


HIGH-INTEGRITY MODELING OF NON-STATIONARY KALMAN FILTER
INPUT ERROR PROCESSES
AND APPLICATION TO AIRCRAFT NAVIGATION

BY
ELISA GALLON

Submitted in partial fulfillment of the
requirements for the degree of
Doctor of Philosophy in Mechanical and Aerospace Engineering
in the Graduate College of the
Illinois Institute of Technology

Approved 
Adviser

Chicago, Illinois
May 2023

© Copyright by
ELISA GALLON
May 2023

ACKNOWLEDGEMENT

First and foremost, I would like to express my sincerest gratitude to my PhD advisor, Professor Boris Pervan, for his exceptional guidance and mentoring, unwavering support, and accessibility. His teaching and mentoring have been invaluable to my personal and academic growth. I could not have asked for a more dedicated and knowledgeable advisor to guide me through my PhD journey.

I would also like to extend my thanks to Professor Mathieu Joerger for his continuous support, constructive feedback, and meticulous review of every aspect of my research. I am grateful for his contributions to the success of this dissertation.

My sincere appreciation goes to the members of my jury committee, Professors Datta-Barua, Williamson, and Williams, for their valuable feedback, and insightful comments and critiques.

I would like to acknowledge Samer Khanafseh for his numerous technical supports throughout my research. His technical expertise has been invaluable to my success.

I would also like to acknowledge my lab mates, Sahil, Jaymin, Kana, Wengxiang, Birendra, and Cagatay, for their camaraderie and support during my research journey. I am grateful for the friendships that have developed inside and outside the lab, and for the shared experiences that made this journey memorable. I am also deeply indebted to KellyAnn, Sal, Alex, Rachel, and Lily, who played an essential role in making my life in Chicago enjoyable. Their friendship and support contributed to the mental and emotional structure of my PhD journey.

I would like to express my gratitude to Yash for his invaluable support, mentorship, and friendship during what could have been the most stressful year of my PhD journey, but ended up being one of the best. His passion and curiosity towards mathematics, physics, and science in general are contagious, and his contributions to my academic and personal growth will always be treasured.

Enfin et surtout, je voudrais remercier mes parents, Valérie et Pascal, ainsi que mon frère Jules pour leur soutien et accompagnement durant toutes mes années d'études. La stabilité familiale et mentale qu'ils m'ont inculquée aura été une base nécessaire au bon déroulement de mon doctorat.

AUTHORSHIP STATEMENT

I, Elisa Gallon, attest that the work in this thesis is substantially my own.

In accordance with the disciplinary norm of authorship in engineering (see IIT Faculty Handbook, Appendix S), the following collaborations occurred in the thesis:

My adviser, Prof. Pervan, and co-adviser, Prof. Joerger, contributed to the design of all experiments and assisted and guided in the interpretation of data as is the norm for a PhD supervisor.

Samer M. Khanafseh contributed to Chapter 7 of this dissertation by sharing his Kalman Filter Matlab code which was modified to obtain the results provided in this chapter.

Santiago Diaz Perea contributed to Chapter 3 of this dissertation by sharing his orbit and clock error generation Matlab code which was modified to obtain the results provided in this chapter.

TABLE OF CONTENTS

	Page
ACKNOWLEDGEMENT	iii
AUTHORSHIP STATEMENT	iv
LIST OF TABLES	viii
LIST OF FIGURES	ix
LIST OF ACRONYMS	xii
LIST OF SYMBOLS	xvi
ABSTRACT	xix
CHAPTER	
1. INTRODUCTION	1
1.1. Introduction to navigation systems	1
1.2. Introduction to ABAS	6
1.3. Prior work & research motivation	9
1.4. Dissertation contributions	11
1.5. Dissertation outline	15
2. TIME SEQUENTIAL ERROR MODELING: METHODOLOGY	17
2.1. Error classification	18
2.2. Frequency domain bounding of stationary input error processes	20
2.3. Procedure: making the most out of experimental data	31
3. ORBIT AND CLOCK ERRORS MODELING	36
3.1. Orbit and clock errors characterization over time	37
3.2. Error stationarity analysis	46
3.3. Robust modeling of orbit and clock errors	47
4. TROPOSPHERIC DELAY MODELING	54
4.1. Evaluation of tropospheric models	55
4.2. Robust modeling of tropospheric residuals	66
5. CARRIER PHASE MULTIPATH MODELING	74
5.1. Dual frequency multipath characterization	76
5.2. Ionospheric delay filtering	77
5.3. Multipath error modeling	79

5.4. Equivalence to iono-free measurements	81
5.5. Summary of the error model	83
5.6. Application to aircraft multipath	84
6. INERTIAL ERRORS MODELING	87
6.1. Methodology: from specifications to bounding model	88
6.2. Experimental evaluation	98
6.3. Opening remarks	104
7. PERFORMANCE ASSESSMENT OF FAULT FREE RECUR- SIVE ARAIM	106
7.1. Summary of GNSS error models	108
7.2. Kalman Filter design	109
7.3. Performance assessment	112
8. CONCLUSION AND FUTURE WORK	123
8.1. Summary of accomplishments	123
8.2. Recommended topics for future research	127
APPENDIX	128
A. EPHEMERIS INTERPOLATION	129
A.1. GPS ephemeris interpolation	130
A.2. Galileo ephemeris interpolation	132
B. VARIANCE OF AUTOCORRELATION ESTIMATES	133
C. SENSITIVITY OF PSD ESTIMATION TO PARAMETER SE- LECTION	135
C.1. Impact of the window shape on a FOGMRP PSD estimate	137
C.2. Impact of the window shape on real orbit and clock error data	138
D. NUMBER OF INDEPENDENT SAMPLES IN A FOGMRP	141
E. ONE-TO-ONE MAPPING ANALYSIS OF INERTIAL ERRORS	144
E.1. Velocity random walk modeled as a white noise	145
E.2. Acceleration random walk modeled as a random walk	145
E.3. Flicker noises modeled as a first order GMRP	146
F. IONOSPHERIC DELAY CUT OFF FREQUENCY VALIDATION	147
F.1. Mathematical representation of multipath	148
F.2. Validation of the cut off frequency for rooftop multipath	153
F.3. Validation of the cut off frequency for Aircraft Multipath	154

G. SNAPSHOT ERROR MODEL OF THE CODE AND CARRIER SMOOTHED CODE MULTIPATH OF OUR TESTING ENVIRONMENT	157
H. PSD BOUNDING OPTIMIZATION: CHOOSING THE BEST TAPERING WINDOW AND FOGMRP BOUND FOR A GIVEN DATASET	160
I. GPS AND GALILEO SATELLITE INFORMATION DURING 2018-2020	165
BIBLIOGRAPHY	168

LIST OF TABLES

Table	Page
3.1 Clocks and blocks of each GPS satellite (March 2018)	44
3.2 Clocks and blocks of each Galileo satellite (March 2018)	45
3.3 PSD bounding summary: FOGMRP parameters	53
4.1 Statistics of MOPS (columns 4-5) and GPT2w (columns 6-7) tropo- spheric residuals for 35 out of the 100 reference stations over year 2018	58
6.1 Inertial errors conversion table	91
6.2 Accelerometer errors bounding model values	102
6.3 Gyroscope errors bounding model values	105
7.1 GNSS Error Model Parameter Values	108
I.1 GAL Block information between 2018 and 2020	166
I.2 GPS Block information between 2018 and 2020	167

LIST OF FIGURES

Figure	Page
1.1 Representation of the GNSS segments	5
1.2 Navigation integrity representation	8
2.1 Error classification decision tree.	20
2.2 PSD Bounding procedure for WSS input	24
2.3 Upper bound on standard deviation of ACF estimate ($\tau_x = 6$ h, $\sigma_x = 1.5$ m)	32
2.4 Block diagram of the dissertation’s high integrity modeling methodology	35
3.1 Error generation diagram	38
3.2 Projection of Radial, Along track and Cross track errors onto the user’s line of sight.	41
3.3 Orbit and clock errors for all GPS and Galileo satellites at 30-s intervals in December 2019	41
3.4 Example ephemerides interpolation (radial errors) of GPS PRN07 in December 2018 (left), as well as its impact on radial plus clock error ACF (right)	42
3.5 GPS and Galileo Orbit and Clock Errors over December 2018	46
3.6 Statistics of the 2018 GPS (upper) and GAL (lower) orbit and clock errors stationary subsets	48
3.7 PSDs of radial-plus-clock errors for: (a) GPS (b) Galileo	51
3.8 PSD bounding of: (a) GPS Rb (b) GAL RAFS (c) GPS Cs (d) GAL PHM	52
4.1 Selection of the 100 IGS stations considered in this dissertation	56
4.2 MOPS tropospheric residual statistics at 100 reference stations over year 2018	59
4.3 Impact of a storm (left) and the rainy season (right) on MOPS tropospheric residuals	60
4.4 GPT2w tropospheric residual statistics at 100 reference stations over year 2018	63

4.5	Impact of a storm (left) and the rainy season (right) on GPT2w tropospheric residuals	64
4.6	Tropospheric models statistics summary	65
4.7	Separating data into stationary segments	67
4.8	MOPS (upper) and GPT2w (lower) tropospheric residuals statistics	69
4.9	PSD bounding of MOPS (left) and GPT2w (right) residuals . . .	70
4.10	MOPS (left) and GPT2w (right) residuals ECDF bounding	70
4.11	Summary table on FOGMRP and Gaussian over-bounding (OB) .	71
5.1	Multipath environment of the Rettaliata Engineering building's rooftop	77
5.2	Sidereal day differences of $L_1 - L_2$ residuals (a), and their PSD estimate for PRN 07 (b)	78
5.3	Resulting carrier multipath after high pass filtering of the $L_1 - L_2$ residuals (all PRNs)	80
5.4	Mapping of the carrier phase multipath for PRN 07	81
5.5	PSD bounding of the $L_1 - L_2$ carrier phase multipath	81
6.1	Diagram of AV bounding cases	92
6.2	Example of failed PSD criterion.	95
6.3	FlowChart of the steps involved in AV bounding	96
6.4	Experimental set up (left) and environment's temperatures (right)	99
6.5	Experimental results: upper-bounding sample accelerometer error PSDs.	100
6.6	AV and PSD domain bounding of IMU errors.	101
6.7	Experimental results: upper-bounding sample accelerometer error PSDs.	103
6.8	AV and PSD domain bounding of IMU errors.	104
7.1	GPS and Galileo satellites in view	113
7.2	KF and LSE/snapshot vertical protection levels	115
7.3	Sensitivity to the FOGMRP parameters	117

7.4	Impact of clock-specific orbit and clock error model on KF output standard deviation	119
7.5	Standard deviations of stationary GPS datasets (2018-2020)	120
7.6	Covariance validation results over 6 sets of 4h	122
A.1	GPS and Galileo Ephemerides Interpolation Diagram	130
A.2	GPS PRN07 Ephemerides Interpolation	131
C.1	Example tapering windows used in the PSD estimation process	137
C.2	Impact of tapering window on PSD estimate of FOGMRP in terms of spectral leakage: (a) original figure, (b) zoomed.	138
C.3	Impact of tapering window on PSD estimate of FOGMRP in terms of data noise: (a) original figure, and (b) zoomed.	138
C.4	(a) Tapered ACF and (b) PSD estimates for GPS PRN 01 orbit + clock errors.	139
F.1	Ground Reflection	148
F.2	Wall Reflection	148
F.3	Complex representation of direct VS reflected signal.	150
F.4	Bessel approximation of ground (left) and wall (right) reflection power distribution	153
F.5	Bessel approximation of spiral divergence (left) and phugoid (right) modes power distribution	154
F.6	Aircraft flight modes [63]	156
G.1	Rooftop multipath	159
H.1	ACF tapering window representation	161
H.2	Selection of the optimal tapering window and FOGMRP parameter, T_2 , σ_x and τ_x for an example dataset (orbit and clock errors of GPS PRN 24 during 2018-2020)	163

LIST OF ACRONYMS

Acronym	Definition
ABAS	Aircraft Based Augmentation System
AC	Analysis Center
Ac/R-RW	Acceleration/Rate Random Walk
ACF	AutoCorrelation Function
AL	Alert Limit
APC	Antenna Phase Center
ARAIM	Advanced Receiver Autonomous Integrity Monitoring
AV	Allan Variance
CDF	Cummulative Distribution Function
CoM	Center of Mass
Cs	Cesium
DD	Double Difference
DF	Dual Frequency
DGNSS	Differential GNSS
DoY	Day of the Year
ENU	East North Up
FANE	False Alarm No Exclusion
FD	Fault Detection
FDE	Fault Detection and Exclusion
FDNE	False Detection No Exclusion
FOGMRP	First Order Gauss Markov Process

FT	Fourier Transform
GBAS	Ground Based Augmentation System
GEO	Geostationary orbit
GNSS	Global Navigation Satellite System
GPS	Global Positioning System
HPL	Horizontal Protection Level
HMI	Hazardously Misleading Information
IGS	International GNSS Service
IGSO	Inclined Geosynchronous Satellite Orbits
IMU	Inertial Measurement Unit
INS	Inertial Navigation System
IR	Integrity Risk
ISM	Integrity Support Message
KF	Kalman Filter
KS	Kolmogorov-Smirnov
LEO	Low Earth Orbit
LSE	Least Square Estimator
MEMS	Micro Electro Mechanical System
MEO	Medium Earth Orbit
MGEX	Multi-GNSS Experiment
MHSS	Multiple Hypothesis Solution Separation
MOPS	Minimum Operational Performance Standards

NANU	Notice Advisory to NAVSTAR users
NOAA	National Oceanic and Atmospheric Administration
PHM	Passive Hydrogen Maser
PL	Protection Level
PNT	Position, Navigation and Timing
PRN	Pseudo-Random Noise
PSD	Power Spectral Density
PVT	Position, Velocity and Time
RAFS	Rubidium Atomic Frequency Standard
RAIM	Receiver Autonomous Integrity Monitoring
Rb	Rubidium
RINEX	Receiver Independent Exchange Format
RW	Random Walk
SARPs	Standards and Recommended Practices
SBAS	Space Based Augmentation System
UNB3	University of New Brunswick
URA	User Ranging Accuracy
URE	User Ranging Error
V/An-RW	Velocity/Angular Random Walk
VPL	Vertical Protection Level
VMF1	Vienna Mapping Function 1
WAAS	Wide Area Augmentation System

WN	White Noise
WSS	Wide Sense Stationary
ZTD	Zenith Tropospheric Delay

LIST OF SYMBOLS

Symbol	Definition
$b_{GD,\rho/\phi}$	Code/carrier phase group delay
b_s	Bias instability
b_r	bias repeatability
c	Speed of light
$\delta t_{k,r}$	Receiver clock bias of receiver r at epoch k
δt_k^i	Satellite clock bias of satellite i at epoch k
$\eta_r^{i,f}$	Carrier phase cycle ambiguity between receiver r and satellite i , on frequency f
ε_x	Total error of process x (i.e. orbit and clock error, tropospheric delay, multipath, or thermal noise)
ϵ_x	Slant error of process x (i.e. tropospheric delay, multipath, or thermal noise)
$\mathbf{\Gamma}_k$	Process noise mapping matrix at epoch k
f_c	Ionospheric delay cut off frequency
f_N	Nyquist frequency
$h(t)$ or $H(f)$	Transfer function and its associated FT
\mathbf{H}_k	Kalman filter observation matrix at epoch k
$I_{k,r}^{i,f}$	Ionospheric delay of receiver r and satellite i on frequency f at epoch k
$\mathbf{I}_{n \times n}$	Identity matrix of size $n \times n$
K	Random Walk parameter
\mathbf{L}_k	Kalman gain at epoch k
λ^f	Wavelength of frequency f

Λ	ACF tapering window
$m_{W/D}$	Wet and Dry VMF1 tropospheric mapping functions
m	Multipath mapping function from [1]
μ_x	Mean value of process x
N_0	White noise density
$\mathbf{P}_{k k-1}$	Kalman Filter covariance matrix
p	Acceleration/Rate random walk
$\phi_{k,r}^{i,f}$	Carrier phase measurement of satellite i and receiver r at epoch k on frequency f
Φ_k	Kalman Filter state transition matrix at epoch k
q_m	Measured output of inertial sensor
q_t	True output of inertial sensor
$r_{k,r}^i$	Range between satellite i and receiver r at epoch k
R_{xx}	Autocorrelation function of process x
\mathcal{R}_{xx}	Instantaneous autocorrelation function of process x
$\rho_{k,r}^{i,f}$	Code measurement of satellite i and receiver r at epoch k on frequency f
$\tilde{\rho}_{k,r}^{i,f}$	Code measurement of satellite i and receiver r at epoch k on frequency f
s_f	Scale factor of inertial errors
S_{xx}	Power Spectral Density of process x
\mathcal{S}_{xx}	Instantaneous Power Spectral Density of process x
$\sigma_{orb}, \sigma_T, \sigma_\phi$	Standard deviations of the FOGMRP models for orbit and clock errors, tropospheric delays and carrier phase multipath

$\sigma_{\hat{R}_{xx}}^2$	Variance of the ACF estimate of process x
σ_y^2	Variance of the Kalman Filter output
Σ_x^2	Allan Variance of process x
$T_{k,r}^{i,f}$	Tropospheric delay of receiver r and satellite i on frequency f at epoch k
T_1	Parameter of the ACF tapering window for which ACF values at correlation times $ \tau < T_1$ remain unchanged
T_2	Parameter of the ACF tapering window for which ACF values at correlation times $ \tau > T_2$ are set to zero
τ	Correlation time
$\tau_{orb}, \tau_T, \tau_\phi$	Time constants of the FOGMRP models for orbit and clock errors, tropospheric delays and carrier phase multipath
ν_k	Measurement noise vector at epoch k
\mathbf{V}_k	Measurement noise covariance matrix at epoch k
w_k	Process noise at epoch k
\mathbf{W}_k	Process noise covariance matrix at epoch k
\mathbf{x}_k	Kalman Filter state vector at epoch k
\mathbf{z}_k	Measurement vector at epoch k

ABSTRACT

Most navigation applications nowadays rely heavily on Global Navigation Satellite Systems (GNSSs) and inertial sensors. Both of these systems are known to be complementary, and as such, their outputs are very often combined in an extended Kalman Filter (KF) to provide a continuous navigation solution, resistant to poor satellite geometry, as well as radio frequency interference.

Additionally, recent development in safety critical applications (such as aviation) revealed the performance limitations of current algorithms (Advance Receiver Autonomous Integrity Monitoring - ARAIM) to vertical guidance down to 200 feet above the runway (LPV-200). When nominal constellations are depleted, LPV-200 can only sparsely be achieved. Exploiting satellite motion in ARAIM (for instance using a KF) could help alleviate those limitations, but would require adequate modeling of the errors, including the error's time correlation.

Power Spectral Density (PSD) bounding is a methodology that provides high integrity, time correlated error models, but this approach is currently limited to stationary errors (which is rarely the case with real data), and has never been applied to navigation errors. More generally, no high integrity, time correlated error models have ever been derived for navigation errors.

As a result, in the first part of this thesis, a methodology for high integrity modeling of time correlated errors is introduced. The PSD bounding methodology is extended to both stationary and non-stationary errors.

In the second part of this thesis, these methodologies are applied to the 3 main error sources impacting iono-free GNSS measurements (orbit and clock errors, tropospheric errors and multipath), as well as to inertial errors.

The methodology introduced in this dissertation provides high integrity time

correlated error models and is applicable to any type of applications where high integrity is required (e.g. Differential GNSS - DGNSS, Aircraft Based Augmentation System - ABAS, Ground Based Augmentation System - GBAS, Space Based Augmentation System - SBAS, etc...). Additionally, the error models derived here are not only limited to high integrity applications, but could also be used in applications where the correlation over time of the errors plays an important role (such as any KF integration).

In the last part of this dissertation, we focus on a specific safety critical application: aviation, and in particular ARAIM. The dissertation is concluded with an assessment of the performance improvements provided by recursive ARAIM, using those bounding dynamic error models, with respect to those models, used for baseline snapshot ARAIM. Additionally, a sensitivity analysis is performed on each of the error model parameters to assess which of them impacts the KF performance (i.e. covariance) the most.

CHAPTER 1

INTRODUCTION

1.1 Introduction to navigation systems

With the creation of new transportation systems in the 17th and 18th Centuries came the development of more and more ingenious navigation tools, most of which were based on observation of celestial bodies and the prior knowledge of their position. The Industrial Revolution in the 18th Century and the development of the first combustion engine in early 19th Century propelled the creation of more modern navigation means, two of which are the cornerstone of this thesis: Inertial and Satellite Navigation.

1.1.1 Inertial Navigation Systems. Practical Inertial Navigation Systems (INSs) have been available since the 1950s but were initially very large and very costly. Over the years, their prices and sizes have decreased, and most INSs can now be classified into one of four categories: consumer, industrial, tactical or navigation grade.

These systems use inertial sensors to estimate and track their relative position (with motion sensors) and attitude (with rotation sensors). Newton's laws tells us that a body's motion will uniformly follow a straight line unless disturbed by an external force. Hence, acceleration measurements provided by an inertial sensor can be mathematically integrated with respect to time to obtain relative position and velocity estimates. Acceleration measurements are provided by a specific type of inertial sensors: accelerometers. To navigate, it is important to keep track of the direction in which the accelerometer is pointing. Gyroscopes are inertial sensors that measure the body's angular rates. Once integrated, they can provide attitude estimates.

To obtain 3D estimates of a body's position and attitude, 3 sets of each of these sensors are commonly placed in an orthogonal basis. This ensemble of sensors is referred to as an Inertial Measurement Unit (IMU).

These types of sensors perform what is called "dead-reckoning", meaning they can only estimate *relative* positions. Additionally, when the sensors' measurements are integrated, the noise impacting these measurements is integrated as well, resulting in the creation of a large drift over time. Depending on the INS' grade, those drifts can become more or less incapacitating.

To cope with these limitations, INS measurements are commonly combined with absolute positioning measurements from GNSS.

1.1.2 Global Navigation Satellite Systems. On October 4, 1957, the Soviet Union launched Sputnik: the first satellite to successfully orbit the earth. While analyzing Sputnik's transmitted radio signal, a group of researchers from the Applied Physics Laboratory at Johns Hopkins University noticed that the frequency of its radio signals increased as the satellite approached, and decreased as it moved away. This phenomenon, known as Doppler effect, was later used to estimate the satellite's location and track its movement from the earth. This observation led the scientists to believe that a reversed approach to this problem could be possible: if a receiver on the ground can estimate a satellite's location, then a receiver can probably estimate its location by its distance from a satellite. This discovery led to the creation, in 1958, of the Transit system: the first GNSS. Initially developed by John Hopkins University; it transitioned to the Navy in the mid-1960s and provided continuous service by 1964 using Low Earth Orbit (LEO) satellites. Transit could deliver up to tens of meters accuracy (depending on the number of observations used) for 28 years, before being superseded by the Global Positioning System (GPS) in 1996.

The GPS system has now been fully operational for over 25 years and is slowly being complemented with additional constellations [2, 3], making satellite navigation more accurate and available to an increasing number of applications.

- The *GPS* constellation (USA) is comprised of 32 satellites in 6 equally spaced orbital planes. The satellites are placed in Medium Earth Orbit (MEO) with a nominal period of 11 hours, 58 minutes and 2 seconds, repeating their geometry each sidereal day enabling global coverage for continuous and instantaneous position fixes.
- The *Galileo* constellation (EU) has a Full Operational Capability (FOC) of 27 operational and 3 spare MEO satellites, spread on 3 orbital planes. Their geometry will repeat every 10 sidereal day, with a period of 14 hours, 4 minutes and 45 seconds.
- The *GLONASS* constellation (Russia) consists of 24 MEO satellites distributed over 3 orbital planes. They have a nominal period of 11 hours, 15 minutes and 44 seconds, repeating the geometry every 8 sidereal days.
- The *BeiDou* constellation (or COMPASS - China) will consist of 35 satellites, including 5 in Geostationary orbits (GEO) and 30 in non-GEO satellites in near-circular orbits. Among the non-GEO satellites, 3 are in Inclined Geosynchronous Satellite Orbits (IGSO) and 27 are in MEO with an orbital period of 12 hours and 53 minutes, repeating their ground track every 7 sidereal days.

Each of these GNSS constellations are divided into 3 main segments, as represented in Figure 1.1:

- The *space segment* is composed of GNSS satellites (e.g. 32 for GPS) orbiting the earth typically in MEO. Each GNSS constellation has its own fleet of satellites,

arranged in orbit to provide their desired coverage. The satellites broadcast ranging signals to the user segment that can be used for Position, Navigation, and Timing (PNT). These signals contain information that identifies the satellite, and provides satellite orbit information (the ephemeris), a satellite range estimate of the signal, and a rough estimate of where other satellites in the constellation are (the almanac).

- The *control segment* consists of master stations, data upload stations, and monitor stations. The master station(s) generate the satellite's orbit and clock parameters based on measurements collected by the monitor stations, in order to maintain accuracy. The monitor stations are scattered around the globe and continuously monitor the constellation's signals and status. The master station(s) then analyses these observables and uplink fresh orbit and clock products to the satellites via the data uplink stations.
- The *user segment* consists of the multitude of (governmental and civilian) receivers around the globe (terrestrial, aviation, and beyond) where each receiver processes the GNSS satellites' signals to determine the users position and time.

The GNSS concept relies on the principle of multilateration. Each satellite transmits a so called ranging signal containing (among other information) the time of emission of the signal from the satellite. As the user receives this signal, it can estimate its distance from the satellite by estimating the difference between the time of emission and the time of reception of the signal. Knowing its distance from multiple satellites, the user can apply multilateration to estimate their position. In theory, a minimum of three measurements are needed to estimate the 3D coordinates of a user. In practice, since most receivers use low-cost quartz-oscillator clocks, their deviation from GNSS time needs to be estimated as well, bringing the total number of unknowns to 4.

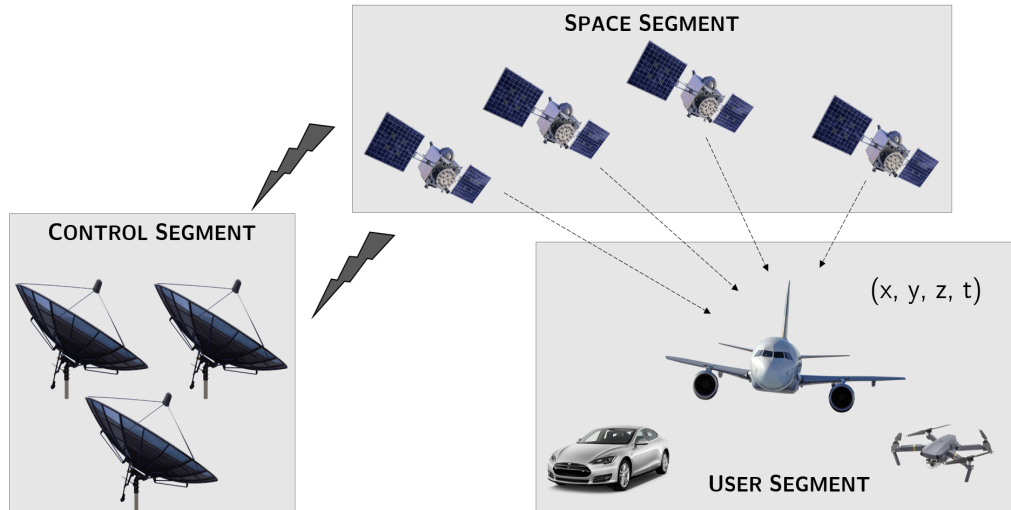


Figure 1.1. Representation of the GNSS segments

Over the years, GNSS has become essential for applications ranging from agriculture, mining and construction, to aviation, rail, harbor and autonomous navigation. With each of these applications, comes a different set of accuracy, integrity and continuity requirements. In this thesis, we focus on safety critical applications.

1.1.3 Navigation Integrity & Continuity. For safety critical applications, such as aviation, it is commonplace to consider performance metrics other than accuracy, namely integrity, continuity, and availability. Because of the safety critical aspect of civil aviation applications, integrity is of the utmost importance as it guaranties that the system is protected against rare event faults such as satellite/constellation failures.

The ICAO Standards and Recommended Practices (SARPs) [4] defines these four performance metrics, for the aviation domain, as follows [5]:

Integrity is “a measure of the trust that can be placed in the correctness of the information supplied by the total system. Integrity includes the ability of a system to provide timely and valid warnings to the user (alerts)”. The Integrity Risk (IR) is

defined as the probability of an undetected system error or fault causing Hazardous Misleading Information (HMI), which may result in a large positioning error. The integrity risk is quantified when the user computes its error bounds (Protection Level - PL) at each epoch and compares them to a pre-defined Alert Limit (AL). Depending on the applications and/or the flight operation level, those probabilities must remain within a certain range, between 10^{-7} and 10^{-9} .

Continuity is “the capability of the system to perform its function without unscheduled interruptions during the intended operation, expressed as a probability”. The Continuity Risk (CR) is the sum of probability of two separate events: when a false alarm occurs and cannot be excluded (FANE), and when a fault is detected and cannot be excluded (FDNE). Once again, these requirements will vary depending on the application and operational level.

Accuracy is “defined as the difference between a computed and a true position”. Position estimated at any location must be within a pre-defined accuracy bound 95% of the time in order to meet the system’s accuracy requirements (for GPS and Galileo).

Availability is “the portion of time (...) during which the system provides reliable navigation information” (i.e. is simultaneously meeting the accuracy, integrity and continuity requirements). Availability is a key performance metric since it measures the operational performance of a navigation system.

1.2 Introduction to ABAS

For safety critical applications such as aviation, where the user is traveling at considerable speed and can quickly deviate from its flight path, integrity is of the utmost importance. Three types of augmentations were developed to complement GNSS with the aspect of integrity: ABAS (Aircraft Based Augmentation Systems),

GBAS (Ground Based Augmentation System) and SBAS (Space Based Augmentation System). These augmentation systems can be divided into two subgroups: the independent algorithms (ABAS) and the ones dependent on external data (GBAS/SBAS). In particular, the ABAS system, independent of external processes, augments and/or integrates the information obtained from the other GNSSs with additional (integrity) information available on board the aircraft.

Over the years, the GNSS community has pushed to develop an ABAS solution that would ensure integrity in the civil aviation domain down to Non Precision Approaches (NPA), such as Receiver Autonomous Integrity Monitoring (RAIM).

RAIM is a user algorithm that makes use of measurement redundancy from 5 or more satellites to check for the relative consistency among them and, in case of fault detection, exclude the most likely faulted measurement(s)/satellite(s). As we know, a minimum of four satellites are needed in order to compute a 3D position estimate. In practice, a user on earth will observe more than 4 satellites in view at any time. If at least five are visible, the user can in theory use that redundancy to detect a faulty measurement. This is Fault Detection (FD), a core concept of RAIM. If at least six satellites are available, the faulty satellite can be excluded as well. This is Fault Detection & Exclusion (FDE). The most commonly used method for fault detection is Multiple Hypothesis Solution Separation (MHSS), which relies on the computation of test statistics to extract the faulty measurement(s) [6].

To evaluate the integrity and continuity performance of a system, PL are computed. PLs are bounds on the uncertainty of the estimated position. The Horizontal Protection Level (HPL) is the radius of a circle around the true position in the horizontal domain. The Vertical Protection Level (VPL) is a similar distance in the vertical domain. Both of these bounds describe the region that is assured to contain or bound the provided position to a very high probability. To ensure integrity, these

bounds are compared to a-priori specified AL: the probability that the true position lies outside of these bounds is called the Integrity Requirement I_{REQ} (see Figure 1.2). The aircraft is considered to be operating safely if no PL exceeds its associated AL.

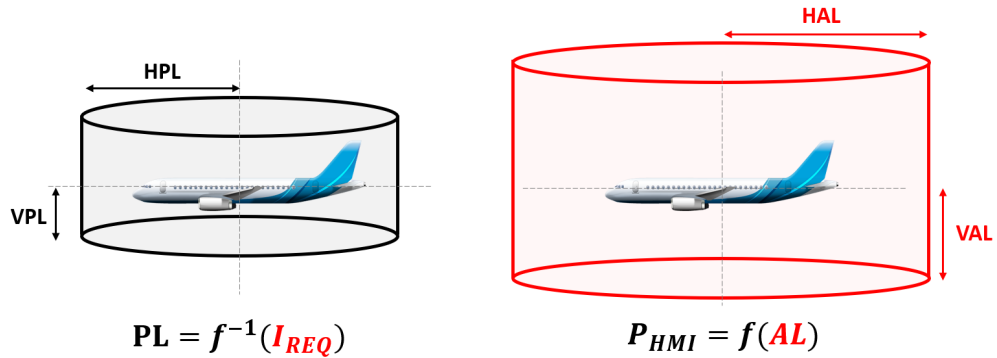


Figure 1.2. Navigation integrity representation

RAIM was developed on GPS L1-C/A signals and was only intended to support lateral navigation. For vertical guidance, Advanced RAIM (ARAIM) was developed, and takes advantage of:

- Frequency diversity: ARAIM is a multi-frequency system that enables iono-free measurements, eliminating a major source of error: the ionosphere.
- Geometry diversity: ARAIM is a multi-constellation system that takes advantage of the increasing number of constellations, and hence satellites available to the user.
- Integrity Support Message: ARAIM uses safety assertions on each of the GNSS constellations to augment the navigation solution. These safety assertions (e.g. probability of satellite fault, probability of constellation fault...) are contained in the Integrity Support Message (ISM), and available onboard the aircraft.

1.3 Prior work & research motivation

RAIM was initially intended to support horizontal guidance for aircraft during en-route flights using GPS L1 only. Extensive efforts have been made to develop a new dual frequency, multi-constellation ARAIM FDE method. ARAIM is now intended to support applications such as vertical guidance (LPV-200). However, [7] showed that when nominal GPS and Galileo constellations are depleted, LPV-200 could only be sparsely achieved. Further, snapshot ARAIM cannot provide better performance than LPV-200 even under optimistic constellation assumptions.

Reference [7] describes a new ARAIM integrity monitoring method which exploits the motion of satellites from multiple constellations: *batch ARAIM*. Although batch ARAIM was shown to be more computationally and memory expensive than snapshot ARAIM, it can also provide dramatic performance improvements: meeting the 10 m alert limit in nominal conditions and achieving LPV-200 requirements using depleted constellations. By potentially achieving 10-meter ALs, sequential ARAIM algorithms (using batch estimators or KFs) open the possibility to extend the scope of ARAIM applications beyond aircraft navigation, to rail, harbor, or arctic navigation.

Although the batch implementation had the advantage of presenting minimal modifications from the snapshot ARAIM algorithm, its computational power and complexity would gradually increase (and potentially become un-manageable) with the mission duration, especially when used in combination with high rate sensors (such as inertial sensors). A KF implementation of ARAIM, on the other hand, could help reduce the computational and memory cost of batch-ARAIM, while keeping the benefits of incorporating satellite motion in ARAIM.

For safety critical applications (e.g. aviation), the error models considered need to be bounding (e.g. they need to over-bound the actual errors encountered by

the user/impacting the measurements). Additionally, since KF relies on filtering of the errors over time, bounding error models that also account for the time correlation of the errors are needed. Most error models developed in the literature are either snapshot models (i.e. do not account for the stochastic dynamic of the errors) or are not bounding (and can therefore not be applied to safety critical applications). Time correlated, bounding error models still need to be developed.

A lot of research has been done in the field of high integrity error modeling. Recently, the concept of Cumulative Distribution Function (CDF) over-bounding was introduced by [8] and refined in [9]. Building on this prior work, [5] employed over-bounding theory to define upper bounds on the variances of orbit and clock errors for both GPS and Galileo satellites. If these error models are sufficient for snapshot positioning, they however are not for time-sequential implementations because they do not address the stochastic dynamics of the errors over time.

To account for this limitation, [10] derived an analytical bound on integrity risk for time-sequential linear estimators using AutoCorrelation Function (ACF) bounding of the errors impacting the navigation solution. But, this ACF-based approach requires continuous, cumulative storage of all data and estimator coefficients over time, and except for short, finite-horizon intervals, is unsuitable for KF implementations, especially in the case of high rate sensors. More recently, [11] introduced the concept of PSD bounding. The PSD bounding method, unlike ACF bounding, is not restricted to fixed-interval implementations and is compatible with Kalman filtering. Therefore, in this thesis, we build up on the concept of PSD bounding (of the errors impacting carrier phase measurements) and extend it to the more “realistic” case of non-stationary errors. The error models developed are then incorporated in a KF version of ARAIM: *recursive* ARAIM.

The methodology and error models derived in this work are not only applica-

ble to ARAIM related applications, but also to any applications that could benefit from high integrity models that account for the time correlated aspect of stochastic processes (such as GNSS/INS integration). Indeed, extensive research [12] has been done to show the numerous advantages of combining GNSS measurements with inertial sensors. Combining GNSS and INS in a KF version of ARAIM has the potential to:

- Benefit from satellite motion to meet LPV-200's stringent (high integrity) requirements,
- Provide robustness against radio frequency interference attacks (i.e. jamming, spoofing),
- Improve continuity through sky obstructed areas, such as urban canyons.

Additionally, the rise of autonomous applications (urban, drones, maritime or rail navigation) in recent years has increased the need for high integrity systems. Most of these applications come with stringent requirements, and very low AL. Adapting *recursive* ARAIM to these applications could be extremely beneficial.

The error models and methodology derived in this thesis could potentially help improve the performance of these systems too.

1.4 Dissertation contributions

This dissertation contains five main contributions. They are outlined in the following subsections.

1.4.1 Bounding models for random processes. PSD bounding is a powerful tool used to provide high integrity, time correlated error models. But this methodology is currently limited to stationary errors, and has never been applied to navigation

errors. The definition of the statistical tools used in this dissertation to model GNSS errors will vary depending on the stationarity of the errors involved. As a first step, we introduce two stationary tests: the Levene test and the Kolmogorov Smirnov (KS) test. Those two tests will be used in combination to determine whether our experimental data is stationary or not. Additionally, non-stationarity is separated in 3 categories; the PSD bounding methodology is extended to each of these categories.

1.4.2 Developing GNSS & INS high integrity, time correlated error models.

The 4 main error sources impacting iono-free signals are modeled:

- **Orbit and clock errors:** GPS and Galileo orbit and clock errors are derived from existing code/carrier observables and final clock/orbit products (as ground truth) for the years of 2018-2020. Each constellation's data is divided according to their two clock types: Cesium/Rubidium (Cs/Rb) for GPS and Passive Hydrogen Maser/Rubidium Atomic Frequency Standard (PHM/RAFS) for Galileo. The different clock characteristics are observed in the time and frequency domain. Power Spectral Density bounding is then employed to derive robust, time-correlated models of the orbit and clock errors for each of the satellite clock types.
- **Tropospheric errors:** Tropospheric delays from 2018 are generated for 100 stations worldwide based on ground truth measurements. Two tropospheric models are studied. The Minimum Operational Performance Standards (MOPS) model, which is commonly used in many GNSS applications (e.g. aviation) and requires little computational power. And the GPT2w model, which is computationally heavy and usually used in Geodetic applications. The advantages and drawbacks of each models are brought up and compared against one another. Specific scenarios (e.g. India's monsoon seasons, or Hawaii's 2018 transient storm) are also evaluated to observe the quality of each model in these unique

conditions. Each model's residuals then have their PSDs upper bounded to provide a robust model to these residuals.

- **Multipath errors:** Carrier multipath is characterized by performing the difference of carrier phase measurements on 2 different frequencies. The remaining ionospheric delay is filtered out with a high pass filter whose parameters are determined through an extensive analysis of local ionospheric delay. This filtering approach to multipath characterization is novel and has never been done before. Once multipath is characterized, the PSD bounding method is applied to it so as to obtain a bounding model for multipath errors. There are two types of multipath errors considered in this work:
 - IIT Rooftop/experimental static multipath errors, for which the resulting model will be used in our final KF implementation.
 - Aircraft multipath errors, which will be used to show a methodology that other users can apply to their own aircraft data.
- **Inertial errors:** Individual IMU error components are modeled, and the methodology is validated with experimental data. IMU errors can be modeled as a sum of independent error components. These elements of gyroscope and accelerometer errors can be analyzed using the Allan Variance (AV). The AV method is often adopted by IMU manufacturers because it allows for the identification of the different components of the IMU errors. Prior contributions used an approach to robust error modeling, through PSD bounding, to ensure KF output integrity. But the PSD obtained from raw inertial measurements are often too noisy and inaccurate, resulting in an overly conservative model. This leads us to our next main contribution:

1.4.3 Reinforcing AV bounding to provide high integrity models for in-

ertial errors. Manufacturers tend to provide high quality AV curves that were obtained under controlled environments. Leveraging these high accuracy AV curves, for instance by bounding them, would be to the user’s best interests. We will show however that AV bounding alone is not sufficient to provide high integrity, and will derive additional criterion to that effect. This result has never been shown for these specific cases before.

1.4.4 Exploiting satellite motion: *Recursive* KF positioning implementation.

The error models derived in the above contributions are combined into this KF implementation of (fault free) recursive ARAIM. This section outlines the details of the KF ARAIM design. Unlike snapshot ARAIM, which relies on dual-frequency, ionospheric-free carrier-smoothed-code measurements, recursive ARAIM mainly uses raw iono-free carrier phase measurements. Dual-frequency iono-free code phase measurement errors will be heavily influenced by antenna group delays (also referred to as front end group delays), the dynamics of which cannot be modelled stochastically in a KF. Indeed, antenna group delays are deterministic processes: the errors will change according to the antenna’s environment, as well as substantial platform reorientations (e.g., turns, banks) and satellite line of sight variation. In principle, this effect is calibratable, albeit not always easily for many platforms of interest, like civil transport aircraft. Although much the same can be said for multipath, in this case error dynamics are highly sensitive to small scale attitude motions and further complicated by a multiplicity of reflective surfaces on platforms with complex shapes, (again) like transport aircraft, making multipath far more amenable to stochastic modelling. We focus on raw carrier phase measurements because their platform/antenna dependent errors are restricted to multipath and thermal noise, which can be modelled stochastically in a KF. Code measurements are used to aid in the initialization of floating carrier cycle ambiguities, but they will not otherwise be used (or needed) in the recursive ARAIM KF.

To properly account for the time correlation of the errors present in the raw carrier phase measurements (satellite orbit and clock errors, residual tropospheric delay, multipath error, and thermal noise), bounding dynamic error models derived in this dissertation are used. These bounding models are First Order Gauss Markov Random Processes (FOGMRPs) incorporated into the KF by state augmentation. Chapter 7 will describe the details of this implementation.

1.4.5 Performance assessment of Recursive positioning and interpretation for aviation. An assessment of the performance improvements provided by recursive ARAIM, compared to baseline snapshot ARAIM is achieved using bounding dynamic error models. Selecting an example Chicago, IL location, PLs over one day are analysed in both scenarios and compared to one another. These resulting PLs will help us assess the performance of our system in terms of integrity and continuity. Additionally, a sensitivity analysis is performed on each of the error model parameters to assess which of them impacts the KF performance (i.e. covariance) the most. Finally, experimental data will be collected in our lab (Chicago, IL) and used to validate the results obtained in the previous covariance analysis.

1.5 Dissertation outline

Chapter 2 of this dissertation outlines the specifics of a new methodology to robustly model errors and their time correlation: Power Spectral Density Bounding [11]. As outlined in the previous section, most error models developed in the literature are either snapshot models (i.e. do not account for the stochastic dynamic of the errors) or are not bounding (and can therefore not be applied to safety critical applications). Applying PSD bounding theory to GNSS and INS errors has therefore never been done, and the performance improvements of such bounding models have never been quantified either.

The following Chapters (3-6) apply this methodology to navigation errors (GNSS and Inertials) and represent some of the main contributions of this thesis. Those models are then incorporated in a recursive implementation of ARAIM, outlined in Chapter 7. Chapter 7 then evaluates the performance of said modifications to state of the art ARAIM. Finally, Chapter 8 summarizes the different results obtained in this dissertation and opens to a discussion on the possible advantages and applications of such implementation.

CHAPTER 2

TIME SEQUENTIAL ERROR MODELING: METHODOLOGY

The complementary properties of GNSS and INS are leveraged in algorithms that filter their measurements over time, for example using a KF. The performance of a KF is highly dependent on the quality of its error models. GNSS and INS measurements are impacted by errors that include atmospheric delays, satellite orbit and clock errors, multipath, accelerometer and gyroscope errors. Each source of error must be carefully modeled. Since measurements are filtered over time, their error time-correlation must be accounted for. This chapter focuses on the development of a new, high integrity and time-correlated error modeling methodology.

In addition, in safety critical applications such as aviation applications, robust and reliable error models must be derived to upper-bound the navigation integrity and continuity risks. CDF overbounding [8] has been used extensively to bound risks for snapshot, instantaneous least-squares position estimators. However, this approach does not account for model uncertainty over time. Several approaches to upper-bound navigation integrity risk while accounting for time correlated errors were developed, but require large data processing and storage capabilities [10, 13, 14]. In the case of high-update-rate inertial-aided navigation, these approaches present computational and memory constraints that greatly limit the allowable filtering duration.

A new approach to overbound KF-based estimate error distributions in the presence of uncertain time-correlated noise was developed in [11]. This approach relied on upper bounding a modified PSD derived from the Fourier Transform (FT) of a windowed ACF for stationary errors.

However, the treatment of experimental data for the modeling of wide-sense

stationary processes has yet to be formalized, and the case of non-stationary error processes remains unaddressed. For instance, inertial measurements have non-stationary noise components, flicker noise, that cannot directly be modeled using the approach in [11] because the evaluation method of PSD and ACF may differ for such random processes. Therefore, new modeling methods must be derived.

Section 1 of this chapter defines conditions used to classify error processes with respect to their stationarity characteristics. Section 2 then develop robust modeling approaches: for each type of error, experimental examples are given to demonstrate the proposed methodology using actual data. Section 3 provides a practical description of the statistical tests used in this work to assess the stationarity of a finite data set, and ends with a diagram summarizing this chapter.

2.1 Error classification

This section aims at classifying stationary and non-stationary processes. It serves as outline for the remainder of the chapter where modeling methods are derived for each category of non-stationary process.

2.1.1 Wide-Sense Stationary Errors. Mean values and autocorrelation functions are key descriptors of a random process' statistical properties. The mean value of a random process x at time t can be expressed as:

$$\mu_x(t) = E[x(t)] \quad (2.1)$$

where $E[\]$ is the expected value operator. In addition, the correlation between the values of the random process x at two different times $t - \tau/2$ and $t + \tau/2$, also called the ACF, is defined as:

$$\mathcal{R}_{xx}(\tau, t) = E \left[x \left(t + \frac{\tau}{2} \right) x \left(t - \frac{\tau}{2} \right) \right] \quad (2.2)$$

If $\mu_x(t)$ or $\mathcal{R}_{xx}(\tau, t)$ change over time t , then process x is said to be *non-*

stationary. If $\mu_x(t)$ and $\mathcal{R}_{xx}(\tau, t)$ do not vary with t (i.e. $\mu_x(t) = \mu_x$ and $\mathcal{R}_{xx}(\tau, t) := R_{xx}(\tau)$), then process x is called Wide Sense Stationary (WSS). This definition of stationarity is sufficient for our purposes moving forward. Note that we use different notation for a stationary ACF R_{xx} and a non-stationary (instantaneous) ACF \mathcal{R}_{xx} .

However, despite the simplicity of its definition, when dealing with a finite number of samples from an experimental dataset, the stationarity of the stochastic process can be challenging to assess. The following subsection addresses the classification of non-stationary errors.

2.1.2 Non-Stationary Errors. When process x is non-stationary, the ACF in Equation 2.2 is called an *instantaneous* ACF [15] and depends on both t and τ . This function can be determined in one of two ways:

- a) analytically, if the process is understood well enough to evaluate Equation 2.2,
- or
- b) using experimental data.

In practice, option (a) is rarely available. Obtaining sufficient data for option (b) is only possible if the ACF variation over (real) time t are much slower than over the lag time τ :

$$\frac{\partial \mathcal{R}_{xx}}{\partial t} \ll \frac{\partial \mathcal{R}_{xx}}{\partial \tau} \quad (2.3)$$

In this dissertation, we consider two specific classes of non-stationary error processes:

- Condition 2.3 is satisfied, so that stationary sample ACFs can be computed.
- Condition 2.3 is not satisfied, but the PSD of the process is not a function of time and sample PSDs can be computed.

The remaining case of fast-varying non-stationary processes with time-varying PSDs is introduced in Chapter 4 by means of an example of rapid change in GNSS tropospheric delay encountered during passage of a severe storm front. Such events will likely need to be dealt with using real time detection and adaptation (e.g., measurement exclusion) rather than stochastic modeling, and are therefore outside the scope of this work.

The overall classification of error processes is summarized in Figure 2.1.

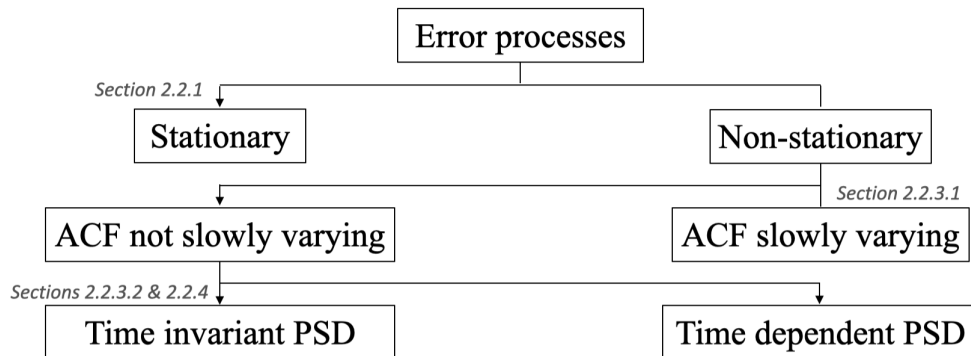


Figure 2.1. Error classification decision tree.

2.2 Frequency domain bounding of stationary input error processes

In [11], Langel et al. derived a frequency domain criterion for modeling stationary correlated noise through PSD error bounding. This section gives a simpler, alternative proof of this criterion for time-invariant and time-varying KFs.

Because the KF is a linear filter, we can separately evaluate the impacts of independent error sources, and then add their output contributions. Therefore, for clarity of exposition in the following derivation, we consider a scalar KF fed by zero-mean sensor data and process noise contributions.

2.2.1 Time-Invariant KF with WSS Input. We first consider the case of a

steady-state KF fed by zero-mean stationary noise. Consider a scalar error input¹ $x(t)$ with PSD $S_{xx}(f)$. In general, the KF is designed using $\bar{S}_{xx}(f) \neq S_{xx}(f)$. The transfer function of this KF from $x(t)$ to some scalar output of interest $y(t)$ is $\bar{h}(t)$ (and its Fourier Transform $\bar{H}(f)$). Note that the bar notation $\bar{\cdot}$ is used here to denote the parameters used to design the KF. We will show later on that these parameters are upper bounds of the true error, hence the notation.

The mean of the KF output error is zero (because the input is zero-mean), and the *true* output error variance is

$$\sigma_y^2 = \int_{-\infty}^{\infty} |\bar{H}(f)|^2 S_{xx}(f) df. \quad (2.4)$$

However, the KF will produce a *predicted* output error variance

$$\bar{\sigma}_y^2 = \int_{-\infty}^{\infty} |\bar{H}(f)|^2 \bar{S}_{xx}(f) df. \quad (2.5)$$

Clearly, if $\bar{S}_{xx}(f) > S_{xx}(f) \forall f \in \mathbb{R}$, then $\bar{\sigma}_y^2 > \sigma_y^2$.

The PSD upper-bound $\bar{S}_{xx}(f)$ can be used to define a time-correlated measurement error model that guarantees an upper bound on the KF estimation error variance [11, 16].

2.2.2 Time-Varying KF with WSS Input. Considering a time-varying filter with transient response $\bar{h}(\tau, t)$ to a unit impulse $\delta(\tau)$, the filter's output to an input $x(t)$ is described by the following convolution integral:

$$y(t) = \int_{-\infty}^{\infty} \bar{h}(\alpha, t) x(t - \alpha) d\alpha, \quad (2.6)$$

¹The scalar function $x(t)$ can represent any stationary sensor or process noise input to the KF. It can be the sum of multiple error components—e.g., $x(t) = \sum_i x_i(t)$.

The variance of the output can then be derived as:

$$\begin{aligned}
\sigma_y^2(t) &= E[y(t)^2] \\
&= E\left\{ \int_{-\infty}^{\infty} \bar{h}(\alpha, t)x(t - \alpha)d\alpha \int_{-\infty}^{\infty} \bar{h}(\beta, t)x(t - \beta)d\beta \right\} \\
&= \int_{-\infty}^{\infty} \int_{-\infty}^{\infty} \bar{h}(\alpha, t)\bar{h}(\beta, t)E[x(t - \alpha)x(t - \beta)]d\alpha d\beta \\
&= \int_{-\infty}^{\infty} \int_{-\infty}^{\infty} \bar{h}(\alpha, t)\bar{h}(\beta, t)R_{xx}(\alpha - \beta)d\alpha d\beta.
\end{aligned} \tag{2.7}$$

Using the Wiener-Khinchin theorem [17] to express the relationship between the stationary ACF R_{xx} and the stationary PSD S_{xx} as:

$$R_{xx}(\alpha - \beta) = \int_{-\infty}^{\infty} S_{xx}(f)e^{-i2\pi f(\alpha - \beta)}df, \tag{2.8}$$

we can rewrite equation 2.7 as:

$$\begin{aligned}
\sigma_y^2(t) &= \int_{-\infty}^{\infty} S_{xx}(f) \int_{-\infty}^{\infty} \bar{h}(\alpha, t)e^{-i2\pi f\alpha}d\alpha \int_{-\infty}^{\infty} \bar{h}(\beta, t)e^{i2\pi f\beta}d\beta df \\
&= \int_{-\infty}^{\infty} S_{xx}(f)\bar{H}(f, t)\bar{H}(f, t)^*df,
\end{aligned} \tag{2.9}$$

$$\sigma_y^2(t) = \int_{-\infty}^{\infty} S_{xx}(f)|\bar{H}(f, t)|^2df. \tag{2.10}$$

Similar to Equation 2.5 for the time-invariant case, Equation 2.10 shows that for a time-varying KF: if $\bar{S}_{xx}(f) > S_{xx}(f) \forall f \in \mathbb{R}$, then $\bar{\sigma}_y^2(t) > \sigma_y^2(t) \forall t \in \mathbb{R}^+$.

2.2.2.1 Experimental procedure. The PSD bounding methodology was first introduced in [10, 11, 18]. The proposed methodology relied on a four step process:

- Estimate the sample ACF R_{xx} of the input process x (done with the matlab function *xcorr*).
- Multiply it with a tapering window Λ . This tapering window is used to reduce the spectral leakage generated by the implicit rectangular window when using finite data.

- Take the Fourier Transform of our modified/windowed ACF function, to obtain the (modified) PSD of the process x .
- Derive a high integrity, time correlated error model by upper bounding the PSDs.

This process is represented in Figure 2.2.

The finite nature of experimental data can be compared to applying a rectangular window over a process. Rectangular windows, with their sharp edges, introduce spectral leakage during the conversion from time domain to frequency domain, and degrade the quality of the resulting PSD estimate. To counter this effect, tapering windows are often used (e.g. Hamming window, Hann window). Additionally, it is important to note that the longer the dataset, the more accurate the ACF estimate will be. However, for most applications, the mission duration (let us call it T_1) is finite and the user will therefore not observe correlations longer than this mission duration (i.e. flight duration - 18 hours for the longest on record). The information contained in the ACF for lag times longer than the mission duration is therefore not useful and can be leveraged in the windowing process, to reduce spectral leakage.

The window used in this work was developed in [18] and is expressed for each lag time τ as:

$$\Lambda(\tau, T_1, T_2) = \begin{cases} 0, & \text{for } \tau < -T_2 \\ \frac{-1}{e^{4\eta/(1-\eta^2)} + 1} + 1, & \text{for } -T_2 \leq \tau < -T_1 \\ 1, & \text{for } -T_1 \leq \tau \leq T_1 \\ \frac{1}{e^{4\eta/(1-\eta^2)} + 1}, & \text{for } T_1 < \tau \leq T_2 \\ 0, & \text{for } \tau > T_2 \end{cases} \quad (2.11)$$

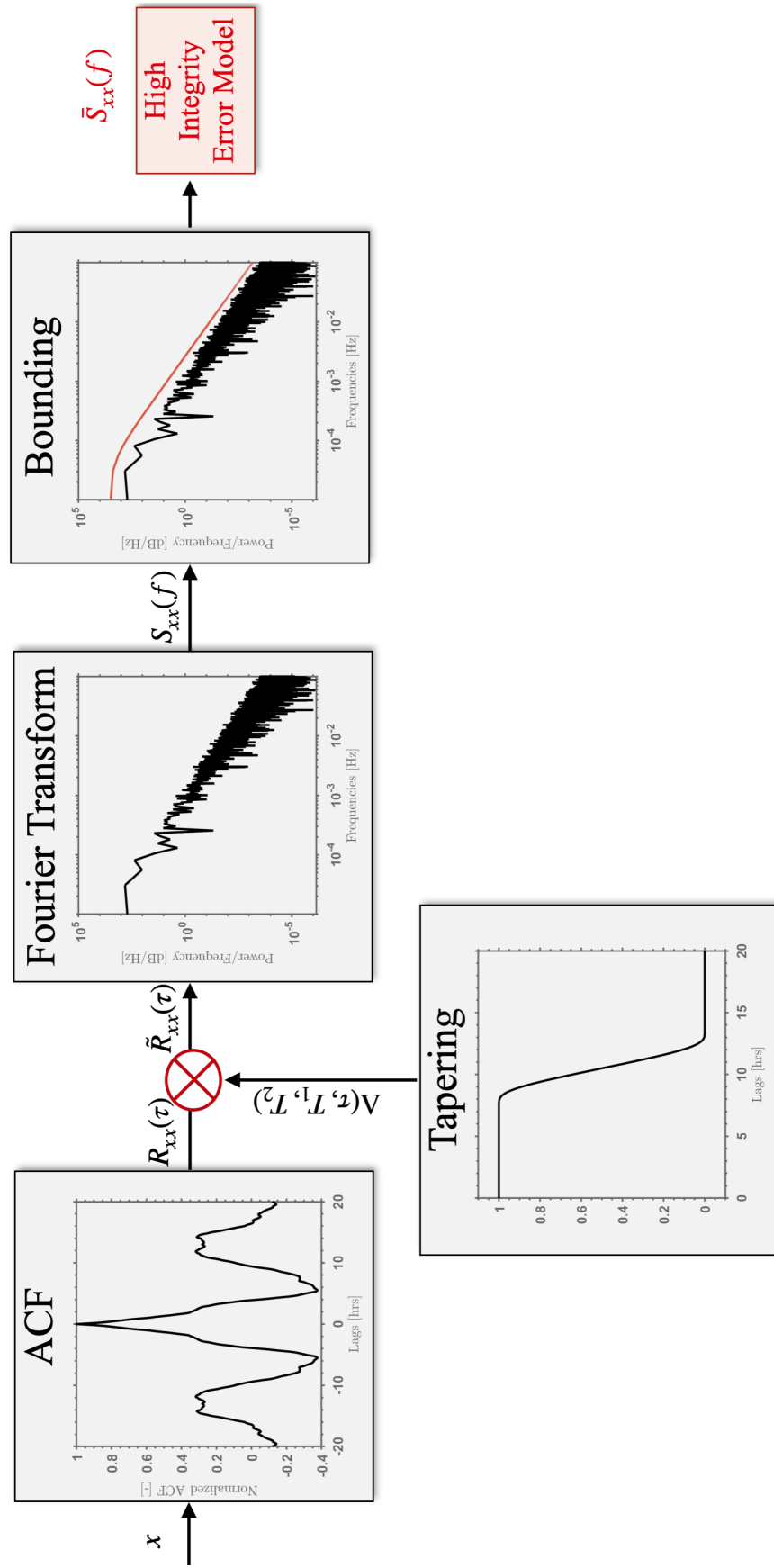


Figure 2.2. PSD Bounding procedure for WSS input

where $\pm T_2$ are the lag times where the window achieves a value of zero and

$$\eta = \begin{cases} 1 - 2\frac{T_1 + \tau}{T_1 - T_2}, & \text{for } -T_2 \leq \tau < -T_1 \\ 1 + 2\frac{T_2 - \tau}{T_1 - T_2}, & \text{for } T_1 < \tau < T_2 \end{cases} \quad (2.12)$$

With this window, ACF values for lag times smaller than T_1 remain untouched, while ACF whose lag time values are larger than T_2 are set to zero. The further away T_1 and T_2 are, the less spectral leakage will impact the PSD estimate. A representation of that window is shown in Figure 2.2, where $T_1 = 7\text{h}$ and $T_2 = 14\text{h}$. The validity and advantages of such window are detailed in [11].

Finally, the sample PSD estimate of the process x can be estimated by taking the Fourier Transform of the windowed ACF. This step is expressed, in discrete form, as:

$$S_x(f) = \sum_{\tau=-T_2}^{T_2} \Lambda(\tau, T_1, T_2) R_{xx}(\tau) e^{-j2\pi f\tau} \text{ for all } f \in \mathbb{R}^+ \quad (2.13)$$

2.2.3 Frequency Domain Bounding of Non-Stationary Input Error Processes. In Section 2.1, for a non-stationary process $x(t)$ at time t over lag time τ , we defined a condition in Equation 2.3 on the *instantaneous* autocorrelation function $\mathcal{R}_{xx}(\tau, t)$. This condition is used to categorize “slow” versus “fast” changing non-stationarity. In this section, we present methodologies for error modeling in each of these cases, which we then illustrate using experimental data in the following chapters.

2.2.3.1 Slowly Varying ACF: Condition 2.3 is Satisfied. If we can evaluate $\mathcal{R}_{xx}(\tau, t)$ using either method (a) or (b) described in Section 2.1.2, then we can also define its instantaneous PSD as [15]:

$$\mathcal{S}_{xx}(f, t) = \int_{-\infty}^{\infty} \mathcal{R}_{xx}(\tau, t) e^{-j2\pi f\tau} d\tau, \quad (2.14)$$

and conversely:

$$\mathcal{R}_{xx}(\tau, t) = \int_{-\infty}^{\infty} \mathcal{S}_{xx}(f, t) e^{j2\pi f\tau} df. \quad (2.15)$$

Let us assume a KF designed using $\overline{\mathcal{S}}_{xx}(f, t) \neq \mathcal{S}_{xx}(f, t)$.

Following the development for the time-varying KF with stationary input process in Section 2.2.2, we can express the output variance as:

$$\sigma_y^2(t) = \int_{-\infty}^{\infty} \int_{-\infty}^{\infty} \overline{h}(\alpha, t) \overline{h}(\beta, t) \mathcal{R}_{xx}(\alpha - \beta, t) d\alpha d\beta, \quad (2.16)$$

which leads to the following equation:

$$\sigma_y^2(t) = \int_{-\infty}^{\infty} |\overline{H}(f, t)|^2 \mathcal{S}_{xx}(f, t) df. \quad (2.17)$$

In this case again, if $\overline{\mathcal{S}}_{xx}(f, t) > \mathcal{S}_{xx}(f, t) \forall f \in \mathbb{R}$, then $\overline{\sigma}_y^2(t) > \sigma_y^2(t) \forall t \in \mathbb{R}^+$.

However, even if $\overline{H}(f, t)$ is time-varying, it is desirable for the input error model PSD $\overline{\mathcal{S}}_{xx}(f, t)$ to be *time-independent*. The reason is that it is difficult, if not impossible, to ensure instantaneously-valid error models using experimental data collected prior to the time the KF is actually implemented.

Thus, we follow a more robust and practical approach: we collect a long, non-stationary, error dataset to capture the time variability in $\mathcal{S}_{xx}(f, t)$. We then determine a time-invariant upper-bounding PSD such that $\overline{\mathcal{S}}_{xx}(f) > \mathcal{S}_{xx}(f, t) \forall t \in \mathbb{R}^+$. This is achieved by dividing a long continuous data set into smaller quasi-stationary subsets that satisfy the condition of Equation 2.3, with center times t_1, t_2, \dots, t_N , to compute $\mathcal{S}_{xx}(f, t_1), \mathcal{S}_{xx}(f, t_2), \dots, \mathcal{S}_{xx}(f, t_N)$. We then find:

$$\overline{\mathcal{S}}_{xx}(f) \geq \max_{1 \leq k \leq N} \mathcal{S}_{xx}(f, t_k). \quad (2.18)$$

In Chapters 3 and 4, we will apply this methodology to orbit and clock, and tropospheric errors, which presents slow non-stationarity. The orbit and clock errors, and tropospheric residuals will be partitioned in stationary sets, and the methodology

described in Section 2.2.2 and Figure 2.2 will be applied to them to obtain bounding models for the orbit and clock, and tropospheric errors.

2.2.3.2 Rapidly Varying ACF with Time-Invariant PSD. This section addresses the case where condition 2.3 is not satisfied and the PSD is not a function of time. This category relates to processes that are non-stationary because they are *unstable* - e.g. $1/f^n$ noises: noise components for which the noise power is inversely proportional to frequency.

In these cases, even if condition 2.3 is not satisfied, the input PSD is not a function of time. It is therefore tempting to directly use Equations 2.17 and 2.18. However, these equations were derived assuming that an instantaneous autocorrelation function was obtainable, i.e., assuming Condition 2.3 was satisfied. Instead, in this section, we evaluate the PSD using periodograms rather than the autocorrelation function. We also assume that the KF error output process is stable (even if the input is not), which would likely be true for any useful KF.

Theoretical development First, we can express the PSD of the output $y(t)$ of a *time-invariant* KF as:

$$\begin{aligned}
 S_{yy}(f) &= \lim_{T \rightarrow \infty} \frac{1}{T} E\{Y_T(f)Y_T(f)^*\} \\
 &= \lim_{T \rightarrow \infty} \frac{1}{T} E\left\{ [\overline{H}(f)X_T(f)] [\overline{H}(f)X_T(f)]^* \right\} \\
 &= |\overline{H}(f)|^2 \lim_{T \rightarrow \infty} \frac{1}{T} E\{X_T(f)X_T(f)^*\} \\
 &= |\overline{H}(f)|^2 S_{xx}(f)
 \end{aligned} \tag{2.19}$$

where the expectation operator $E[\]$ is the expected value operation over the finite duration T , and $X_T(f)$ and $Y_T(f)$ are the *Finite* Fourier Transforms of $x(t)$ and $y(t)$, respectively, expressed as: $Y_T(f) = \int_0^T y(t)e^{-j2\pi ft} dt$.

As long as the output error process $y(t)$ is stable, the following integrals con-

verge:

$$\sigma_y^2 = \int_{-\infty}^{\infty} S_{yy}(f)df = \int_{-\infty}^{\infty} |\overline{H}(f)|^2 S_{xx}(f)df, \quad (2.20)$$

which is the same form as in Equation 2.5, and the same conclusion on variance bounding using a PSD bound $\overline{S}_{xx}(f)$ applies.

Next, we consider the PSD of the output $y(t)$ of a *time-varying* KF, which can be written as:

$$\begin{aligned} S_{yy}(f, t) &= \lim_{T \rightarrow \infty} \frac{1}{T} E\{Y_T(f, t)Y_T(f, t)^*\} \\ &= \lim_{T \rightarrow \infty} \frac{1}{T} E\left\{ [\overline{H}(f, t)X_T(f)] [\overline{H}(f, t)X_T(f)]^* \right\} \\ &= |\overline{H}(f, t)|^2 \lim_{T \rightarrow \infty} \frac{1}{T} E\{X_T(f)X_T(f)^*\} \\ S_{yy}(f, t) &= |\overline{H}(f, t)|^2 S_{xx}(f) \end{aligned} \quad (2.21)$$

Assuming a stable output error process $y(t)$, we can express its variance at time t as:

$$\sigma_y^2(t) = \int_{-\infty}^{\infty} S_{yy}(f, t)df = \int_{-\infty}^{\infty} |\overline{H}(f, t)|^2 S_{xx}(f)df. \quad (2.22)$$

This equation is of the same form as Equation 2.10 and the same conclusion on $\sigma_y^2(t)$ -bounding using an $\overline{S}_{xx}(f)$ applies.

PSD estimation challenges for unstable errors In practice, estimating the PSD $S_{xx}(f)$ from experimental data to derive a model $\overline{S}_{xx}(f)$ is challenging. The first limitation stems from the range of frequencies achievable using observations, which is no greater than:

$$\Delta f \leq f \leq f_N$$

where f_N is the Nyquist frequency defined by the sampling interval Δt : $f_N = \frac{1}{2\Delta t}$. The second limitation is the frequency resolution Δf , which depends on the length of the dataset T_D : $\Delta f = \frac{1}{T_D}$. Therefore, the estimate of $S_{xx}(f)$ is determined by T_D and Δt , or in analogy by the sample rate and the number of samples considered.

In addition, PSD estimates derived from periodograms are impacted by spectral leakage, which can cause PSD bounds to be larger than necessary. In [10, 16] and the previous subsections, PSDs are estimated using Fourier Transforms of ACFs tapered with smooth-edged windows that limit leakage. Unfortunately, this approach does not apply to the case of unstable errors: in this case, PSDs derived from periodograms may be impacted by spectral leakage. In practice, a tapering window could be applied to the data itself, but the impact it would have on the correlation time (and hence the modeling) of the error would need to be studied further.

Additionally, and most importantly, a “loosely” controlled data collection environment (e.g. temperature variations or vibrations) can also contribute to degraded measurements models. For instance, INS manufacturers often provide specifications in the form of sensor error AV curves rather than PSDs. The specification document’s error data is often of great quality, collected in highly controlled and stable environments using temperature and vibration isolation chambers. However, the parameters extracted from these datasets often prioritize model accuracy over integrity, i.e., they are not designed to overbound measurement error distributions. Taking advantage of these high quality curves would be greatly beneficial to our modeling strategy. Therefore, for unstable errors, instead of investigating the periodogram approach further, we will complement PSD bounding with an AV-domain method. This method will be applied to accelerometer and gyroscope errors in Chapter 6.

2.2.4 Allan Variance-Based Error Modeling for Inputs with Fast-Varying Non-Stationarity. In navigation, flicker noises are the most common type of fast-varying non stationarity observed and are usually encountered in one of two scenarios: inertial errors or clock errors. In both cases, they do not appear isolated but are nested amongst all other error sources. The AV approach is therefore often chosen to differentiate and isolate various error contributors present in one data set.

To leverage the results of Equations 2.5, 2.10, 2.17 and 2.22, we must show that a bound in the AV domain also provides a bound in the PSD domain. The relationship between AV (Σ_x^2) and PSD (S_{xx}) can be expressed as [19]:

$$\Sigma_x^2(\tau) = 4 \int_0^\infty \frac{\sin^4(\pi f \tau)}{(\pi \tau f)^2} S_{xx}(f) df \quad (2.23)$$

From Equation 2.23 it is not clear whether the mapping from the PSD domain to AV domain is one-to-one for all S_{xx} [20] (more details on this in Chapter 6). Therefore, the methodology in this subsection will vary depending on the errors encountered:

- Case (a): the errors are such that their mapping between the PSD domain and the AV domain is one-to-one.
- Case (b): one (or more) of the error components' mapping is not one-to one between the PSD and the AV domain.

In case (a), a bounding in the AV domain is a necessary and sufficient condition to ensure a bounding in the PSD domain, and therefore a high integrity model. Therefore, to model the errors of type (a), one can simply upper bound each error component in the AV domain.

In case (b) however, bounding in the AV domain will not be sufficient, and an additional step will be needed to ensure that the bound obtain in the AV domain is also bounding in the PSD domain.

Because such methodologies are so specific to the type of errors encountered, more details are provided in Chapter 6, where this methodology is applied to inertial errors, impacted by (among other things) flicker noises which will be modeled as FOGMRP, hence making the mapping in Equation 2.23 not one-to-one.

2.3 Procedure: making the most out of experimental data

2.3.1 The accuracy versus stationarity dilemma. The following dilemma arises when dealing with sample ACFs (applicable to all inputs apart of those with Fast-Varying Non-Stationarity (cf., section 2.2.3.2)). On the one hand, if we use too little data, the estimation of the expectation function in Equation 2.2 may be noisy and inaccurate. But, on the other hand, if we use very long sets of data, the process may not be stationary over the entire data collection period.

To get some guidance on how much data is needed to obtain an accurate ACF estimate (and later, an accurate PSD estimate), let us analyze the example of a zero-mean FOGMRP with an ACF expressed as:

$$R_{xx}(t) = \sigma_x^2 e^{-|t|/\tau_x} \quad (2.24)$$

where

τ_x is the time constant of the FOGMRP x , and

σ_x^2 is the variance of the random process x .

The variance of the sample ACF (\hat{R}_{xx}) is given by:

$$\sigma_{\hat{R}_{xx}}^2(t) \approx \sigma_x^4 \left(\frac{\tau_x}{T} + \frac{2t + \tau_x}{T} e^{-2t/\tau_x} \right) \quad (2.25)$$

where t is the lag time, τ_x is the process time constant, and T is the length of data used in the estimation of the ACF. This result is derived in Appendix B.

Figure 2.3 presents these standard deviations of the ACF estimates for an example FOGMRP in Equation 2.25 with $\tau_x = 6$ h, $\sigma_x = 1.5$ m. The curves are shown for various lengths of data T (color-coded curves) as a function of lag time (x-axis). Let us assume, for now, that this FOGMRP can be used as a rough approximation of GNSS satellite orbit and clock errors (for instance). The standard deviations

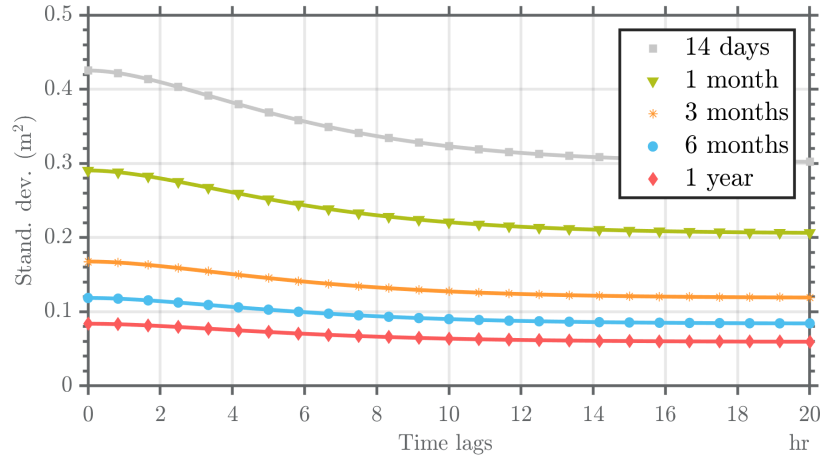


Figure 2.3. Upper bound on standard deviation of ACF estimate ($\tau_x = 6$ h, $\sigma_x = 1.5$ m)

of the ACF estimates (y-axis) are expressed in meters squared because the curves represent variations in orbit and clock error ACF estimation. For example, at lag time zero, the different curves capture the uncertainty in sample variance estimation error as a function of the length of data used. As T increases towards infinity, $\sigma_{\hat{R}_{xx}}$ decreases towards zero: the longer the dataset, the more accurate the ACF estimate will become.

Using 14 days of data, the standard deviation of the ACF estimate is close to 0.3 m^2 at a lag time of 20 hours, whereas using 1 year of data the standard deviation is about 0.06 m^2 at the same lag. The results in Figure 2.3 show that the longer the data set used to estimate the ACF, the lower the uncertainty. However, there appears to be diminishing benefit in using data lengths much longer than 3-6 months. But the question of stationarity testing remains.

2.3.2 Stationarity testing of correlated data. In the case of real data analysis, the number of sample function to analyse is usually limited, and the mean and ACF obtained are only estimates of the errors' true mean and ACF. Therefore, assess-

ing the stationarity of an error from real data cannot be done solely by looking at their estimated mean and ACF but must be done with a more thorough analysis of their statistical properties. In this work, two statistical tests are combined to assess stationarity.

The Levene test [21] is a statistical test that compares the variances of two or more sets of data. It tests the null hypothesis according to which the variances of the populations are equal (homoscedastic). Each data set to be tested for stationarity through the Levene test will be divided into 4 segments. The variances of each of these segments will then be compared to each other.

The two-sample Kolmogorov-Smirnov (KS) test [22] determines whether two sample sets come from the same distribution. In this work, the data sets to be tested with the KS test will be divided into two segments and the distributions of these two segments will be compared to one another.

Taking advantages of these two approaches, we will combine the Levene and the KS test to determine whether a data set is stationary. By combining these two tests, we ensure that the stationarity is verified in terms of variances (Levene test), as well as overall distributions (KS test). Both tests are performed with a 95% confidence level (i.e., p-value of 0.05). If both tests come back positive, the data is considered stationary.

However, both tests assume that the samples are independent. This is not the case for the actual GNSS or INS error data. To approximate the effective number of independent samples we use the properties of a FOGMRP. While the sample data processes are obviously not known to be FOGMRP a-priori, we use this as reasonable approximation (which the data - and their PSDs - will verify later) to determine the effective number of independent samples. Appendix D shows that two samples of a

FOGMRP with time constant τ_x can be considered independent if they are separated by a period larger than or equal to $2\tau_x$. Therefore, to test stationarity, the data is re-sampled at regular $2\tau_x$ intervals, where τ_x is the estimated FOGMRP time constant of the said dataset.

Note that if the process studied is not FOGMRP, a similar approach to the one described in [16] will need to be performed to determine what the number of independent samples is for this specific process type (more details in Appendix D).

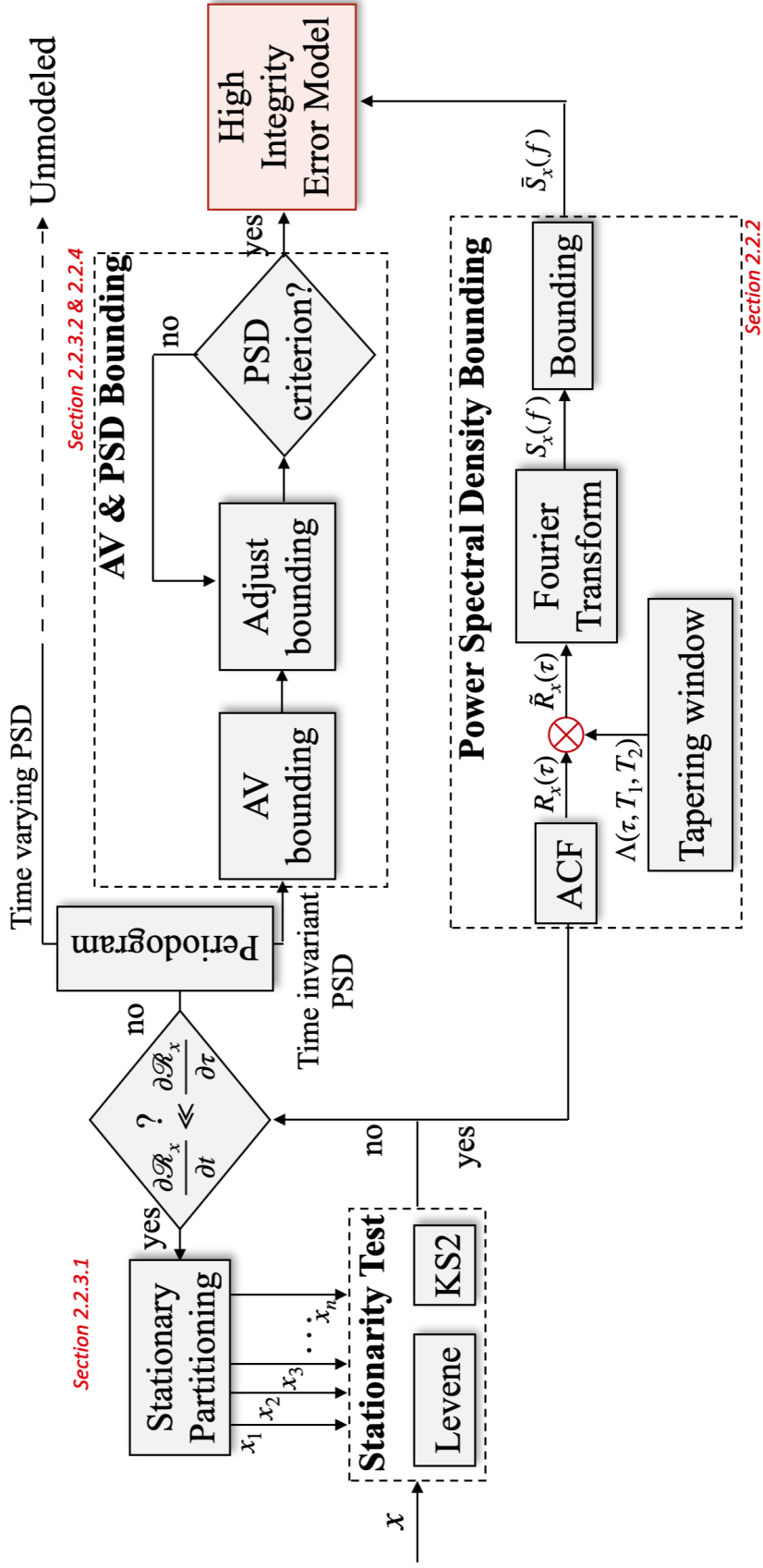


Figure 2.4. Block diagram of the dissertation's high integrity modeling methodology

CHAPTER 3

ORBIT AND CLOCK ERRORS MODELING

In a perfect GNSS positioning scenario, a user's position is estimated by converting the transmission/reception time difference (time of flight) to a distance between the receiver and the satellite (range) and applying trilateration principles between 3 different satellites' ranging estimates. In practice however, this estimation problem is much more complex. A GNSS signal traveling through space will be impacted by various factors. These factors will result in errors in the pseudorange ρ and carrier phase measurements ϕ , used during the position estimation process:

$$\rho_{k,r}^{i,f} = r_{k,r}^i + c (\delta t_{k,r} - \delta t_k^i) + T_{k,r}^i + I_{k,r}^f + \varepsilon_{\rho,k,r}^{i,f} + b_{GD,\rho}^i, \quad (3.1)$$

$$\phi_{k,r}^{i,f} = r_{k,r}^i + c (\delta t_{k,r} - \delta t_k^i) + T_{k,r}^i - I_{k,r}^f + \lambda^f \eta_{k,r}^{i,f} + \varepsilon_{\phi,k,r}^{i,f} + b_{GD,\phi}^i, \quad (3.2)$$

where²

i, f, r, k are satellite, frequency, receiver and epoch indexes, respectively,

$r_{k,r}^i$ is the geometric range between satellite i and receiver r at epoch k ,

c is the speed of light,

$\delta t_{k,r}$ is the receiver clock bias,

δt_k^i is the satellite clock bias,

$T_{k,r}^i$ is the tropospheric delay,

$I_{k,r}^f$ is the ionospheric delay,

$\lambda^f \eta_{k,r}^{i,f}$ is the carrier phase cycle ambiguity,

$\varepsilon_{k,r}^{i,f}$ are the multipath ($\varepsilon_{MP,k,r}^{i,f}$) and thermal noise ($\varepsilon_{TN,k,r}^{i,f}$).

²more complex models exist, however this dissertation will focus on typical model applied to COTS standard receivers.

$b_{GD,\rho/\phi}^i$ are the code/carrier phase group delay impacting the measurements (where $b_{GD,\phi}^i$ is negligible - cf Chapter 7)

Since the ionospheric delay is frequency dependent, pseudorange and carrier phase measurements are often combined in an *iono-free (IF) combination*:

$$\rho_{k,r}^{i,IF} = r_{k,r}^i + c(\delta t_{k,r} - \delta t_k^i) + T_{k,r}^i + \varepsilon_{\rho,k,r}^{i,IF} + b_{GD,\rho}^i, \quad (3.3)$$

$$\phi_{k,r}^{i,IF} = r_{k,r}^i + c(\delta t_{k,r} - \delta t_k^i) + T_{k,r}^i + \lambda^{IF} \eta_{k,r}^{i,IF} + \varepsilon_{\phi,k,r}^{i,IF} + b_{GD,\phi}^i. \quad (3.4)$$

Orbit and clock errors (i.e. residual to the clock and ephemeris products) being the main contributor to ranging errors, these errors are addressed first.³

In the following, we develop new robust sequential models for GNSS satellite orbit and clock errors using PSD bounding. Clock errors are analyzed per satellite clock type: Rubidium (Rb) versus Cesium (Cs) for GPS, and Rubidium Atomic Frequency Standard (RAFS) versus Passive Hydrogen Maser (PHM) for Galileo.

3.1 Orbit and clock errors characterization over time

In this section, we describe the databases and processes used to compute GPS and Galileo satellite orbit and clock errors (based on the keplerian model using clock and ephemeris products as broadcast by the GNSS signal navigation data). Orbit and clock estimates from broadcast navigation data are compared to a reference source (“truth”) after interpolation and coordinate transformation. In addition, we partition the data with respect to satellite clock type. Thirty six months of data were processed (years 2018-2020).

3.1.1 Reference orbit and clocks. Truth data is obtained from the Multi-GNSS Experiment (MGEX) repositories accessible at [24] which provides a posteriori

³The work presented in this Chapter has been published in [23].

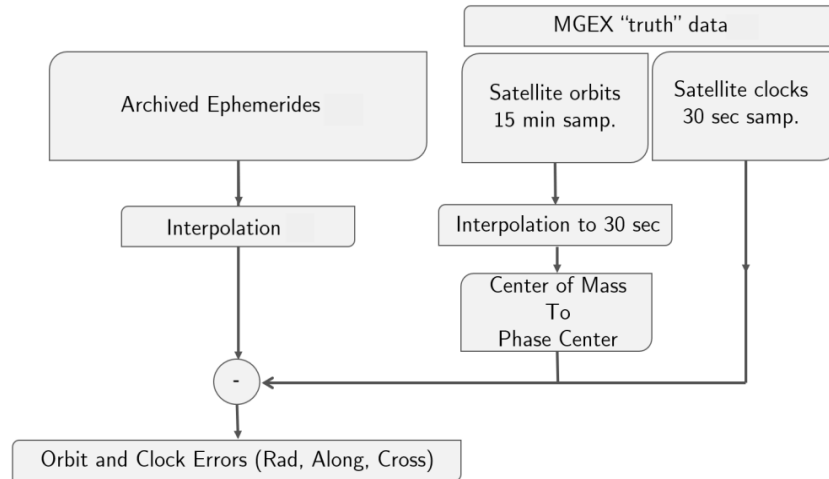


Figure 3.1. Error generation diagram

so called "final products/orbits" describing the true geometric orbits with only a negligible residual error in the order of centimeters remaining. The MGEX service was initiated by the International GNSS Service (IGS) to create a single GNSS data service for multiple core constellations. MGEX is comprised of several ACs which independently compute their own GNSS orbit and clock products. For this work, we used precise orbit and clock data (so called final products) from two ACs: CODE for GPS and CNES for Galileo, both available at the [24] repository, and we consider them to be our truth reference. These reference products have an accuracy of 2.5 centimeters (specified as the one-dimensional mean RMS value over the three geocentric position components). A more detailed analysis of the consistency and accuracy of the MGEX orbit and clock products, as well as references for the GPS and Galileo reference files can be found in [25]. Because we are interested in accurately characterizing orbit and clock errors (and their correlation) over time periods of a few hours (cf Chapter 2 Section 2.2.2.1), the reference orbit' nominal 15-minute sampling period is insufficient. The data was therefore interpolated at 30-second intervals. For this purpose, we used an 8th order Lagrange polynomial following the analysis in [26].

Clock errors are random walk processes and should not be interpolated. Instead, we directly use the IGS reference clock products, which are provided with RMS errors lower than 70 picoseconds at 30-second sample intervals. Note that each clock product is aligned to their AC’s realization of the system time. This means that each Analysis Center (AC) product will be impacted by its own clock bias. Therefore a common clock bias for the AC product in use must be removed from all satellites. Note however, that the data collected was not always continuous due to possible data gaps and/or satellite errors.

3.1.2 Broadcast ephemerides. In the remainder of this work, we follow the GPS ICD standards [27] and use the term “ephemerides” to refer to both orbit *and* clock ephemerides, and more specifically the L/NAV model [28]. Broadcast ephemerides are stored in Receiver INdependent EXchange (RINEX) formats that contain 24 hours of navigation messages. We used Stanford University’s ‘sugl’ files [29] for GPS satellites and ‘brdc’ from CNES [30] for Galileo. These institutions were chosen among several others because their data cleaning and validation algorithms ensure a minimal amount of residual file recording, storing, and labeling errors [31, 32].

3.1.3 GPS and Galileo orbit and clock errors. Satellite orbit and clock errors are obtained by taking the difference between the estimates of the broadcast ephemerides (between a user calculated satellite orbit and clock - based on the satellites navigation message disseminated at that time and their respective models [27,33]) and those of the reference orbits and clocks, as shown in Figure 3.1. Reference orbits are provided with respect to the Center of Mass (CoM) of the satellite, whereas broadcast ephemerides are recorded with respect to the satellite’s Antenna Phase Center (APC). Thus, they need to be converted to the same reference point—in this case, the reference orbits are expressed at the APC. Note that there are 2 conventions to define the APC: the IGS convention and the satellite metadata. The convention

for these offsets can be found at [34], [35] and [36]. More details on these offset corrections can be found at [37]. After correcting for the offsets, orbit and clock errors are obtained by differencing reference and broadcast orbit and clocks. The final errors are then converted to the satellite-referenced local-level radial, along-track, and cross-track frame. Note that each clock product is aligned to their AC's realization of the system time. This means that each AC product will be impacted by its own clock bias. Therefore a common clock bias must be removed from all satellites.

The User Ranging Error (URE) is the projection of the satellite's orbit and clock errors for any user on earth and is the combination of three components:

$$\epsilon_{URE}(\eta) = c_x x(\eta) + c_w w(\eta) + c_v v(\eta) \quad (3.5)$$

where x , w and v are the radial-plus-clock, along track and cross track components, respectively. The weighting factors c_v and c_w are described below with $c_x = \sqrt{1 - c_w^2 - c_v^2}$.

We consider three scenarios. Given R_e the earth radius in kilometers and R_{SV} the satellite's altitude in kilometers, the following limiting cases respectively maximize the contributions of radial/clock, along track, and cross track errors to URE as observed at user's zenith (i.e. satellite nadir):

- Case 1: $c_v = c_w = 0$
- Case 2: $c_v = 0$ and $c_w = \frac{R_e}{R_e + R_{SV}}$
- Case 3: $c_v = \frac{R_e}{R_e + R_{SV}}$ and $c_w = 0$

These cases are represented in Figure 3.2. Note that case 3 represent the cross track equivalent of case 2.

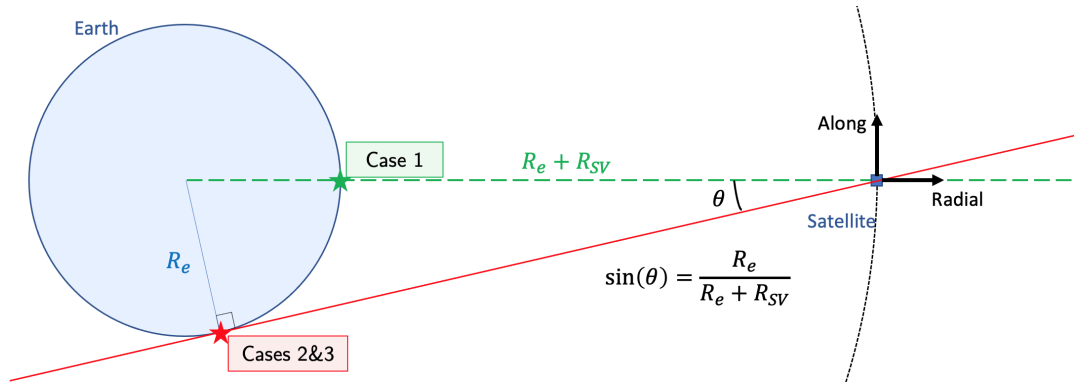


Figure 3.2. Projection of Radial, Along track and Cross track errors onto the user's line of sight.

We processed the orbit and clock errors of GPS (31 active satellites) and Galileo (18 active satellites) over 2018, 2019 and 2020, at a 30 sec sampling rate, which represents about 180 million data points. Figure 3.3 shows the orbit and clock errors of the 31 GPS (grey) and 18 Galileo (black) satellites in December 2019. Orbit and clock error time series for the entire month, for all satellites, for Case 1, are plotted on top of each other.

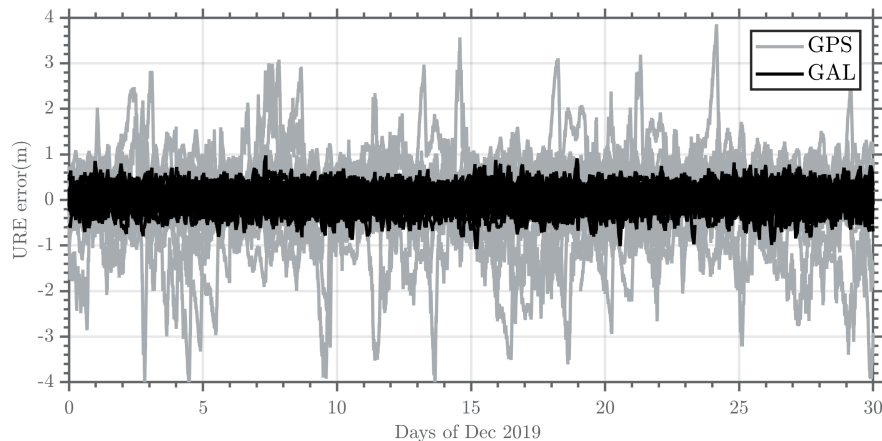


Figure 3.3. Orbit and clock errors for all GPS and Galileo satellites at 30-s intervals in December 2019

GPS ephemerides are nominally broadcast every 2 hours. When a new set of ephemerides is received, the GPS Interface Specifications document stipulates that the previous one is still valid [28], but most users choose to use the most recently

received set as it is a reasonable assumption that a lower age of data will provide, in general, a better quality product. The switch of ephemerides causes an abrupt change in the estimated satellite positions, which can be cumbersome to model in a KF. In response, we adopt an ephemerides switch-over method more amenable to dynamic modelling. We interpolate the broadcast ephemerides in the position domain over the two-hour overlap between the previous and current sets to ensure continuous transitions at ephemerides switch-overs.

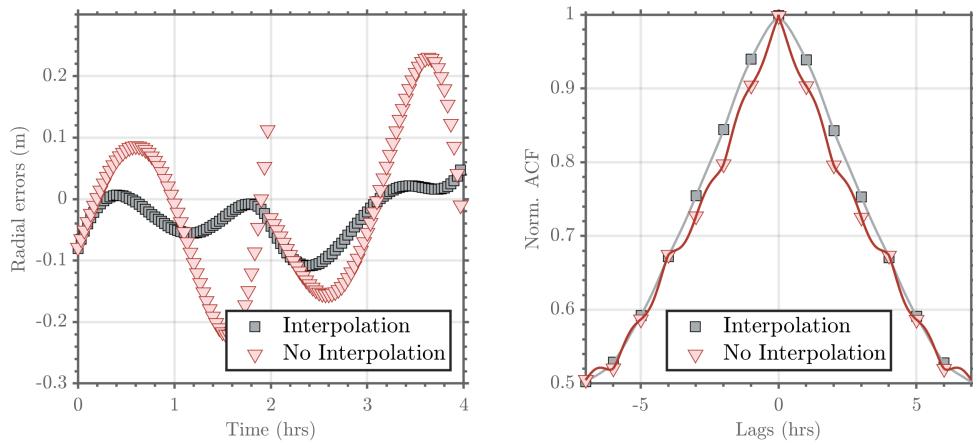


Figure 3.4. Example ephemerides interpolation (radial errors) of GPS PRN07 in December 2018 (left), as well as its impact on radial plus clock error ACF (right)

Figure 3.4 shows an example of radial error for GPS PRN07 interpolated (grey) versus not interpolated (red). The ephemerides jump can be observed for the non-interpolated case at the 2-hour time tag. The process used for Galileo ephemerides is similar, and both are further explained in Appendix A.

Although the interpolated switch-over method does produce much smoother error transitions and is more amenable to modeling in a KF, it does not lead to error spectral characteristics significantly different from those resulting from abrupt switch-overs. The right part of Figure 3.4 shows the (normalized) ACF for interpolated (grey) and not interpolated (red) orbit and clock errors of GPS PRN07. The x-axis

was limited here to 7 hours since it is the longest satellite pass duration (longer correlation times will not impact the user). The choice of interpolation method has minimal influence on the ACFs and therefore will not limit the general applicability of the final error models.

The error models developed in the rest of this section are intended for implementations where the ephemerides are interpolated. However, these error models also apply in applications where the difference between interpolated versus non-interpolated ephemerides is negligible, even if the user does not interpolate ephemerides. For residual error modeling in Space-Based and Ground-Based Augmentation Systems (SBAS and GBAS) that rely on corrections of the un-interpolated ephemerides, this methodology could be re-iterated with un-interpolated ephemerides in order to obtain appropriate models.

3.1.4 Impact of satellite clock type on orbit and clock errors. There are three main types of space-qualified atomic clocks used in GPS and Galileo: Rb or RAFS, Cs, and PHM. GPS satellites have been equipped with several combinations of clocks. GPS blocks II/IIA carried two Cs and two Rb clocks, blocks IIR and IIR-M contained three Rb clocks, and blocks IIF carried two Rb and one Cs clocks. Galileo satellites, on the other hand, use PHM as their primary clocks and RAFS as secondary. Tables 3.1 and 3.2 summarize the GPS and Galileo clocks and block numbers associated with each Pseudo Random Noise (PRN) during the time period of the data we processed. Table 3.1 shows that most GPS satellites used a Rb clock as their main clock. Only two GPS satellites used Cs clocks. Table 3.2 shows that most Galileo satellites were PHM satellites and even though all of them carried RAFS, only 3 used them for the broadcast signals.

A comparison in [38] (Chapter 5) of atomic frequency standards was performed among the GPS and Galileo constellations over timescales ranging from 1 second to 1

Table 3.1. Clocks and blocks of each GPS satellite (March 2018)

PRN	01	02	03	05	06	07	08	09	10	11	12	13	14	15	16	17	18	19	20	21	22	
Clock	Rb	Rb	Rb	Rb	Rb	Rb	Rb	Rb	Rb	Rb	Cs	Rb	Rb	Rb	Rb	Rb	Rb	Rb	Rb	Rb	Rb	Rb
Block	IIR	IIR	IIR	IIR	IIF	IIR	IIF	IIR	IIF	IIR	IIF	IIF	IIF	IIR	IIR	IIR	IIR	IIR	IIR	IIR	IIR	IIR
PRN	23	24	25	26	27	28	29	30	31	32												
Clock	Rb	Cs	Rb	Rb	Rb	Rb	Rb	Rb	Rb	Rb												
Block	IIR	IIF	IIF	IIF	IIF	IIR	IIR	IIF	IIR	IIF												

Table 3.2. Clocks and blocks of each Galileo satellite (March 2018)

PRN	01	02	03	05	07	08	09	11	12	13	14	15	18	19	20
Clock	PHM	RAFS	PHM	PHM	PHM	PHM	PHM	PHM	PHM	RAFS	PHM	PHM	PHM	PHM	PHM
PRN	21	22	24	25	26	27	30	31	33	36					
Clock	PHM	RAFS	PHM	PHM	PHM	PHM	PHM	PHM	PHM	PHM					

day. It showed that stability could vary by as much as a factor 10 and was generally better for the Rubidium and PHM clocks.

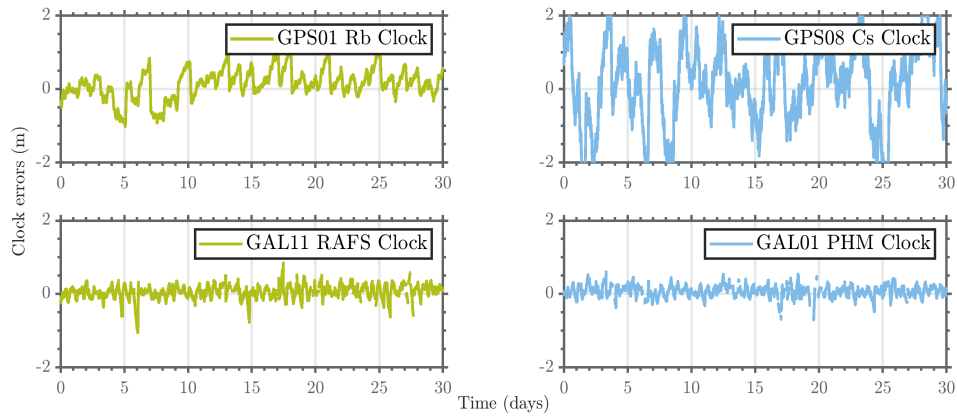


Figure 3.5. GPS and Galileo Orbit and Clock Errors over December 2018

We can illustrate this observation with Figure 3.5, which shows example error time-series at 30-second intervals for each satellite clock type in March 2018, for GPS (top-two charts) and Galileo (bottom-two charts). For GPS, the upper left and right plots show errors for the Rb and Cs clocks on PRN01 and PRN08, respectively. The Rb clock error oscillates within ± 1 m. The Cs clock has larger error variations that reach up to ± 2 m. For Galileo, both PHM and RAFS clock errors have similar behavior and remain between ± 0.5 m. The variations in satellite clock errors are significantly larger in GPS than in Galileo satellites.

In order to model orbit and clock errors using PSD bounding, we must first ensure that they are stationary over the model’s duration.

3.2 Error stationarity analysis

The process described in Chapter 2 is applied in this section onto the orbit & clock error contributors. More specifically, since orbit and clock errors have a ”slowly varying” non stationarity (see later), we apply the methodology of Chapter

2, section 2.2.3.1. For each PRN, the orbit and clock errors of a given satellite over 36 months of data are tested for stationarity. If the dataset is deemed non-stationary, the data is subdivided into stationary datasets. Figure 3.6 shows the statistics of each stationary sub-dataset for 2018 only (for clarity purposes). In some cases, the x-axis shows repeating PRNs. GPS PRN03, for example, is present four times. This means that stationarity tests failed until the dataset was split into four different sets. Note that stationary subsets do not overlap. Also note that due to the analysis shown in Section 2.3.1, we understand the value of using the longest dataset possible. Therefore, the stationarity partitioning begins with the longest dataset available (e.g. 3 years), and reduces its size by partitioning until a stationary subset has been found. Once stationarity is asserted, the partitioned datasets are treated separately.

3.3 Robust modeling of orbit and clock errors

Unlike prior work that provided bounds on the variance of orbit and clock errors for GPS and Galileo [39], we present an approach to modeling these errors over time.

3.3.1 Zero Mean Assumption. This section supports the fact that the orbit and clock errors can be assumed zero mean. Figure 3.6 shows box plots of the error data for each satellite in the GPS (upper) and Galileo (lower) constellations. For clarity in exposition the figure shows results limited to 2018; the rest of this work uses data from 2018, 2019 and 2020. The x-axis indicates the satellite’s PRN number. The color code designates the length of data used to generate the box representation as determined using the stationarity test. The red line inside each box represents the sample median and the upper and lower limits of the box represent the 75th and 25th percentiles, respectively. The dotted lines reaching away from the boxes represent the lowest and highest data points, excluding the outliers, which are represented by colored dots. A point is considered to be an outlier if it is greater than $q_3 + 2.7\sigma(q_3 - q_1)$

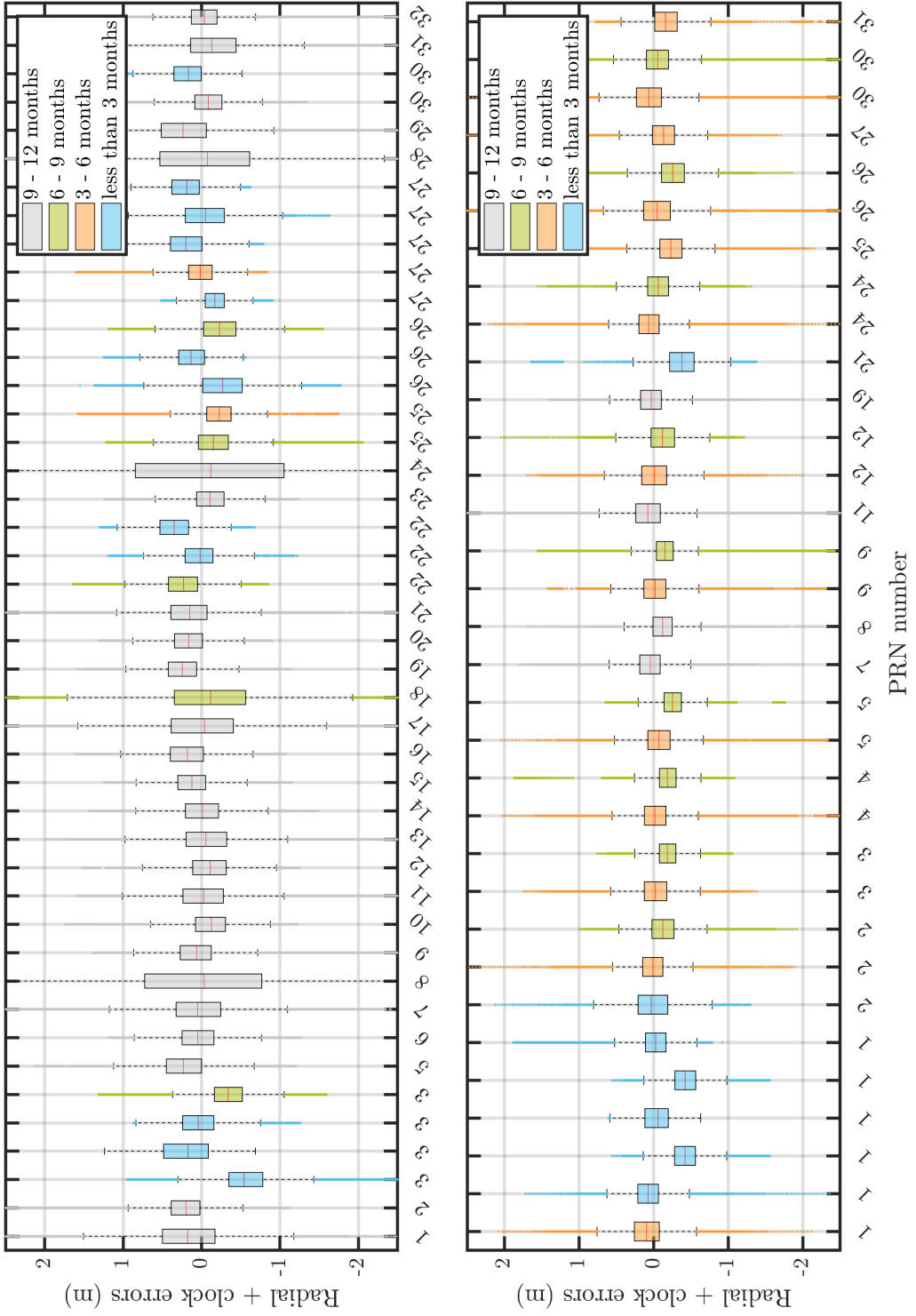


Figure 3.6. Statistics of the 2018 GPS (upper) and GAL (lower) orbit and clock errors stationary subsets

or smaller than $q_1 - 2.7\sigma(q_3 - q_1)$, where q_1 and q_3 are the 25th and 75th percentiles of the sample data. Note that $\pm 2.7\sigma$ corresponds to precisely 99% of the data if it is normally distributed. For both GPS and Galileo, the boxplots appear to be consistent with a zero-mean assumption but will be verified below. It is worth noticing that GPS PRNs 8 and 24, the two Cesium satellites, have much larger error spreads than the rest of the GPS satellites.

In addition, we can obtain the ensemble mean \hat{x} over n stationary data sets for a given constellation.

For each stationary data set x_i , we can take independent samples every $2\tau_i$, and the estimates of the mean \bar{x}_i and variance $\sigma_{\bar{x}_i}^2$ for the data set can respectively be expressed as:

$$\bar{x}_i = \frac{1}{N_i} \sum_{k=1}^{N_i} x_{i,k} \quad (3.6)$$

$$\sigma_{x_i}^2 = \frac{1}{N_i - 1} \sum_{k=1}^{N_i} (x_{i,k} - \bar{x}_i)^2 \quad (3.7)$$

where N_i is the number of independent samples in stationary set x_i , and $x_{i,k}$ is the k^{th} independent sample within x_i . The variance of the error on the mean estimate \bar{x}_i can be written as [15]:

$$\sigma_{\bar{x}_i}^2 = \frac{\sigma_{x_i}^2}{N_i} \quad (3.8)$$

The weighted least squares estimate of the ensemble mean for samples within a constellation is then computed as:

$$\hat{x} = \frac{1}{\sum_i \sigma_{\bar{x}_i}^{-2}} \sum_i \frac{\bar{x}_i}{\sigma_{\bar{x}_i}^2} \quad (3.9)$$

Using orbit and clock error data from 2018 to 2020 (in order to achieve a more accurate estimation), we obtain mean estimates per constellation of $\hat{x}_{GPS} = 1.79$ cm and $\hat{x}_{GAL} = 0.84$ cm. It is important to remember that the IGS reference files are

provided with an accuracy of approximately 2.5 cm. Therefore, the mean estimates (i.e. potential biases) obtained here are negligible.

These results are consistent with those independently obtained in [5], which show that GPS and Galileo radial-plus-clock errors for individual satellites are zero mean over one year. Therefore, we model orbit and clock error as a zero-mean process.

It is worth pointing out that *we do not assert that the errors are zero mean over the duration of a satellite pass* at a given location. Oftentimes they are not, because their correlation time is typically of length similar to that of the longest satellite pass. It is the *underlying parent process* that is zero mean. This is a necessary condition for evaluating PSDs in the next subsection.

3.3.2 Power Spectral Density Bounding. We implement the PSD estimation algorithm described in Chapter 2, Section 2.2.2.1. Because the maximum satellite pass length is in the order of 7h, no user will ever experience orbit and clock error correlations longer than that duration. Hence, the tapering window described in this section is applied to the errors' ACFs with windowing parameters of 7 and 22 hours, respectively, for T_1 and T_2 . A sensitivity analysis on these two parameters is provided in Appendix C. This sensitivity revealed that T_2 values between 14 and 48 hours produce the least spectral leakage. Since the goal is to obtain a bounding FOGMRP model (with parameters σ_x and τ_x) that is as small as possible, an additional analysis was performed to optimize the set of parameters T_2 , σ_x , and τ_x . This analysis can be found in Appendix H and concluded that $T_2 = 22$ hours was optimal for orbit and clock errors.

The left hand-side plot in Figure 3.7 shows the estimated orbit and clock error PSD curves for GPS satellites over the years 2018 to 2020 and for each of the three line-of-sight limit cases selected in Section 3.1.3. The Cs satellites are represented

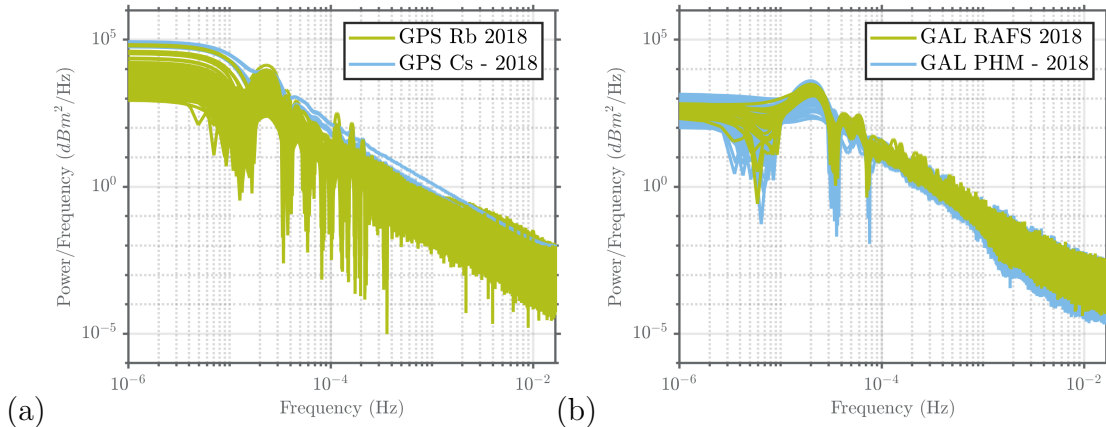


Figure 3.7. PSDs of radial-plus-clock errors for: (a) GPS (b) Galileo

with blue curves and the Rb satellites with green ones. The two clock types can again be clearly distinguished, with Cs curves above the others. The fact that Rb clock curves are lower means that the standard deviation of their errors is also lower, which matches our previous observations and those in [5].

The right hand-side plot in Figure 3.7 shows the same curves for Galileo satellites. As observed before, no clear distinction can be seen between the PHM and the RAFS Galileo satellites.

To robustly model the dynamics of orbit and clock errors (denoted ϵ_{orb}) over time, we upper-bound their PSD using a FOGMRP model. We chose a FOGMRP that is fully determined by two parameters, a time constant τ_{orb} and a standard deviation σ_{orb} , because it can easily be incorporated in a KF, e.g., by state augmentation. Its PSD can be expressed as [17]:

$$S(f) = \frac{2\sigma_{orb}^2/\tau_{orb}}{1/\tau_{orb}^2 + 4\pi^2 f^2} \quad (3.10)$$

Since the two GPS clock types clearly show different trends in the frequency domain, the user may implement different bounding models for each. Figure 3.8 (a) shows the PSD curves for the Rb satellites and its FOGMRP bound. Figure 3.8 (c) shows the same for the Cs satellites. Figures 3.8 (b) and (d) respectively show the bounds for the Galileo satellites RAFS and PHM. If future ARAIM ISM do not identify clock types by satellite, users could access this information via Notice Advisory to NAVSTAR Users (NANU). However, we only processed data for two GPS Cs and three Galileo RAFS satellites. The bounds for satellites with these two clock types could benefit from validation using more data, either from more satellites or over a longer duration.

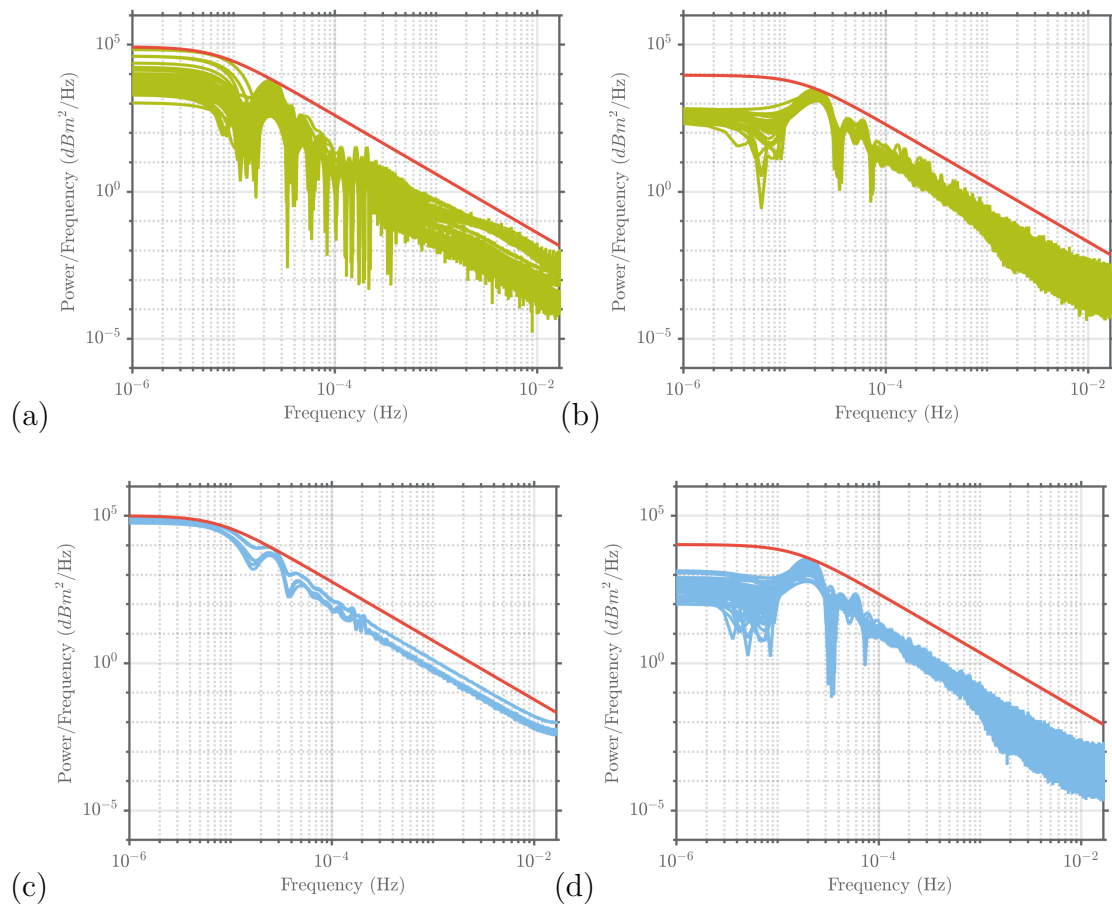


Figure 3.8. PSD bounding of: (a) GPS Rb (b) GAL RAFS (c) GPS Cs (d) GAL PHM

3.3.3 Summary of the Error Model. Table 3.3 summarizes the parameters of the PSD-bounding FOGMRP models. For the GPS constellation, the PSDs of orbit and clock errors were bounded using $\tau_{GPS} = 5.8$ hours and $\sigma_{GPS} = 1.55$ meters. Galileo errors were bounded using $\tau_{GAL} = 3$ hours and $\sigma_{GAL} = 0.7$ meters. For simplicity, those parameters will be referred to as σ_{orb} and τ_{orb} : $\epsilon_{orb} \sim \text{FOGMRP}(\sigma_{orb}, \tau_{orb})$.

Table 3.3. PSD bounding summary: FOGMRP parameters

	τ_{orb} [h]	σ_{orb} [m]
GPS Rb	6.4	1.35
GPS Cs	5.8	1.55
GPS All	5.8	1.55
GAL RAFS	3	0.65
GAL PHM	3	0.7
GAL All	3	0.7

The dynamics of the FOGMRP error model, with parameters σ_{orb} & τ_{orb} , are expressed in discrete form as:

$$x_{k+1} = e^{-\Delta t/\tau_{orb}} x_k + \sqrt{\sigma_{orb}^2 (1 - e^{-2\Delta t/\tau_{orb}})} \omega_k, \quad (3.11)$$

$$\omega_k \sim N(0, 1) \quad \text{and} \quad x_0 \sim N(0, \sigma_{0_{orb}}^2)$$

where $\sigma_{0_{orb}}^2$ is the initial variance of the process.

This model's dynamic equation will be used in Chapter 7, to incorporate the error models in a KF through state augmentation [40].

CHAPTER 4

TROPOSPHERIC DELAY MODELING

Atmospheric errors constitute a major source of ranging error in GNSS. When a GNSS signal travels through the atmosphere, it is delayed and refracted. Ionospheric errors can be removed using dual-frequency signals. However, tropospheric errors are not frequency-dependent and cannot be removed in the same way. The tropospheric contribution to range error in the zenith direction is on the order of 2.4 m. It is made up of “dry” and “wet” components. The dry component is caused by dry gases present in the troposphere, and its magnitude varies with local temperature and pressure. These variations are predictable to a large extent and can, therefore, be modeled accurately. The wet component of the tropospheric delay is caused by water vapor and condensed water, which depends on weather conditions and is therefore less predictable.

In current implementations of GNSS Space-Based and Aircraft-Based Augmentation Systems (SBAS and ABAS) [1, 41–43], the dry and wet components of the zenith tropospheric delay are modeled as functions of the day of the year (to account for seasonal variations) and latitude of the user (to account for geographic variations). The estimated zenith delay is then individually scaled for each satellite by an elevation-dependent mapping function (i.e., obliquity factor). The standard deviation of the residual range error contribution in the zenith direction is specified to be no larger than 0.12 m (as specified by the MOPS algorithm currently in use in SBAS and ABAS [1, 42, 43]).

The literature on high-integrity tropospheric error time correlated models is sparse. The Wide Area Augmentation System (WAAS) MOPS [1] suggests that the

correlation of the tropospheric delay over time be modeled as a FOGMRP with a 30-minute time constant. However, no reference is provided to justify this choice of time constant and no guarantees are provided with regard to integrity. Huang, et al. [44] studied the spatial correlation of the tropospheric error over a 5 km baseline. The work is applicable to differential GNSS systems, but not to inertial navigation or sequential ARAIM. Ibrahim and El-Rabbany analyzed tropospheric residuals relative to the National Oceanic and Atmospheric Administration (NOAA) model using 10 stations in North America [45]. Using a least-squares approach, they estimated the best fit covariance function to the sample autocovariance function of the residuals and developed four different covariance models. These models capture the time correlation of the tropospheric residuals, but they are not designed for high-integrity applications, are limited to North America, and are restricted to complement the NOAA model only.

In response, in this chapter, we develop new, robust models for the tropospheric residuals using data from a worldwide network of ground stations, using the methodology derived in Chapter 2, Section 2.2.3.1. We consider two models: the WAAS/RAIM MOPS tropospheric error model (that will be referred to as “MOPS”) [1], because it is the one that is currently used in GNSS applications of interest (ARAIM and GNSS/INS), and the empirically derived “GPT2w” model [46], because it was initially developed for geodesy applications and is purportedly very accurate.⁴

4.1 Evaluation of tropospheric models

The following sections describe the steps involved in determining the residual errors after application of each of the two tropospheric models.

⁴The work presented in this Chapter has been published in [16].

4.1.1 IGS tropospheric measurements. To obtain the tropospheric residuals, precise tropospheric delay estimates were collected from a set of IGS stations. IGS is an organization of over 200 self-funded agencies, universities and research institutions that provide high precision GPS satellite orbit and clock estimates using a worldwide network of reference stations. These estimates are, in turn, used to develop precise tropospheric products [47], available daily at regular 5-minute intervals and with a 1-sigma accuracy of 4 mm. The product files contain estimates of the tropospheric Zenith Path Delay (ZPD) at each station. We use these ZPDs to compute residuals for the MOPS and GPT2w tropospheric models.

4.1.2 Reference station selection.

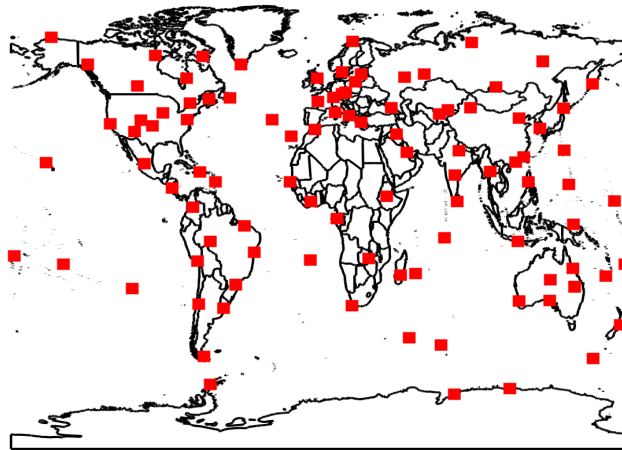


Figure 4.1. Selection of the 100 IGS stations considered in this dissertation

Because tropospheric delay varies with reference station location, the number and distribution of worldwide stations considered in this work are important parameters. If we choose too few stations, then regional variations of the troposphere are not accounted for. But, if we consider too many stations, the data processing time becomes prohibitive. With this tradeoff in mind, we selected 100 stations worldwide.

Their locations are represented in Figure 4.1. The impact of the tropospheric delay on a GNSS signal depends on the day of the year, the receiver’s location and the satellite’s elevation. The errors studied in this work are evaluated over 1 year (2018), at these 100 locations.

4.1.3 MOPS zenith tropospheric delay residuals. The total tropospheric Zenith Tropospheric Delay (ZTD) estimate and its error standard deviation are provided at 5-min time intervals in the IGS tropospheric files. We consider these delay values to be the “true” tropospheric delay. We first analyze residual errors obtained using the MOPS model, computed as:

$$\epsilon_{MOPS} = T_{MOPS} - T_{IGS} \quad (4.1)$$

where:

T_{IGS} is the total tropospheric zenith path delay from IGS, and

T_{MOPS} is the MOPS model estimated zenith path delay.

To compute T_{MOPS} , the user takes as input the day of the year and the user’s latitude. These are used to obtain estimates of various meteorological parameters (via look-up tables), which are then used to estimate the dry and wet tropospheric delays. More details on these computations can be found in [1].

We collected data spanning from January 1 to December 31, 2018 at 5-minute intervals for each of the 100 IGS stations displayed in Figure 4.1. This represents a total of approximately 10.5 million data points. The analysis is carried out for zenith tropospheric delay because they are the random part of the total slant delays perceived by receivers. Slant delays impacting GNSS signals are discussed at the end of this chapter.

Table 4.1 (columns 1 – 4) shows the results obtained for 35 of the 100 stations. High negative latitude stations (e.g. DAV1, CAS1, and PALM) exhibit the largest

Table 4.1. Statistics of MOPS (columns 4-5) and GPT2w (columns 6-7) tropospheric residuals for 35 out of the 100 reference stations over year 2018

STAT.	LAT. [°]	LON. [°]	μ_M [m]	σ_M [m]	μ_G [m]	σ_G [m]
LCK4	26.9	80.9	-0.047	0.122	-0.006	0.048
STK2	43.5	141.8	-0.022	0.080	0.009	0.041
CEDU	-31.9	133.8	-0.076	0.044	0.006	0.040
DAV1	-68.6	78	-0.111	0.022	0.001	0.020
DGAR	-7.3	72.4	0.007	0.047	0.015	0.043
KOKV	22.1	-159.7	-0.019	0.046	0.007	0.044
PALM	-64.8	-64.1	-0.096	0.029	-0.004	0.030
YKRO	6.9	-5.2	-0.027	0.062	-0.009	0.051
MAJU	7.1	171.4	0.064	0.048	0.022	0.045
UFPR	-25.4	-49.2	0.014	0.058	0.007	0.050
NRIL	69.4	88.4	-0.027	0.044	0.003	0.030
LAMA	53.9	20.7	0.005	0.053	0.004	0.033
CAS1	-66.3	110.5	-0.125	0.027	-2x10 ⁻⁴	0.025
SASK	52.2	-106.4	-0.021	0.043	-0.003	0.023
REUN	-21.2	55.6	-0.021	0.048	-8x10 ⁻⁴	0.038
PIE1	34.3	-108.1	-0.003	0.044	-3x10 ⁻⁴	0.024
ZAMB	-15.4	28.3	-0.021	0.061	-0.008	0.036
LAUT	-17.6	177.4	0.021	0.075	-0.003	0.066
LMMF	14.6	-109.3	-0.036	0.048	0.009	0.043
WHIT	60.7	-135.2	-0.001	0.037	0.003	0.022
BAKE	64.3	-96.0	-0.054	0.037	-0.008	0.027
IGAL	63.7	-68.5	-0.054	0.036	-0.010	0.029
RDSD	18.5	-69.9	-0.013	0.047	0.002	0.040
FAA1	-17.5	-149.6	0.004	0.056	0.003	0.045
AREQ	-16.5	-71.5	-0.008	0.033	3.3e-05	0.025
MTV1	-34.9	-56.2	-0.048	0.054	-0.004	0.053
SALU	-2.6	-44.2	0.018	0.046	0.010	0.031
POVE	-8.7	-63.9	0.052	0.057	0.003	0.035
RGDG	-53.8	-67.7	-0.066	0.033	-0.002	0.032
QAQ1	60.7	-46.0	-0.044	0.045	-0.015	0.034
DAKR	14.7	-17.4	-0.091	0.036	-0.009	0.045
WTZA	49.1	12.9	0.018	0.050	0.001	0.031
TROL	69.7	18.9	-0.004	0.048	0.004	0.035
RIGA	56.9	24.1	-7.1e-4	0.038	0.006	0.030
ADIS	9.0	38.8	0.017	0.033	0.002	0.025

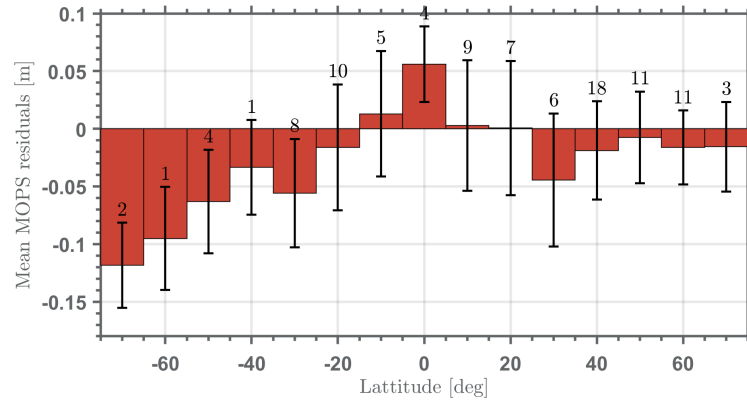


Figure 4.2. MOPS tropospheric residual statistics at 100 reference stations over year 2018

mean error magnitudes, while stations located at low latitude (e.g. DGAR, YKRO, MAJU and SALU) have the smallest means. The error standard deviations remain relatively small at all latitudes.

Figure 4.2 shows yearly mean values and standard deviations in the form of error bars. The tropospheric residuals for the 100 stations over year 2018 were arranged in 10 deg latitude bins. The mean and standard deviation of the binned residuals are represented in the figure. In addition, the number on top of the error bar indicates how many stations were included in each bin. Clearly, there is a latitude dependent bias impacting the MOPS residuals. Residuals for stations located at extreme latitudes have yearly biases reaching about -13 cm, whereas biases at stations between -30 and +30 deg latitude range between -6 and 0.5 centimeters. The MOPS model does not perform as well near the poles as it does near the equator.

Weather - humidity in particular - is also expected to have a large impact on the unpredictability of tropospheric errors. Figure 4.3 (left) shows tropospheric residuals at the KOKV station, which is located in the southeast of Hawaii. In August 2018, Hurricane Lane moved across the Hawaiian Islands and reached Category 5 on August 22 (i.e. Day of Year (DoY) 234). This was the wettest tropical cyclone

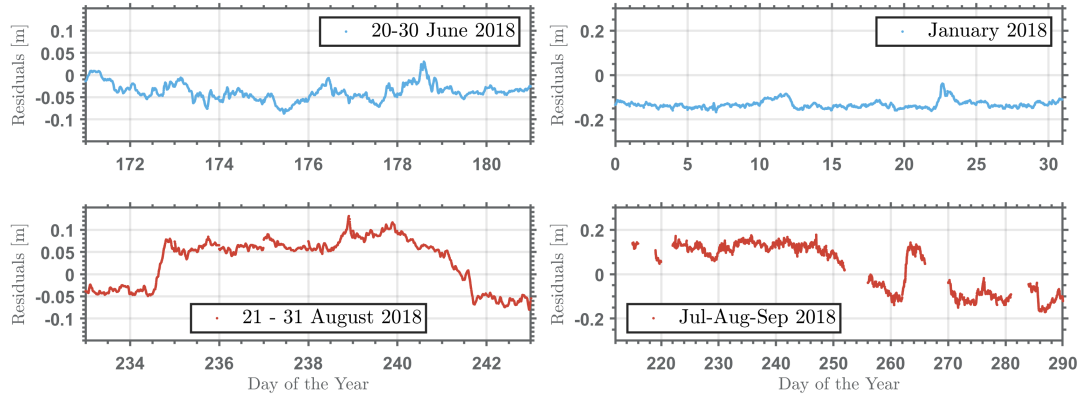


Figure 4.3. Impact of a storm (left) and the rainy season (right) on MOPS tropospheric residuals

on record in Hawaii with rainfall accumulations of up to 1,500 mm. It remained a Category 5 hurricane for 5 days before being downgraded to a tropical depression on August 28 (DoY 240) and dissipating in the following day.

The upper plot in Figure 4.3 (left) represents the tropospheric residuals at KOKV between June 20 and 30, 2018. June was the driest month of the year at this location and is used here as a reference for “nominal” tropospheric conditions. The lower plot in Figure 4.3 (left) shows residuals from August 21 to 31, 2018, at the peak of Hurricane Lane’s activity. On DoY 234, the first day of the hurricane, the residuals mean shifts from -0.05 m to 0.05 m and stays around this value for the entire duration of the storm. When the storm ends on DoY 241, the residuals return to their initial mean of -0.05 m.

We note that extreme hurricanes as described above are rare and do not represent a large portion of weather events that an aircraft may encounter. However, an aircraft may fly over regions that are impacted by rainy seasons.

Figure 4.3 (right) represents the tropospheric residuals of station LCK4 located in the northeast part of India. This area is known for its intense rainy (monsoon)

seasons. In this figure, the upper plot represents the tropospheric residuals during the month of January 2018 (driest month of 2018) and the lower plot represents those same residuals during the months of July, August and September 2018 (wettest months of 2018).

In contrast with the previous location (KOKV), where abrupt changes in weather conditions were observed, LCK4 is located in an area that experiences slowly changing weather conditions. Note that the month of September is the end of the rainy season. This is consistent with the fact that, while the upper plot (dry season) shows constant residuals of -0.13 m, the lower plot varies (positive bias throughout the monsoon season), but slowly converges towards -0.13 m at the end of September. The MOPS model does not take such monthly variations into account, even though they appear and dissipate gradually and are predicable.

Figure 4.2 shows that the MOPS model produces zenith tropospheric residuals that are negatively biased by up to 13 cm at high latitudes. An elevation-dependent mapping function can be used to evaluate the slant delay experienced by a GNSS signal reaching an antenna at elevation angles lower than 90 deg.

The MOPS mapping function is expressed as [1]:

$$m(\theta_k^i) = \frac{1.001}{\sqrt{0.002001 + \sin^2(\theta_k^i)}} \quad (4.2)$$

where θ_k^i is the elevation angle of satellite i at epoch k .

The elevation mapping function takes values ranging from 1 for a satellite at zenith to about 10 for a low elevation satellite. Thus, using the MOPS model, a low elevation satellite signal (i.e., with a mapping function of 10) at a high-latitude location (i.e., observing biases of up to 13 cm) could be impacted by a 1.3-meter bias. Biases this large may become unacceptable for aircraft navigation, especially during

final phases of flight. In the next section, we analyze the tropospheric residual errors using the more accurate GPT2w model.

4.1.4 GPT2w zenith tropospheric delay residuals. The GPT2w blind model is an empirical model of tropospheric delay developed in [46]. The term “blind” refers to the fact that no real time meteorological inputs are required. In this model, the wet delay is computed using predetermined estimates of water vapor pressure, weighted mean temperature, and water vapor decrease factor. In our case, these values were provided in the form of a 1 deg by 1 deg latitude-longitude grid. This grid is used to calculate pressure, temperature, temperature lapse rate, mean temperature of the water vapor, water vapor pressure, hydrostatic and wet mapping function coefficients, water vapor decrease factor, and geoid undulation for specific sites near the Earth surface. Using these parameters, the zenith hydrostatic delay is calculated using the refined Saastomoinen equation from [48] and the zenith wet delay is calculated using the method in [46].

Finally, VMF1 is used with the hydrostatic and wet mapping function coefficients provided with the GPT2w model. Note that contrary to work done in [49], the GPT2w model used here is a dynamic model, which uses the day of the year information to estimate more accurately annual and semi-annual variations in the tropospheric delay’s amplitudes.

Unlike the MOPS model, which only takes the user latitude into consideration, the GPT2w model is a multi-dimensional grid tropospheric delay model using both latitude and longitude.

Using a similar approach to the previous section, the GPT2w zenith tropospheric residuals are computed as:

$$\epsilon_{GPT2w} = T_{GPT2w} - T_{IGS} \quad (4.3)$$

where:

T_{IGS} is the total tropospheric zenith path delay from IGS, and

T_{GPT2w} is the GPT2w model estimated zenith path delay.

Residuals were generated for year 2018 using IGS data at a sampling period of 5 minutes for all 100 stations.

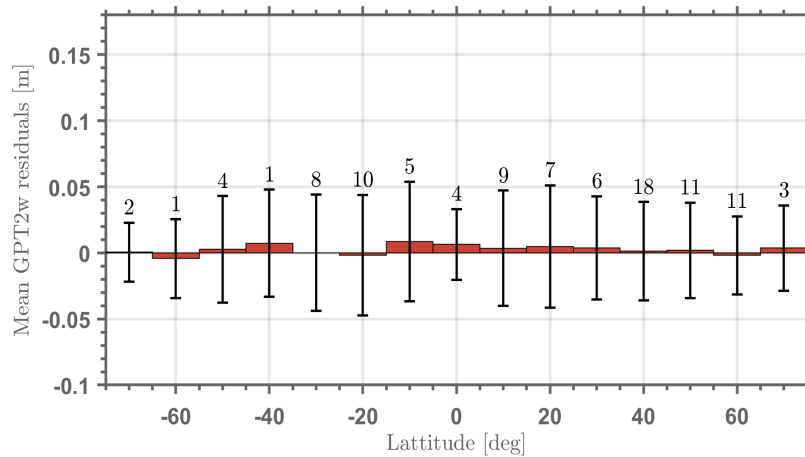


Figure 4.4. GPT2w tropospheric residual statistics at 100 reference stations over year 2018

Figure 4.4 displays the mean values and standard deviations of the GPT2w tropospheric residuals for latitude bins ranging from -70 to 70 deg. The numbers located above the error bars represent the number of stations used to compute the associated bar plot. In comparison to Figure 4.2, the mean values in Figure 4.4 are much lower, on the order of a few millimeters. The standard deviations are also smaller than for the MOPS residuals. It is clear from these results that the GPT2w model globally performs better than the MOPS model.

Columns 5 and 6 of Table 4.1 provides values for the mean and standard deviation of the GPT2w residuals at 35 out of the 100 individual stations. In this case, the stations with the lowest mean values are stations CAS1 (Antarctica) and PIE1 (USA), whereas the largest biases are observed at stations DGAR (Diego Garcia

Islands) and MAJU (Marshall Islands). The mean values of the residuals do not vary significantly with receiver latitude.

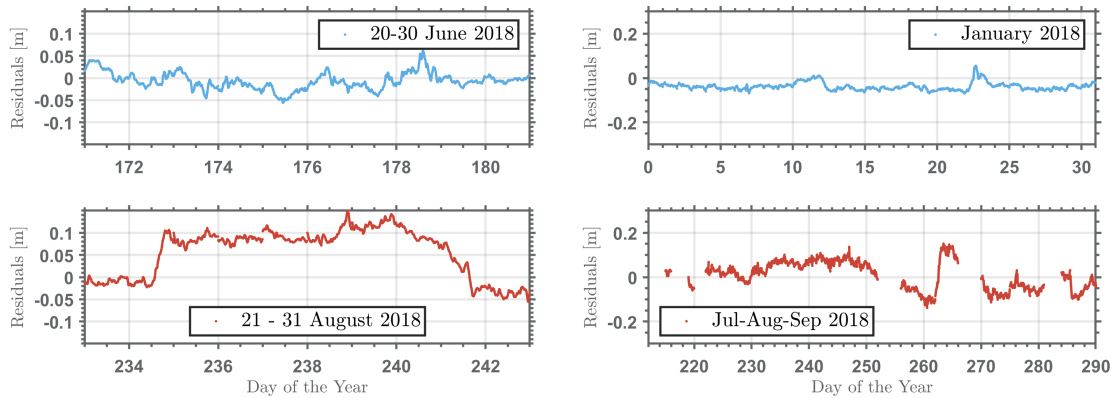


Figure 4.5. Impact of a storm (left) and the rainy season (right) on GPT2w tropospheric residuals

Figure 4.5 (left) shows the tropospheric residuals of station KOKV in June (nominal conditions) and August 2018 (stormy conditions). Mean residual values are close to zero during nominal conditions. Similar to the MOPS residuals in August 2018, the GPT2w residuals change abruptly on DoY 234 (when the storm begins) and move back to normal on DoY 241 (end of the storm). This observation confirms that neither MOPS nor GPT2w can accurately model the tropospheric delay's behavior during an unexpected storm. Figure 4.5 (left) is almost identical to Figure 4.3 (left).

Figure 4.5 (right) represents the tropospheric residuals at station LCK4, located in India. A storm that appears to have happened during DoY 260-265 is still not accurately captured by the GPT2w model. However, between DoY 200 and 260, MOPS tropospheric residuals in Figure 4.3 (right) were shifted by 26 cm from their nominal value because of the monsoon season impacting the troposphere. This shift is corrected by the GPT2w model in Figure 4.5 (right). Indeed, the GPT2w residuals are close to zero during that period.

Figure 4.6 summarizes the error statistics comparison between the MOPS and

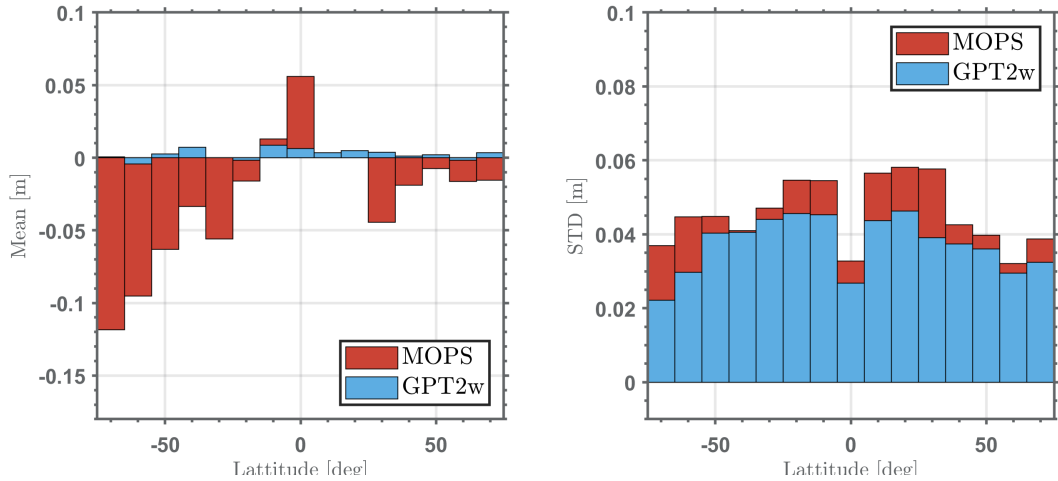


Figure 4.6. Tropospheric models statistics summary

GPT2w models. Yearly means show a clear improvement (especially at high latitudes), and yearly standard deviations of the residuals are slightly improved for GPT2w as compared to the MOPS model, most likely because the GPT2w model accounts for annual and semi-annual variations such as monsoon seasons.

4.1.5 Advantages and drawbacks of each model. The tropospheric model described in the MOPS is derived from the UNB3 model [50]. The UNB3 model is a tropospheric delay model for use in aircraft and does not require estimated meteorological parameters to be input in real-time. Instead, the UNB3 model relies on a 1D latitude-dependent lookup table. One of the main advantages of the MOPS model as compared to the GPT2w model is that it requires low computational power. Because GPT2w requires a search over a 1 deg by 1 deg grid to estimate pressure, temperature, and water vapor information, it performs better but is more computationally expensive.

While the left figures of Figures 4.3 and 4.5 show that sharp changes in air humidity adversely impact tropospheric residuals for both models, overall, the GPT2w model performs much better than the MOPS model. Further analysis of the data

shows that the decimeter-level MOPS zenith residual biases are constant over time, but are location dependent. Thus, modeling MOPS residuals over time will require that both the bias and the random part of the error be accounted for, e.g., using a bias plus FOGMRP model. An alternative solution (chosen in this work) would be to calibrate the MOPS model biases, e.g., using a new lookup table. Or, if the computational burden is acceptable, the GPT2w model may be directly implemented. GPT2w residuals have biases on the order of millimeters and standard deviations on the order of centimeters.

In the remainder of this chapter, both MOPS and GPT2w residuals will be modeled.

4.2 Robust modeling of tropospheric residuals

In order to model the MOPS and GPT2w tropospheric residuals over time, several approaches exist. For example, in [51], ACFs were upper and lower bounded. Unfortunately, time-sequential estimation using ACF bounds requires storage of measurement to state coefficients over time, which quickly becomes memory prohibitive in a GNSS/INS KF implementation [10, 18]. In this chapter we will investigate the alternative approach described in Chapter 2 Section 2.2.3.1, based on partitioning and upper bounding of the residuals' PSD functions.

4.2.1 Stationarity analysis. The models considered are based on stationary FOGMRPs because they are compact parametric realizations that can easily be incorporated in linear estimators, e.g., by state-augmentation in a Kalman filter. Thus, one must first ensure that the data used to find the models parameters is stationary. Various approaches can be implemented to check for stationarity. Here we use the Levene test [21] and the two-sample Kolmogorov-Smirnov test [22].

In Appendix D, we show that two samples of a FOGMRP with time constant

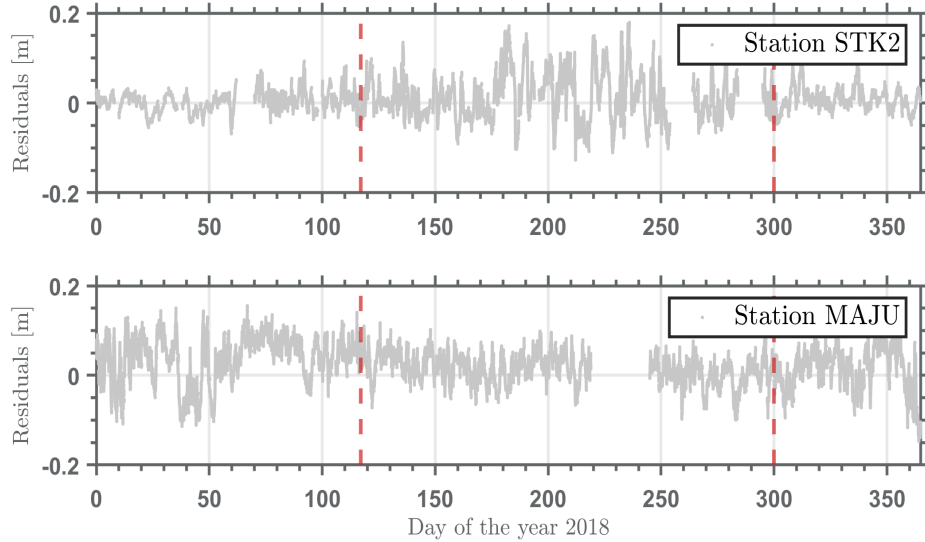


Figure 4.7. Separating data into stationary segments

τ_x can be considered independent if they are separated by a period larger than or equal to $2\tau_x$. While the sample data processes are obviously not known to be FOGMRP a-priori, we use this as reasonable approximation (which the data will actually verify later) to determine the effective number of independent samples. Therefore, to test stationarity, the data was sampled at regular $2\tau_x$ intervals.

For all but six reference stations in Figure 4.1, one year of data was deemed stationarity based on the results comparing 2018 and 2019 data. For GPT2w, residuals from stations STK2 – Japan, MAJU – Marshall Islands, ADIS – Ethiopia, BADG – Russia, CUT0 – Australia, and FUNC - Portugal, were non-stationary over the entire year (2018). Figure 4.7 represents the GPT2w residuals for two of those stations. We can see clear changes of behavior between the winter and summer periods. The summer period was defined for DoYs between 117 and 300 (April 27th to October 27th). For station STK2, a larger standard deviation of the residual can be observed during the summer days. For station MAJU however, the opposite observation can be made. We therefore divided those datasets accordingly and tested winter/sum-

mer sets for stationarity. These tests came back positive. A similar approach was performed for the six non-stationary stations of the MOPS residuals.

4.2.2 Residual mean modeling. The PSD estimation of a random process relies on the assumption that this process is zero mean. In this chapter, we determine whether or not the MOPS and GPT2w residuals must be modeled with a bias.

4.2.2.1 Case 1: MOPS tropospheric residuals. Figure 4.8 shows box plots of the error data for each of the 100 stations studied over the 106 stationary periods. The x-axis represents the station's name. In the boxplot figure, the middle line represents the sample median and the upper and lower limits of the box represent the 75th and 25th percentiles, respectively. The vertical lines reaching away from the box represent the lowest/largest data point excluding the outliers, which are represented by red dots. A point is considered to be an outlier if and only if it is greater than $q_3 + 2.7\sigma(q_3 - q_1)$ or smaller than $q_1 - 2.7\sigma(q_3 - q_1)$, where q_1 and q_3 are the 25th and 75th percentiles of the sample data. The MOPS residuals are clearly not zero mean (as already seen in the previous section, and confirmed in these boxplots), and will need to be modeled as the sum of a bias and a random process.

To model the bias, two approaches are possible. The simplest method would be to use the maximum bias observed over all the stations. Another approach would be to create a latitude/longitude-based model. In this work, we will use the first approach. Station CAS1, located in Antarctica, presented the largest bias, with -0.125 m. This mean will therefore be used to model the bias of the MOPS residuals.

4.2.2.2 Case 2: GPT2w tropospheric residuals. This sub-section aims at providing further evidence, supporting the results in Table 4.1, that the GPT2w residuals can be assumed zero mean. The results in Figure 4.8 validate the zero-mean assumption on the GPT2w residuals because median values are at the centimeter

level, orders of magnitude lower than positioning performance requirements used in air navigation applications.

For the remainder of the development—i.e., the modeling of error dynamics—the residual sample means will be removed prior to error modeling.

4.2.3 Frequency domain modeling: PSD bounding. In this section, we will find a FOGMRP that upper bounds the PSD estimates of the tropospheric residuals.

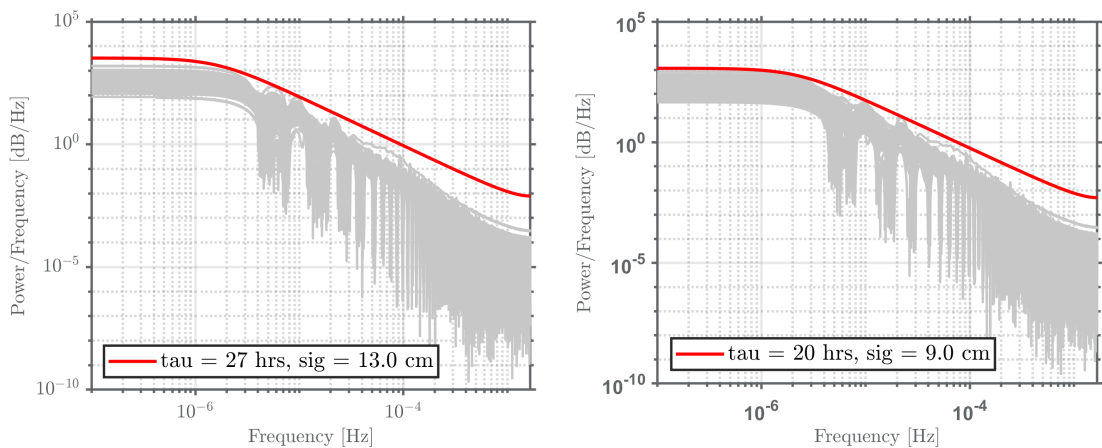


Figure 4.9. PSD bounding of MOPS (left) and GPT2w (right) residuals

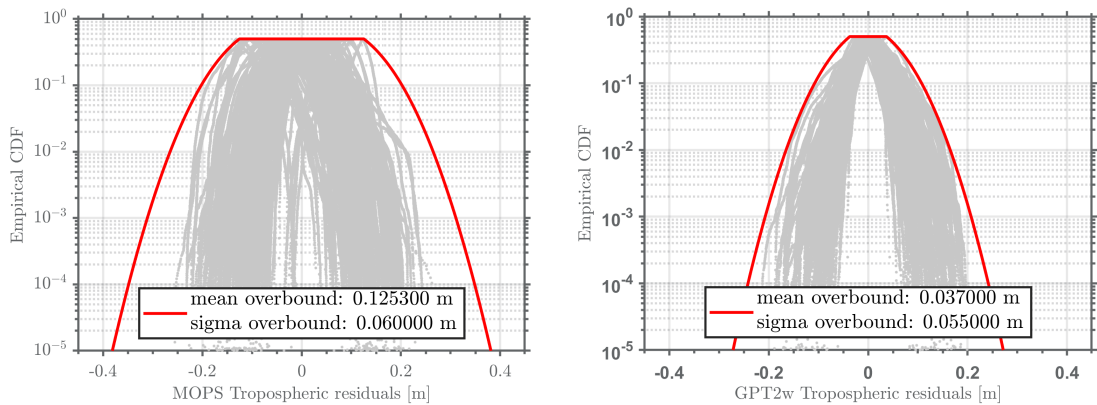


Figure 4.10. MOPS (left) and GPT2w (right) residuals ECDF bounding

To estimate PSDs, multiple approaches exist. We will do so by simply taking Fourier Transforms of the ACFs, multiplied by a tapering window (see Chapter 2,

Section 2.2.2.1). Because the longest flight duration on record is about 18 hours, an aircraft can potentially have to deal with tropospheric error correlation of up to 18 hours. Therefore, we will choose to use a window with $T_1=18$ hours (i.e., the ACF is not modified for lags smaller than 18 hours). To avoid spectral leakage, we optimize the tapering window and use $T_2=54$ hours.

Since the MOPS residuals are clearly not zero mean they need to be modeled as the sum of a bias and a FOGMRP.

In Figure 4.9, the grey curves represent the PSDs of the MOPS (left) and GPT2w (right) tropospheric residuals at each of the 100 stations. The model curves that most tightly bound the MOPS and the GPT2w tropospheric residuals (especially at low frequencies) is a FOGMRP expressed as:

$$S_x(f) = \frac{2}{\tau_T} \frac{\sigma_T^2}{(2\pi)^2 + \frac{1}{\tau_T^2}} \quad (4.4)$$

with a standard deviation of $\sigma_T = 13$ cm and a time constant $\tau_T = 27$ hours for the MOPS model, and a standard deviation of $\sigma_T = 9$ cm and a time constant $\tau_T = 20$ hours for the GPT2w model.

		MOPS	GPT2w
1st order GMRP	Sigma	0.13 m	0.09 m
	Time Constant	27 h	20 h
Gaussian OB	Mean	0.1253 m	0.037 m
	Sigma	0.06 m	0.055 m

Figure 4.11. Summary table on FOGMRP and Gaussian over-bounding (OB)

Figure 4.10 shows the empirical CDFs of residual zenith delay error for of the 100 stations (grey dots). For each of the models, the CDF overbound means have been set to the maximum means observed over each of their respective datasets. For MOPS, as mentioned in chapter IV.B case 1, the overbound mean is 12.53 cm. For the GPT2w residuals, that mean is 3.7 cm. The distributions are not Gaussian, but they can all be upper bounded by a Gaussian CDF with standard deviation of 6 and 5.5 cm (red curve), for MOPS and GPT2w respectively. Thus $\sigma_T = 20$ and 9 cm values obtained to bound the PSDs are also clearly sufficient to over-bound for the non-Gaussian errors contributions as well. These results, along with the FOGMRP bounding results are summarized in Table 4.11.

4.2.4 Summary of the error model. In the rest of this work, we choose to rely on the GPT2w model. Let us express the *slant* tropospheric delay in terms of its hydrostatic (dry, noted $T_{D,k}$) and non-hydrostatic (wet, noted $T_{W,k}$) components:

$$T_k = T_{W,k} + T_{D,k} \quad (4.5)$$

The slant delays can be related to the vertical delays (i.e. ZTD) via a dry and a wet deterministic mapping functions. In this work, the VMF1 mapping functions m_{W_k} and m_{D_k} for the wet and dry ZTD components ($T_{W,k}^{ZTD}$ and $T_{D,k}^{ZTD}$) are used [46]:

$$T_k = T_{W,k}^{ZTD} m_{W_k}(\theta_k^i) + T_{D,k}^{ZTD} m_{D_k}(\theta_k^i) \quad (4.6)$$

The GPT2w model estimates the wet and dry ZTD separately (noted $T_{W,GPT2w,k}^{ZTD}$ and $T_{D,GPT2w,k}^{ZTD}$), with residual errors noted $\delta T_{W,GPT2w,k}^{ZTD}$ and $\delta T_{D,GPT2w,k}^{ZTD}$:

$$T_k = (T_{W,GPT2w,k}^{ZTD} + \delta T_{W,GPT2w,k}^{ZTD}) m_{W_k}(\theta_k^i) + (T_{D,GPT2w,k}^{ZTD} + \delta T_{D,GPT2w,k}^{ZTD}) m_{D_k}(\theta_k^i) \quad (4.7)$$

In this Chapter and in prior work [16], we modeled the post-GPT2w-model residuals without distinction between the wet and dry components. Since the wet component varies faster and more randomly than the hydrostatic component, it is safe to assume that most of the residuals estimated here are wet residuals. Therefore, in the following, the tropospheric delay will be assumed to have the following expression:

$$\begin{aligned} T_k &= (T_{W,GPT2w,k}^{ZTD} + \epsilon_{T,k}) m_{W_k}(\theta_k^i) + T_{D,GPT2w,k}^{ZTD} m_{D_k}(\theta_k^i) \\ &= T_{GPT2w,k} + \epsilon_{T,k} m_{W_k}(\theta_k^i) \end{aligned} \quad (4.8)$$

$T_{W,GPT2w,k}^{ZTD}$ is the total vertical tropospheric delay estimated by the GPT2w model. The FOGMRP used to upper bound the zenith delay residuals of the wet tropospheric residuals ϵ_T (with parameters σ_T and τ_T shown in Figure 4.11) follows the discrete dynamic equation:

$$\begin{aligned} x_{k+1} &= e^{-\Delta t/\tau_T} x_k + \sqrt{\sigma_T^2 (1 - e^{-2\Delta t/\tau_T})} \omega_k, \\ \omega_k &\sim N(0, 1) \quad \text{and} \quad x_0 \sim N(0, \sigma_{0T}^2) \end{aligned} \quad (4.9)$$

where σ_{0T}^2 is the initial variance of the process.

This model's dynamic equation will be used in Chapter 7, to incorporate the error models in a KF through state augmentation [40].

CHAPTER 5

CARRIER PHASE MULTIPATH MODELING

In recent years, multiple papers have been published on the development of bounding error models for aircraft multipath. Considerable advances from both the U.S. side (FAA, Boeing) and the EU side (European Commission, DLR, Airbus) have been made in characterizing and bounding aircraft multipath for the iono-free combinations of both GPS (L1/L5) and Galileo (E1/E5a) measurements [52, 53]. These analyses were performed over multiple hours of flight and with various antennas, aircraft structures and receiver parameters. But all this prior work was focused on the characterization of code or carrier-smoothed-code measurement multipath, and none of it accounted for the time correlation of the multipath errors. Code and carrier-smoothed code measurements are strongly impacted by antenna group delays ($\mathbf{b}_{GD,\rho}$ and $\mathbf{b}_{GD,\phi}$). These delays are deterministic processes: the errors will change according to the antenna's environment, as well as substantial platform reorientations (e.g., turns, banks) and satellite line of sight variation. In principle, this effect is calibratable, albeit not always easily for many platforms of interest, like civil transport aircraft. Although much the same can be said for multipath, in this case error dynamics are highly sensitive to small scale attitude motions and further complicated by a multiplicity of reflective surfaces on platforms with complex shapes, again like transport aircraft, making multipath far more amenable to stochastic modelling. We focus on raw carrier phase measurements because, apart from small, correctable antenna phase center offsets, their platform/antenna dependent errors are restricted to multipath and thermal noise, which can be modelled stochastically in a KF. This chapter describes the methodology employed to first characterize, and then model carrier phase multipath.

Various approaches have been developed historically to characterize multipath. A very well known method is the *Double Difference (DD)* method which consists in differencing carrier phase measurements from two satellites in view, and then from two antennas on the ground. Let us take a moment to look into the DD method and recall Equation 5.1 for the raw carrier phase measurements from satellite i at epoch k received by receiver r on frequency f :

$$\phi_{k,r}^{i,f} = r_{k,r}^i + c(\delta t_{k,r} - \delta t_k^i) + T_{k,r}^i - I_{k,r}^{i,f} + \lambda^f \eta_{k,r}^{i,f} + \varepsilon_{\phi,k,r}^{i,f}, \quad (5.1)$$

Suppose receivers r and u are located in close proximity to one another. Because of their spatial proximity on earth, both receivers will experience similar atmospheric errors (ionospheric and tropospheric delays). The *single difference* of carrier phase measurements for satellite i between these two receivers will remove these atmospheric errors as well as the satellite clock bias (which will be common at any two receivers) to produce the following measurement:

$$\begin{aligned} \phi_{k,r-u}^{i,f} &= \phi_{k,r}^{i,f} - \phi_{k,u}^{i,f} \\ &= r_{k,r-u}^i + c\delta t_{k,r-u} + \lambda^f \eta_{k,r-u}^{i,f} + \varepsilon_{\phi,k,r-u}^{i,f}, \end{aligned} \quad (5.2)$$

where the subscript $r - u$ represents the difference of terms from each receiver (e.g., $r_{k,r-u}^i = r_{k,r}^i - r_{k,u}^i$). The remaining receiver clock terms can be removed by performing a second difference operation, this time between two different satellites in view i and j :

$$\begin{aligned} \phi_{k,r-u}^{i-j,f} - \phi_{k,r-u}^{j,f} &= \phi_{k,r-u}^{i,f} - \phi_{k,r-u}^{j,f} \\ &= r_{k,r-u}^{i-j} + \lambda^f \eta_{k,r-u}^{i-j,f} + \varepsilon_{\phi,k,r-u}^{i,f}. \end{aligned} \quad (5.3)$$

If the relative position vector between the two receivers is known, the range term $r_{k,r-u}^{i-j}$ can be estimated by projecting the vector onto the line-of-sight unit vector to satellite i , and then removed. The cycle ambiguity term $\eta_{k,r-u}^{i-j,f}$ is constant and can

be removed by subtracting off the mean of the residuals obtained over long periods of continuous tracking.

The DD method has isolated a residual carrier multipath component $\varepsilon_{\phi,k,r-u}^{i,f}$ (i.e. the multipath residual in the difference between two receivers and two satellites). For certain applications, for example ones that use double differenced measurements directly for relative positioning, this type of multipath characterization can be sufficient. However, in safety critical applications such as aviation, the multipath error must be characterized for an individual antenna. An airplane may (for redundancy) carry multiple antennas mounted in proximity on top of the fuselage, but they will perceive relatively similar multipath errors, so differencing between them would remove common multipath contributions that are experienced by the individual antennas. In other words, a model based on DD errors presents the risk of not accounting for non negligible contributions to multipath. Therefore, in the remainder of this work, we develop a new method to characterize carrier phase multipath using a dual frequency measurement combination with a single antenna.

5.1 Dual frequency multipath characterization

Let us consider carrier phase measurements from satellite i to receiver r , at epoch k over two frequencies f_1 and f_2 (e.g. GPS L1/L2 and Galileo E1/E5a). Their difference will yield the following residuals:

$$\begin{aligned} \phi_{k,r}^{i,f_1} - \phi_{k,r}^{i,f_2} &= \left(I_{k,r}^{i,f_2} - I_{k,r}^{i,f_1} \right) + \left(\lambda^{f_1} \eta_{k,r}^{i,f_1} - \lambda^{f_2} \eta_{k,r}^{i,f_2} \right) + \varepsilon_{\phi,k,r}^{i,f_1-f_2} \\ &= -I_{k,r}^{i,f_1-f_2} + (\lambda^{f_1} - \lambda^{f_2}) \eta_{k,r}^{i,f_1-f_2} + \varepsilon_{\phi,k,r}^{i,f_1-f_2}. \end{aligned} \quad (5.4)$$

To see multipath error, one has to extract the term $\varepsilon_{\phi,k,r}^{i,f_1-f_2}$ from the residuals of Equation 5.4. Since cycles ambiguities are constant over the course of a satellite pass (assuming the receiver did not lose lock), they are easily removable (i.e. removing the residual mean). The residual ionospheric delay, however, is more tricky and requires

further investigation.

5.2 Ionospheric delay filtering

To separate the ionospheric term $I_{k,r}^{i,f_1-f_2}$, which varies slowly but has large magnitude, from the multipath term $\eta_{k,r}^{i,f_1-f_2}$, which has faster variations but small magnitude, in Equation 5.4, we apply a high pass filter to the residuals, with cut off frequency f_c . The choice of f_c will be paramount to the proper removal of the ionospheric delay from the residuals of Equation 5.4, as well as the quality of the resulting ‘multipath’ observations we obtain after the filtering operation. If f_c is too small compared to the true frequency content of the ionosphere, we take the risk of not removing all of the ionospheric delay and having it impact our final multipath error model, making it too conservative. If f_c is too high, however, we risk removing some of the multipath error we are trying to model, therefore resulting in a model that is not conservative, and may not be bounding either.

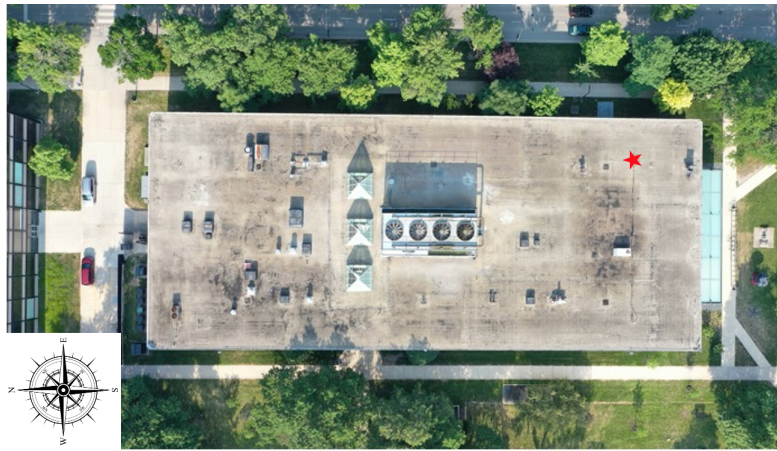


Figure 5.1. Multipath environment of the Rettaliata Engineering building’s rooftop

The first step in our identification of f_c is to isolate ionospheric delay for the location of interest of our data. Throughout this section, results obtained from data collected on the rooftop of the Rettaliata Engineering Building will be shown as a practical application to the methodology developed here. The environment is shown

in Figure 5.1. We obtained a 7-days-long data set collected with our east antenna, under static conditions. Ultimately, the model derived using this data will be used in later chapters, when the KF is run with data from this same environment. However, the methodology developed here is applicable to aircraft flight data as well.

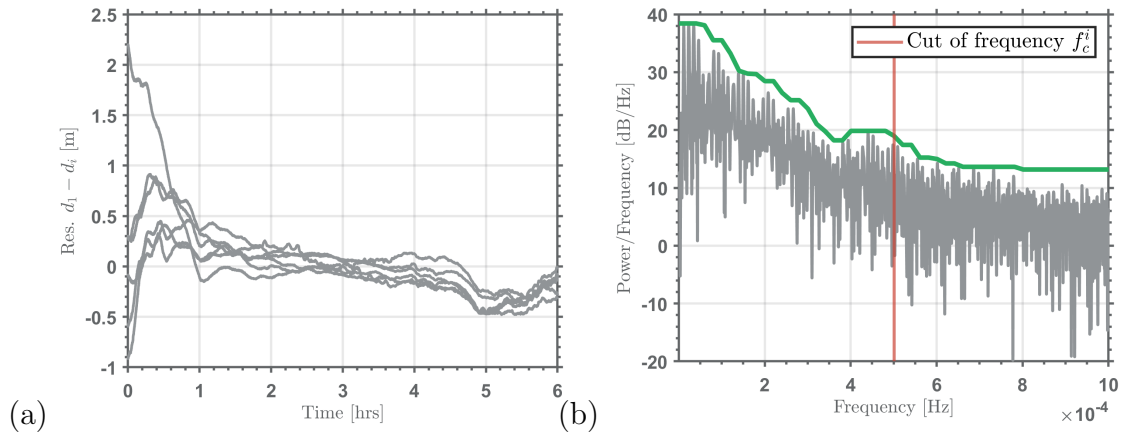


Figure 5.2. Sidereal day differences of $L_1 - L_2$ residuals (a), and their PSD estimate for PRN 07 (b)

To assess the ideal cut off frequency f_c of the ionospheric delay, we need to isolate it from Equation 5.4. To do that, note the difference in periodicity of the two processes present: the multipath (for the static receiver used in this analysis) is repeatable over 1 sidereal day (i.e., the period of the GPS constellation geometry relative to the Earth), which is not the case for the ionospheric delay. To isolate the ionospheric delay, the 7-day data set is divided into sidereal days d_1, \dots, d_7 . The multipath is removed by taking sidereal day differences $d_1 - d_i$, for $i = 2, \dots, 7$. The results consist of ionospheric delays and are represented, for an example PRN07, in Figure 5.2 (a).

Unfortunately, the 7-day-long time series of day-differences is interspersed with gaps due to satellites coming in and out of view. Therefore, traditional PSD estimation methods are out of the question. To estimate the spectral content of the iono-

spheric delay, we instead turn to the Lomb-Scargle periodogram, which is specifically developed to deal with cyclic data impacted by data gaps [54]. The grey curve shown in Figure 5.2 (b) shows the Lomb-Scargle PSD estimate of the ionospheric residual data for PRN 07.

Given a PSD of ionospheric error, it now is necessary to determine the cutoff frequency f_c above which there is negligible power. Ideally, this would be done by choosing the f_c such the area under the PSD curve to the right of f_c is much smaller than the carrier phase multipath error variance. However, the jittery nature of the PSD estimate makes this impractical, requiring that this process be applied to a close overbound (green curve in Figure 5.2 (b)) of the PSD curve. Still the process assumes that the carrier phase multipath error variance is known a-prior, which it is not. A more practical, albeit less rigorous, method using the same PSD overbound is to consider the cutoff frequency to be at approximately the point where the PSD shows a 40dB drop (i.e., 1/100 power). We will proceed with this simpler method to determine f_c^i for each PRN i , but with knowledge that the more rigorous approach can also be applied in a second iteration once an estimate of the carrier phase variance is available.

To ensure the high-pass filtering accounts for all of the ionospheric delay, the final cut off frequency f_c is selected as:

$$f_c = \max_i f_c^i. \quad (5.5)$$

The resulting cut off frequency is $f_c = 1.08 \times 10^{-3}$ Hz (i.e., $\tau_c = 15.4$ min). Figure 5.3 shows the carrier phase multipath obtained after high pass filtering the residuals of Equation 5.4 for each of the satellites in view during 24h.

5.3 Multipath error modeling

To generate high integrity, time correlated error models for carrier phase mul-

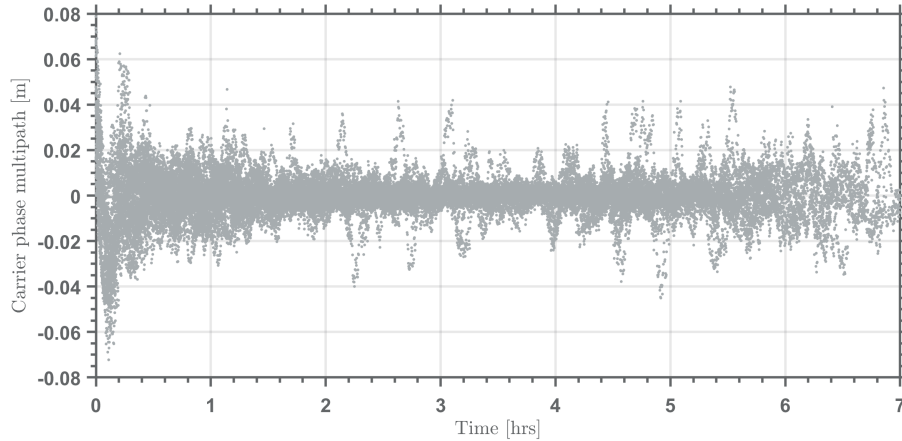


Figure 5.3. Resulting carrier multipath after high pass filtering of the $L_1 - L_2$ residuals (all PRNs)

tipath, we have shown in the methodology section that the first step is stationarity testing and partitioning. Clearly, the time series shown in Figure 5.3 are not stationary since multipath is elevation dependent: low elevation measurements have larger variances than their high elevation counterparts. A common way to resolve this issue is by applying an elevation-dependent mapping function $m_\phi(\theta_k^i)$ to the carrier phase multipath:

$$m_{\phi_k}(\theta_k^i) = a + be^{-\theta_k^i/c}, \quad (5.6)$$

where a , b and c are environment dependent parameters. For the data set under study here, we choose $a = 1$, $b = 2.9$ and $c = 10$. The mapped-multipath residuals $\epsilon_{\phi,k,r}^{i,f_1-f_2}$ are then expressed with respect to $\epsilon_{\phi,k,r}^{i,f_1-f_2}$ as:

$$\epsilon_{\phi,k,r}^{i,f_1-f_2} = m_\phi(\theta^i)\epsilon_{\phi,k,r}^{i,f_1-f_2}. \quad (5.7)$$

Figure 5.4 shows the mapped ($\epsilon_{\phi,k,r}^{i,f_1-f_2}$) and unmapped/raw ($\epsilon_{\phi,k,r}^{i,f_1-f_2}$) carrier phase multipath for an example PRN 07.

The mapped carrier phase multipath of each satellite in view is then tested for stationarity and partitioned accordingly. The stationary segments (of $L_1 - L_2$ multipath) are then converted to the PSD domain and upper bounded as the sum of

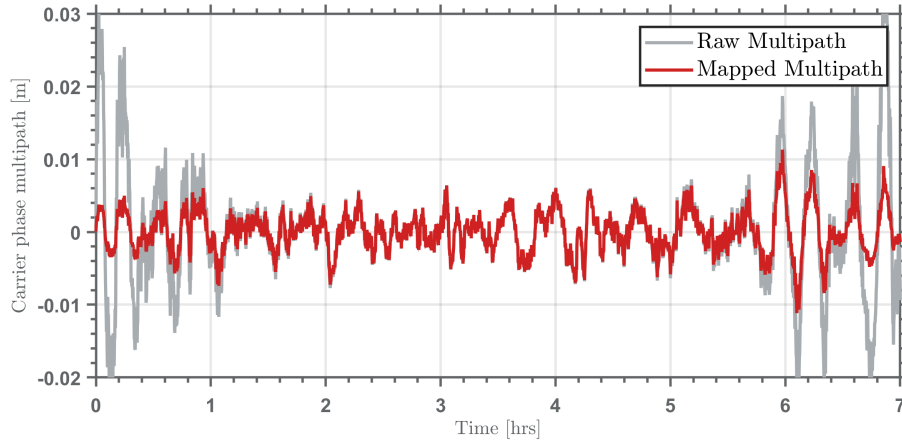


Figure 5.4. Mapping of the carrier phase multipath for PRN 07

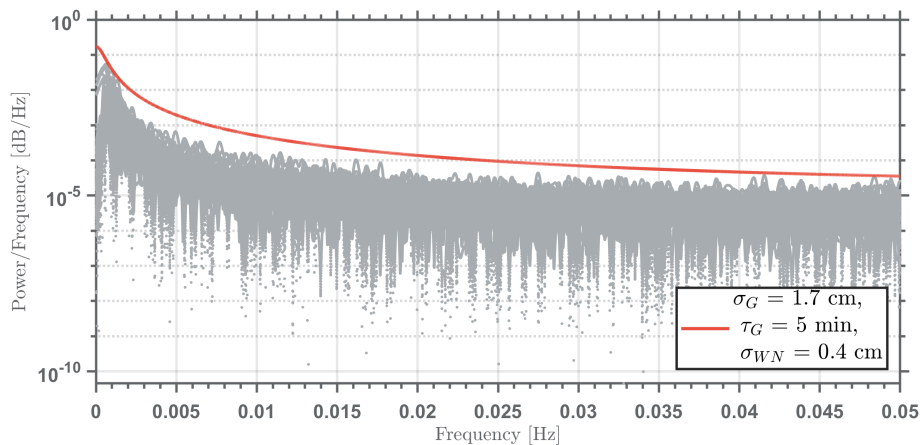


Figure 5.5. PSD bounding of the $L_1 - L_2$ carrier phase multipath

a white noise with $\sigma_{WN} = 0.4$ cm and a FOGMRP with $\sigma_\phi = 1.7$ cm and $\tau_\phi = 5$ min, as represented in Figure 5.5.

5.4 Equivalence to iono-free measurements

The model derived is specific to $L_1 - L_2$ measurement differences. However, KF uses iono-free measurements. This section develops a model for iono-free multipath, based on the model derived above. For the purposes of this derivation, let us simplify the notations as follows:

- ϕ_{IF} is an iono-free carrier phase measurement,
- ϕ_{L_i} is a carrier phase measurement on frequency L_i (e.g. L_1 or L_2 for GPS),
- ϕ_{FD} is a frequency difference measurement: $\phi_{L_1} - \phi_{L_2}$,
- λ_{L_i} is the wavelength associated with frequency L_i .

The iono-free combination is expressed as:

$$\phi_{IF} = \frac{\lambda_{L_1}^2}{\lambda_{L_1}^2 - \lambda_{L_2}^2} \phi_{L_1} - \frac{\lambda_{L_2}^2}{\lambda_{L_1}^2 - \lambda_{L_2}^2} \phi_{L_2}. \quad (5.8)$$

The relationship between the variances can therefore be expressed as:

$$\langle \phi_{IF}^2 \rangle = \left(\frac{\lambda_{L_1}^2}{\lambda_{L_1}^2 - \lambda_{L_2}^2} \right)^2 \langle \phi_{L_1}^2 \rangle + \left(\frac{\lambda_{L_2}^2}{\lambda_{L_1}^2 - \lambda_{L_2}^2} \right)^2 \langle \phi_{L_2}^2 \rangle. \quad (5.9)$$

Assuming independent, identically distributed measurements (which is a conservative assumption to obtain $\langle \phi_{IF}^2 \rangle$), we have $\langle \phi_{L_1}^2 \rangle \approx \langle \phi_{L_2}^2 \rangle$, and therefore:

$$\langle \phi_{IF}^2 \rangle = \left[\left(\frac{\lambda_{L_1}^2}{\lambda_{L_1}^2 - \lambda_{L_2}^2} \right)^2 + \left(\frac{\lambda_{L_2}^2}{\lambda_{L_1}^2 - \lambda_{L_2}^2} \right)^2 \right] \langle \phi_{L_1}^2 \rangle. \quad (5.10)$$

The frequency-difference measurements introduced in this chapter are expressed as:

$$\phi_{FD} = \phi_{L_1} - \phi_{L_2}. \quad (5.11)$$

Their variances can therefore be expressed as:

$$\langle \phi_{FD}^2 \rangle = 2 \langle \phi_{L_1}^2 \rangle. \quad (5.12)$$

Combining Equations 5.10 and 5.12 yields:

$$\langle \phi_{IF}^2 \rangle = \frac{1}{2} \left[\left(\frac{\lambda_{L_1}^2}{\lambda_{L_1}^2 - \lambda_{L_2}^2} \right)^2 + \left(\frac{\lambda_{L_2}^2}{\lambda_{L_1}^2 - \lambda_{L_2}^2} \right)^2 \right] \langle \phi_{FD}^2 \rangle \quad (5.13)$$

5.5 Summary of the error model

The multipath model used in this work has been derived from data collected from an antenna on the rooftop of the Illinois Institute of Technology's Rettaliata Engineering building, in Chicago IL. The experimental KF performance assessment a few chapters later will use data from the same antenna.

Carrier multipath error $\varepsilon_{MP,\phi}$ is modeled as the product of two main components: a deterministic component, which depends on satellite elevation (θ_k^i), and a random component, which depends on the environment of the receiver:

$$\varepsilon_{MP,\phi,k}^i = m_\phi(\theta_k^i)\epsilon_{MP,\phi,k} \quad (5.14)$$

The deterministic component (called a mapping function $m_\phi(\theta_k^i)$) is expressed as:

$$m_\phi(\theta_k^i) = \sqrt{\frac{f_{L1}^4 + f_{L2}^4}{(f_{L1}^2 - f_{L2}^2)^2}} \left(1 + 2.9e^{-\theta_k^i/10}\right), \quad (5.15)$$

where θ_k^i is the elevation of satellite i at time k (in degrees), and f_{L1} and f_{L2} are the (constellation dependent) transmitting frequencies (L1 and L2 for GPS, E1 and E5a for Galileo).

The random component ($\epsilon_{MP,\phi}$) is modeled separately and is propagated as a state in the KF time update. A detailed analysis of this component was performed in this chapter to define a bounding error model for the Rettaliata Engineering building rooftop antenna environment under study. In the analysis, we evaluated carrier phase multipath errors using $L_1 - L_2$ carrier phase data collected at the location shown in Figure 5.1. We used this data to determine that the $L_1 - L_2$ carrier-phase multipath errors could be robustly modeled (i.e., PSD-upper-bounded) using a white noise with $\sigma_{WN} = 0.4$ cm and a FOGMRP with $\sigma_\phi = 1.7$ cm and $\tau_\phi = 300$ sec. The single frequency carrier multipath can therefore be modeled by a white noise with $\sigma_{WN} = 0.28$ cm and a FOGMRP with $\sigma_\phi = 1.2$ cm and $\tau_\phi = 5$ min. The conversion to

iono-free measurements is embedded in the mapping function of Equation 5.15 which will be present in the observation matrix of the Kalman Filter in Chapter 7.

5.6 Application to aircraft multipath

In the case of aircraft carrier phase multipath modeling, two main aspects will differ:

- The dynamics (e.g. pitch, roll, yaw) and dimensions of the aircraft will directly impact the carrier phase multipath.
- The choice of cut off frequency for the ionospheric delay will vary depending on days/times and locations of the flight tests.

5.6.1 Ionospheric delay filtering. The ionospheric cut-off frequency f_c obtained for the rooftop multipath case was specific to the data set collected. Flight data obtained from an airplane flying through different parts of the world on different days will naturally have different ionospheric delays. Therefore, for aircraft flight test data, the process explained in Section 5.2 will need to be performed with data local to the aircraft trajectory.

To do so, IGS [47] provides GNSS measurements from a network of worldwide stations. L_1 and L_2 measurements collected at a station near the aircraft's trajectory on the same days as the data set could be used to reproduce the analysis of Section 5.2 to obtain ionospheric delay estimates and deduce a new data set specific cut off frequency f_c .

Similarly to the work done in Section 5.2, we must ensure that the filtering performed on the residuals will only remove ionospheric delay (and no multipath error). The choice of cut off frequency must be validated. In the case of a static data collection, the frequency content of the multipath was dependent on geometry

changes and distances to reflective surfaces. In the case of in-flight measurements however, the motion and attitude of the aircraft will directly impact the frequency content of the multipath.

In Appendix F, Bessel functions were used to represent the power and frequency content of simulated multipath, and works as follows: let us call f_g the frequency at which the receiver's environment/geometry changes. By scaling the expansion of Bessel multipath expression by f_g , we can observe the frequency distribution of the multipath contribution on a carrier phase measurement. Even though we showed that the frequency content of rooftop multipath and ionospheric delay overlaps and results in a difficult choice of cut off frequency f_c , the aircraft analysis showed that this methodology could still be applied to aircraft in-flight data and yielded better results, with much less overlap and a more fruitful and less risky filtering of the ionospheric delay.

In the case of aircraft multipath, f_g will greatly depend on the phase of the flight (i.e. landing, approach, en route... etc), as well as the attitude of the aircraft (e.g. banking, roll... etc). The Bessel analysis is performed for an example Boeing 747-200 aircraft (specific reflective surface distances), and literature is used to associate an f_g value to various aircraft attitudes.

With these parameters, the Bessel analysis shows that the power distribution of simulated in flight carrier phase multipath is such that the ionospheric delay cut off frequency f_c (specific to Chicago at the time of the static data collection) removed negligible amount of multipath during the ionospheric filtering step.

Given a specific in flight aircraft data set, one can re-apply this analysis to its associated location and time (that will provide ionospheric delay cut off frequency f_c), aircraft type (that will provide the distance measurements needed to simulate

the frequency content of multipath), and aircraft attitude (to estimate f_g) in order to validate the choice of filtering cut off frequency f_c .

5.6.2 Multipath error modeling. In Equation 5.6, we introduced a mapping function that was applied to the multipath errors in order to remove their elevation dependency. The parameters a , b , and c were chosen for that purpose, and are specific to the dataset studied there. For aircraft multipath data, a new set of parameters will need to be selected. Once stationarity is asserted, the time series can be converted to the PSD domain and upper bounded.

CHAPTER 6

INERTIAL ERRORS MODELING

The PSD bounding method is the cornerstone of this dissertation as it allows for the derivation of high integrity, time correlated error models. In particular, the PSD estimation method derived in [11] relies on taking the Fourier Transform of a windowed ACF. However, we showed in Chapter 2 that for certain types of non-stationarity (e.g. fast varying processes with time-independent PSDs), the ACF cannot be used to obtain the PSD. In such cases the error model PSD must be obtained by bounding the periodogram of the errors. But sample periodogram estimates are often noisy which may lead to bounding models that are overly conservative. To improve the quality of the measurements used during the modeling, a method based on AV bounding was also introduced (since manufacturers typically provide AV curves of the sensors errors, obtained from highly controlled tests).

In the first part of this chapter, we introduce the error terms used in our final inertial error models. After a brief reminder on the PSD bounding method and its limitations, the AV bounding methodology is introduced. However, we will also show that AV bounding alone does not ensure integrity, so additional necessary conditions to ensure the integrity of an AV bound are derived.

The second part of the chapter applies these methodologies to an example IMU. Following the procedure detailed in the first part of the chapter, high integrity error models of accelerometers and gyroscopes errors are derived with both methods and compared.

6.1 Methodology: from specifications to bounding model

6.1.1 IMU error model structure. IMU errors are complex stochastic processes that can be modeled differently depending on the application of interest. For high-precision navigation applications, or applications involving long periods of time without external aiding, comprehensive error models are needed. Such models must include the effects of acceleration sensitivity errors, cross-axis sensitivity errors, non-orthogonality errors and installation misalignment errors [55]. In this work, we are primarily interested in inertial-*aided* applications and will therefore restrict ourselves to an error model structure widely-used for this purpose ([12, 56–59]):

$$q_m = (1 + s_f)q_t + b(t) + p(t) + \nu_s(t) \quad (6.1)$$

where q_m is the measured output, which can be that of an accelerometer or gyroscope. The true value of the variable being measured q_t is impacted by a scale factor error s_f , a time-varying bias b , an acceleration/rate random walk (Ac/R-RW) p , and a velocity/angular random walk (V/An-RW) ν_s for an accelerometer/gyro, respectively.

When a noisy sensor output signal is integrated, the result drifts over time due to the accumulation of the noise. This drift is called random walk. For IMU errors, there are two main types of random walk: the angular random walk for gyroscopes, and the velocity random walk for accelerometers. The V/An-RW component is due to thermo-mechanical fluctuations within the sensor and is modeled as additive white Gaussian noise with zero mean. However, in some cases, IMU sensors can also be impacted by an acceleration RW (for accelerometers) or a rate RW (for gyroscopes). In the rest of this paper, this term will be called Ac/R-RW. Their time derivatives can be modeled as:

$$\dot{p}(t) = \nu_p(t) \quad (6.2)$$

where $\nu_p(t)$ is a white Gaussian process, with zero mean and standard deviation σ_p .

The bias component can be expressed as:

$$b(t) = b_r + b_s(t) \quad (6.3)$$

The initial bias of an IMU will be different at each power-up due to signal processing initial conditions and physical properties (thermal, mechanical, and electrical variations). This random variation in initial bias is known as the turn-on bias stability (or bias repeatability) b_r .

The bias stability (or bias instability) b_s is the time-varying component of the bias and measures how much deviation or drift the sensor experiences from its starting value. It is a measure of how stable the bias is over a given time period under constant temperature.

6.1.2 PSD bounding and its limitations. To model the error components in Equations 6.1 to 6.3, data can be collected in the laboratory. These datasets can then be converted to the frequency domain by following the methodology described in Chapter 2, Section 2.2.3.2: using periodograms. To upper bound these errors in the PSD domain, we define a bounding model \bar{S}_{WGR} as (with subscript: WN for white noise, G for FOGMRP, and RW for random walk):

$$\bar{S}_{WGR}(f) = \bar{S}_{WN}(f) + \bar{S}_G(f) + \bar{S}_{RW}(f) \quad (6.4)$$

Each term in this equation can be found in Table 6.1. The velocity random walk ν_s is modeled as white noise with PSD S_{WN} (defined by the parameter N_0), the acceleration random walk p is modeled as a random walk with PSD S_{RW} (defined by the parameter K), and the time-varying bias b is modeled as a FOGMRP with PSD S_G (defined by the parameters σ_G and τ_G). The time-varying bias b is actually a flicker noise (i.e., $1/f$) process, which cannot be modelled in the state space domain, so we instead desire to bound its error contribution using a FOGMRP.

The resulting composite model, although bounding, is likely to be overly-

conservative due to the poor quality of the sample PSD estimates (as shown later, in the experimental section). The following subsections present a second methodology, based on AV curves.

6.1.3 Allan Variance Upper-Bounding Method. The AV domain representation is commonly used in the field of inertial sensor modeling because of its ability to identify and isolate various error components contained in a single dataset. Manufacturers very often rely on AV curves to provide information about their sensors. The curves they provide have often been generated under tightly controlled environments and are therefore of high quality. Taking advantage of these curves in the modeling of inertial sensor errors could therefore be very advantageous.

To leverage the methodology shown in Chapter 2, we must show that a bound in the AV domain also provides a bound in the PSD domain. The relationship between AV and PSD can be expressed as [19]:

$$\Sigma_x^2(\tau) = 4 \int_0^\infty \frac{\sin^4(\pi f \tau)}{(\pi \tau f)^2} S_{xx}(f) df \quad (6.5)$$

Equation 6.5 shows that the mapping from PSD domain to AV domain is one-to-one for all S_{xx} [20].

As already noted, we consider here IMUs three types of errors impacting the IMUs (expressed in both PSD and AV domains in Table 6.1):

- the velocity RW, modeled as a WN,
- the acceleration RW, modeled as a RW, and
- the bias instability, which is flicker noise, but will be conservatively accounted for using a FOGMRP model to enable incorporation in state space realizations.

Appendix E analyses each error type and shows that the inverse mapping from AV to PSD to AV is also one-to-one for WN, flicker noise and RW. But since flicker

Table 6.1. Inertial errors conversion table

Error type	Parameters	Unit	PSD $S_{xx}(f)$	AV $\Sigma_x^2(\tau)$
Flicker noise	σ_F	m/s ²	$\frac{\sigma_F^2}{2\pi f}$	$\frac{2\sigma_F^2}{\pi} \ln(2)$
First order GMRP	σ_G τ_G	m/s ² sec	$\frac{2}{\tau_G} \frac{\sigma_G^2}{(2\pi f)^2 + 1/\tau_G^2}$	$\frac{2\sigma_G^2 \tau_G}{\tau} \left(1 - \frac{\tau_G}{2\tau} \left(3 - 4e^{-\tau/\tau_G} + e^{-2\tau/\tau_G} \right) \right)$
White noise (WN)	N_0	m/s/ \sqrt{h}	$N_0/2$	N_0/τ
Random walk (RW)	K	m/s/h ^{3/2}	$(K/2\pi f)^2$	$K^2 \tau/3$

noises cannot be modeled in the state space domain and must instead be modeled as FOGMRP, we will show here that AV upper bounding does not necessarily imply PSD upper bounding, and that an additional necessary criteria need to be satisfied. We begin by considering two bounding scenarios:

- Case (i): The errors are upper bounded with a white noise and a random walk,
- Case (ii): The errors are upper bounded with a white noise, a random walk, and a FOGMRP.

Both of these cases are represented in a diagram in Figure 6.1. The notations used in this section refer to the ones introduced in Table 6.1. Additionally, let us define $Q := K^2$.

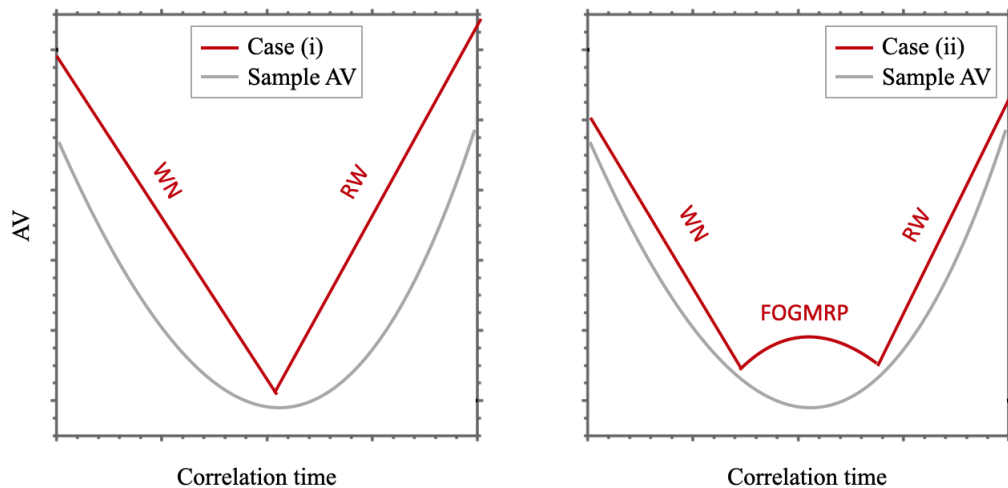


Figure 6.1. Diagram of AV bounding cases

6.1.3.1 Case (i). Let us first consider the case of an error upper bounding consisting of two types of errors: a white noise (WN, with parameter N_0) and a random walk (RW, with parameter Q).

AV Bounding Requirements. We wish to find upper bounding ‘delta’ parameters ΔN and ΔQ such that:

$$\begin{aligned} \bar{\Sigma}_{WN}^2(\tau) + \bar{\Sigma}_{RW}^2(\tau) &= \frac{N_0 + \Delta N}{\tau} + \frac{(Q + \Delta Q)\tau}{3} \\ &> \frac{N_0}{\tau} + \frac{2\ln(2)}{\pi}\sigma_F^2 + \frac{Q\tau}{3} = \Sigma_{WN}^2(\tau) + \Sigma_F^2(\tau) + \Sigma_{RW}^2(\tau) \quad \forall \tau > 0. \end{aligned} \quad (6.6)$$

After simplification and re-ordering, this inequality becomes:

$$\frac{\Delta Q}{3}\tau^2 - \frac{2\ln(2)}{\pi}\sigma_F^2\tau + \Delta N > 0. \quad (6.7)$$

To ensure that no real root exists for τ , we must have:

$$\Delta N \Delta Q > 3 \left(\frac{\ln(2)}{\pi} \right)^2 \sigma_F^4 \approx 0.15\sigma_F^4. \quad (6.8)$$

PSD Bounding Requirements. To ensure integrity, we must also verify that the PSDs of the errors are upper bounded. As in the AV case, we wish to find upper bounding deltas ΔN and ΔQ such that:

$$\begin{aligned} \bar{S}_{WN}(f) + \bar{S}_{RW}(f) &= \frac{N_0 + \Delta N}{2} + \frac{Q + \Delta Q}{(2\pi f)^2} \\ &> \frac{N_0}{2} + \frac{\sigma_F^2}{2\pi f} + \frac{Q}{(2\pi f)^2} = S_{WN}(f) + S_G(f) + S_{RW}(f) \quad \forall f > 0. \end{aligned} \quad (6.9)$$

This, in turn, results in the inequality/condition:

$$\Delta N \Delta Q > \frac{1}{2}\sigma_F^4. \quad (6.10)$$

Deriving an error model by AV bounding will ensure Equation 6.8 is verified, but noting that $1/2 > 0.15$, this does not guarantee PSD bounding. One must take the additional step to meet the condition in Equation 6.10 to guarantee the integrity of the model. This means that either, or both, ΔN and ΔQ will need to be increased. For cases where the flicker noise component σ_F is large, modeling using only a WN and a RW can become very conservative (i.e., loose bounding, as observed in Figure

6.1), motivating the introduction of additional error model to account for the flicker noise.

6.1.3.2 Case (ii). In this case, the upper bound used is comprised of a white noise (to upper bound the velocity random walk), a random walk (to upper bound the acceleration random walk), and a FOGMRP (to upper bound the flicker noise).

AV Bounding Requirements. An upper bounding model in the AV domain would have to verify the inequality:

$$\begin{aligned} \bar{\Sigma}_{WN}^2(\tau) + \bar{\Sigma}_G^2(\tau) + \bar{\Sigma}_{RW}^2(\tau) &= \frac{N_0 + \Delta N}{\tau} + \frac{Q + \Delta Q}{3}\tau \\ &+ \frac{2\sigma_G^2\tau_G}{\tau} \left(1 - \frac{\tau_G}{2\tau} (3 - 4e^{-\tau/\tau_G} + e^{-2\tau/\tau_G})\right) > \frac{N_0}{\tau} \\ &+ \frac{2\ln(2)}{\pi}\sigma_F^2 + \frac{Q\tau}{3} = \Sigma_{WN}^2(\tau) + \Sigma_F^2(\tau) + \Sigma_{RW}^2(\tau) \quad \forall \tau > 0. \end{aligned} \quad (6.11)$$

Let us define the following set of variables:

$$\begin{aligned} x &:= \frac{\tau}{\tau_G}, \quad b := \Delta Q \frac{\tau_G^2}{3} \\ a_G &:= 2\sigma_G^2\tau_G, \quad a_F := 2\sigma_F^2\tau_G. \end{aligned}$$

Equation 6.11 can then be re-arranged as:

$$2bx^3 - \frac{2\ln(2)a_F}{\pi}x^2 + 2(\Delta N + a_G)x - a_G(3 - 4e^{-x} + e^{-2x}) > 0. \quad (6.12)$$

PSD Bounding Requirements. Similar to case (i), additional PSD bounding requirements must be derived:

$$\begin{aligned} \bar{S}_{WN}(f) + \bar{S}_G(f) + \bar{S}_{RW}(f) &= \frac{N_0 + \Delta N}{2} \\ &+ \frac{2}{\tau_G} \frac{\sigma_G^2}{(2\pi f)^2 + \frac{1}{\tau_G^2}} + \frac{Q + \Delta Q}{(2\pi f)^2} > \frac{N_0}{2} + \frac{\sigma_F^2}{2\pi f} + \frac{Q}{(2\pi f)^2} \\ &= S_{WN}(f) + S_G(f) + S_{RW}(f) \quad \forall f > 0. \end{aligned} \quad (6.13)$$

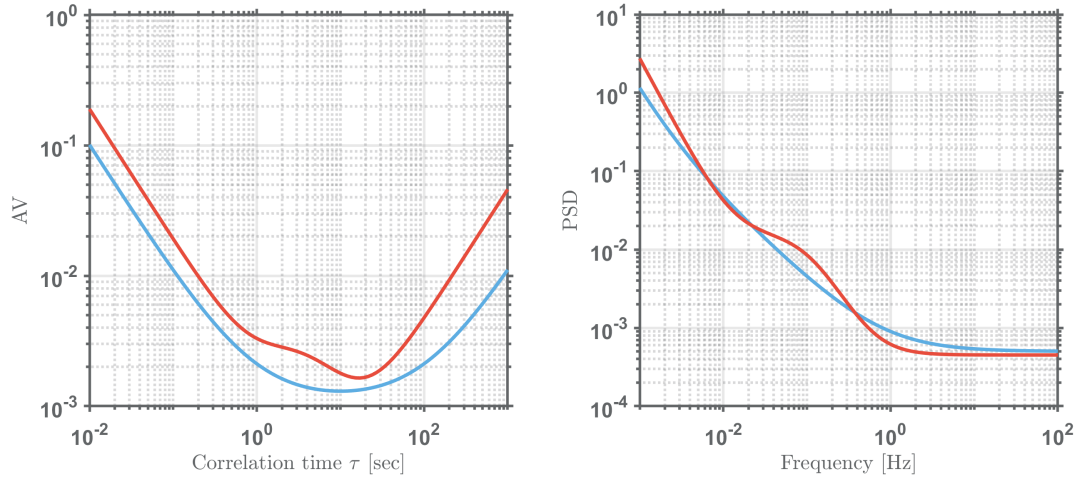


Figure 6.2. Example of failed PSD criterion.

Using the previously defined notation, as well as $u := 2\pi f\tau_G$, and re-organizing the inequality gives:

$$\Delta N u^4 + a_F u^3 + (\Delta N + 2a_G + 6b) u^2 - a_F u + 6b > 0. \quad (6.14)$$

As in case (i), satisfying the AV bounding requirement (here Equation 6.12) does not ensure that the PSD bound (here Equation 6.14) is satisfied. Figure 6.2 shows an example case for which the AV bounding criterion is met (left figure); but the PSD one isn't (right figure).

For case (ii), the steps involved in the development of a high integrity, time correlated error model through the AV domain are represented in Figure 6.3. The manufacturer's data in the AV domain Σ_{WFR}^2 (including a velocity RW, an acceleration RW, and flicker noise) is first upper-bounded by: $\bar{\Sigma}_{WFR}^2 > \Sigma_{WFR}^2$. For the type of processes affecting an IMU, Appendix E shows that the data is also bounded in the PSD domain: $\bar{S}_{WFR} > S_{WFR}$. Since flicker noise cannot be expressed in state space, an additional bound $\bar{\Sigma}_{WGR}^2 > \bar{\Sigma}_{WFR}^2$ is considered, where $\bar{\Sigma}_{WGR}^2$ is the AV of a sum of \underline{WN} , a \underline{FOGMRP} and a \underline{RW} that satisfies Equations 6.12 and 6.14. This model is a high-integrity AV *and* PSD upper-bounding model that can be included

in a KF.

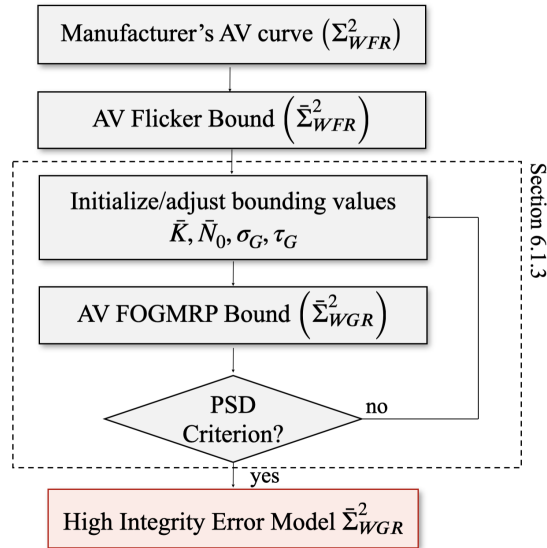


Figure 6.3. FlowChart of the steps involved in AV bounding

6.1.4 Modeling of IMU errors components in a KF. We have so far derived high integrity, time correlated error models for inertial errors via PSD and AV bounding. The component errors are modeled individually using different random processes:

- The velocity/angular random walk (V/An-RW) ν_s is modeled as a white noise with standard deviation σ_s ,
- The acceleration/rate random walk (Ac/R-RW) p is modeled as a RW whose driving noise σ_p can be expressed as: $\sigma_p = K\Delta t$. AC/R-RW are more often defined by their magnitude K .
- The bias instability b_s is a flicker noise. Since flicker noises cannot be modeled in the state space domain, this flicker noise will be modeled using a FOGMRP of parameters σ_{b_s} and τ_{b_s} .

In order to implement the bounding error models in a KF, Equation 6.1 is linearized about the best available estimate of each state, denoted below by an asterisk,

$$\begin{aligned}
q_t &= \frac{1}{1 + s_f} (q_m - b(t) - p(t) - \nu_s(t)) \\
&= h(q_m^*, b^*, p^*, \nu_s^*, s_f^*) + \frac{\delta h}{\delta q_m} \Big|_* (q_m - q_m^*) + \frac{\delta h}{\delta b} \Big|_* (b - b^*) + \frac{\delta h}{\delta p} \Big|_* (p - p^*) \\
&\quad + \frac{\delta h}{\delta \nu_s} \Big|_* (\nu_s - \nu_s^*) + \frac{\delta h}{\delta s_f} \Big|_* (s_f - s_f^*).
\end{aligned} \tag{6.15}$$

Setting $b^* = p^* = \nu_s^* = s_f^* = 0$, we obtain the following linearized model:

$$q_t = q_m - b - p - \nu_s - q_m^* s_f. \tag{6.16}$$

The final, bounding IMU model parameters can now be used in a GNSS/INS KF. An illustrative state propagation equation for a simplified, single-position-coordinate navigation problem using an accelerometer can be expressed as

$$\begin{bmatrix} \dot{x} \\ \dot{v} \\ \dot{b} \\ \dot{p} \\ \dot{s}_f \end{bmatrix} = \begin{bmatrix} 0 & 1 & 0 & 0 & 0 \\ 0 & 0 & -1 & -1 & -q_m^* \\ 0 & 0 & -1/\tau & 0 & 0 \\ 0 & 0 & 0 & 0 & 0 \\ 0 & 0 & 0 & 0 & 0 \end{bmatrix} \begin{bmatrix} x \\ v \\ b \\ p \\ s_f \end{bmatrix} + \begin{bmatrix} 0 \\ 1 \\ 0 \\ 0 \\ 0 \end{bmatrix} q_m + \begin{bmatrix} 0 \\ -\nu_s \\ \nu_{b_s} \\ \nu_p \\ 0 \end{bmatrix}, \tag{6.17}$$

where:

- $\nu_s \sim \mathcal{N}(0, \sigma_s^2)$ is the white noise driving the velocity/angular RW,
- $\nu_{b_s} \sim \mathcal{N}(0, \sigma_{b_s}^2)$ is the white noise driving the FOGMRP bias (in)stability, and
- $\nu_p \sim \mathcal{N}(0, \sigma_p^2)$ is the white noise driving Acceleration/Rate RW with $\sigma_p = K\Delta t$

From a filtering perspective, the presence of p (Ac/R-RW) in the state vector, which the literature and manufacturers sometimes choose to neglect, increases the number of states by 6 (3 accelerometers and 3 gyroscopes) and may complicate the GNSS/INS

integration. Therefore, it may be tempting to use a more conventional model and replace Equation 6.1 with

$$q_m = (1 + s_f)q_t + b(t) + \nu_s(t), \quad (6.18)$$

resulting in the simplified system:

$$\begin{bmatrix} \dot{x} \\ \dot{v} \\ \dot{b} \\ \dot{s}_f \end{bmatrix} = \begin{bmatrix} 0 & 1 & 0 & 0 \\ 0 & 0 & -1 & -q_m^* \\ 0 & 0 & -1/\tau & 0 \\ 0 & 0 & 0 & 0 \end{bmatrix} \begin{bmatrix} x \\ v \\ b \\ s_f \end{bmatrix} + \begin{bmatrix} 0 \\ 1 \\ 0 \\ 0 \end{bmatrix} q_m + \begin{bmatrix} 0 \\ -\nu_s \\ \nu_{b_s} \\ 0 \end{bmatrix}. \quad (6.19)$$

From an integrity perspective, this order reduction is only permissible if the AV of the instrument (accelerometer or gyroscope) does not show evidence of an Ac/R-RW component. In the rest of this chapter we will present a methodology to estimate the parameters in the more general model of Equation 6.17.

6.2 Experimental evaluation

IMU errors are environment-dependent and can vary with factors including temperature, vibrations, and motion. Generating IMU error models that represent multiple possible scenarios requires costly equipment (e.g., temperature chamber, vibration table, rotation table, etc.) and multiple datasets. In this work, we focus on breaking down and modeling IMU performance for static, constant-ambient-temperature data. The same concepts can be used in other testing environments.

6.2.1 Data collection setup. In this section, we apply the methodology presented above to IMU data from a Sensoror STIM-300. The STIM-300 is a small, tactical grade, low weight, high performance IMU that contains 3 highly accurate MEMS gyros, 3 high stability accelerometers and 3 inclinometers. The IMU is factory calibrated and compensated over its entire operating temperature range (-40°C to $+85^\circ\text{C}$). More details on this IMU can be found in [60].

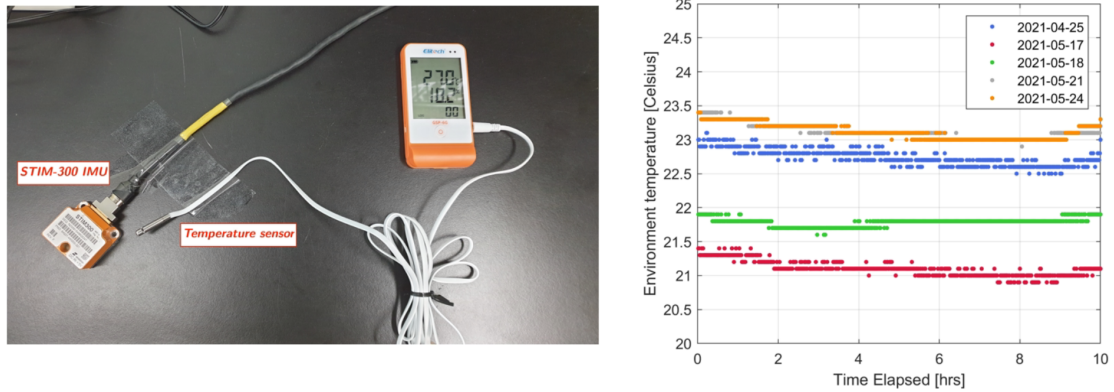


Figure 6.4. Experimental set up (left) and environment's temperatures (right)

Data collection was performed over multiple 10 h-long periods in static conditions at a 125 Hz sampling frequency. To monitor environmental temperature variations and ensure that they did not exceed the variations that can be compensated by the IMU, a temperature sensor was placed next to the IMU (see Figure 6.4). Five of these data sets satisfied the criterion $\Delta T \leq 1^\circ\text{C}/10\text{ h}$ and were used in the following work.

6.2.2 Accelerometer errors. In Chapter 2, we introduced the limitations of the PSD bounding approach for non-stationary processes with time invariant PSDs, and introduced another approach based on AVs. In this section, we apply these two methodologies to the accelerometer errors of the STIM-300 IMU, using the datasets mentioned above and the IMU's specification document.

6.2.2.1 Modeling through PSD bounding. The PSDs derived from these sets using periodograms are represented in gray in Figure 6.5.

To upper bound these errors in the PSD domain, we define a bounding model \bar{S}_{WGR} as (with subscript: \underline{WN} for white noise, \underline{FOGMRP} , and \underline{RW}):

$$\bar{S}_{WGR}(f) = \bar{S}_{WN}(f) + \bar{S}_G(f) + \bar{S}_{RW}(f) \quad (6.20)$$

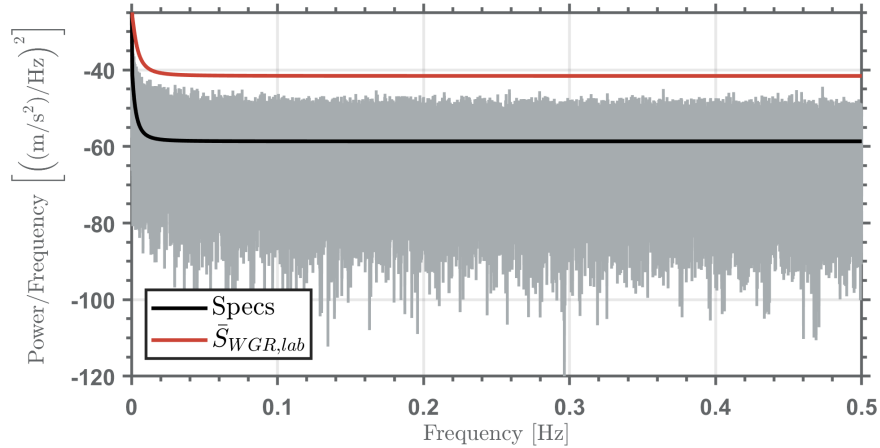


Figure 6.5. Experimental results: upper-bounding sample accelerometer error PSDs.

Each term in this equation can be found in Table 6.1. The velocity random walk ν_s is modeled as white noise with PSD S_{WN} (defined by the parameter N_0), the acceleration random walk p is modeled as a random walk with PSD S_{RW} (defined by the parameter K), and the time-varying bias b is modeled as a FOGMRP with PSD S_G (defined by the parameters σ_G and τ_G). All of these parameters are also in Table 6.1. The bias b is actually flicker noise, but as already noted, we want to bound its error contribution using a FOGMRP because flicker noise cannot be modeled in the state space domain.

In Figure 6.5, the black curve represents the IMU specifications as provided by the manufacturer. It does not upper-bound the sample PSDs. Instead, we can derive a PSD-based error model by selecting a set of values for Table 6.1's parameters K, σ_G, τ_G and N_0 such that $\bar{S}_{WGR,lab}(f)$, the red curve of Figure 6.5, tightly upper-bounds the sample PSD curves over the frequency range in our datasets. The upper bounding values are given in the fourth column of Table 6.2.

This model, although bounding, is likely to be overly-conservative due to the poor quality of the sample PSD estimates. The following paragraphs present a second methodology, based on AV curves.

6.2.2.2 Modeling through Allan Variance bounding. In this section, we apply the methodology in Figure 6.3 to accelerometer errors for an example IMU (STIM-300 [60]).

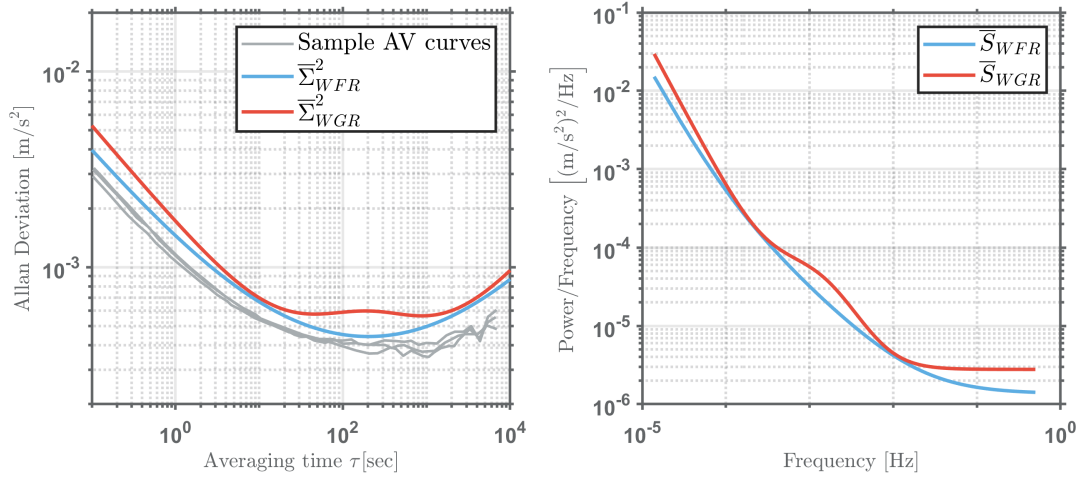


Figure 6.6. AV and PSD domain bounding of IMU errors.

The left plot in Figure 6.6 shows three IMU sample error AV curves Σ_{WFR}^2 (in grey) for the IMU’s x-axis, y-axis, and z-axis as provided by the STIM-300’s manufacturer. The AV domain bound $\bar{\Sigma}_{WFR}^2$ is represented in blue. The “KF-friendly” bound $\bar{\Sigma}_{WGR}^2$ is shown in red. Their respective blue and red PSD curves that ensure Equations 6.12 and 6.14 are satisfied are represented in the right plot of Figure 6.6. The AV and PSD upper-bounding model parameter values are given in the last column of Table 6.2.

The two bounds in Table 6.2 are both high-integrity IMU error models, but they are impacted by the quality of the datasets which they are based upon. The PSD bounding results $\bar{S}_{WGR,lab}$ were obtained using our own experimental lab data collected in *unverified* static conditions. Vibrations and temperature variations were not fully controlled due to our limited lab equipment. In contrast, the bounding results $\bar{\Sigma}_{WGR}^2$ were derived from datasets given in the IMU manufacturer specifica-

Table 6.2. Accelerometer errors bounding model values

Error type	Param.	Units	Bounds	
			$\bar{S}_{WGR,lab}$ (lab data)	$\bar{S}_{WGR}, \bar{\Sigma}_{WGR}^2$ (manuf. specs)
White noise	N_0	m/s/ \sqrt{h}	6.9×10^{-5}	2.77×10^{-6}
FOGMRP	σ_G	m/s ²	3.4×10^{-3}	5.8×10^{-4}
	τ_G	sec	110	100
R.W.	K	m/s/h ^{3/2}	5.5×10^{-5}	1.5×10^{-5}

tion documents. These datasets were obtained in a highly controlled environment. The last two columns of Table 6.2 show that model parameters have much larger values for $\bar{S}_{WGR,lab}$ than for \bar{S}_{WGR} . This is most likely because the experimental data collected in our laboratory is significantly impacted by vibrations and temperature whereas manufacturer specs are not. The new high-integrity spec-based error modeling method not only avoids having to collect own-generated data, but it also provides a tighter error bound.

In addition, it is important to note there are an infinite number of choices of parameter values $\bar{K}, \bar{\sigma}_G, \bar{\tau}_G$ and \bar{N}_0 and value combinations that could have been selected to achieve PSD or AV upper bounds. Depending on the application of interest, a user can decide to apply this methodology and choose a bound which minimizes one parameter over another one.

6.2.3 Gyroscope errors. A similar approach can be applied to the gyroscope errors of the STIM-300 IMU, starting with the PSD bounding method of Chapter 2, Section 2.2.3.2.

6.2.3.1 Modeling through PSD bounding. The gyroscope errors collected in

the five STIM-300 data sets introduced earlier are converted to the frequency domain using the periodogram function. These curves are represented in grey in Figure 6.7. The information provided in the STIM-300 specification document allows us to derive its associated curve (black curve in Figure 6.7). Similar to the case of accelerometer error, the black curve does not over bound the errors, but it instead appears to simply be a good approximation of them. To derive a high integrity error model, we must upper bound the sample PSD curves (in grey), and obtain the red curve.

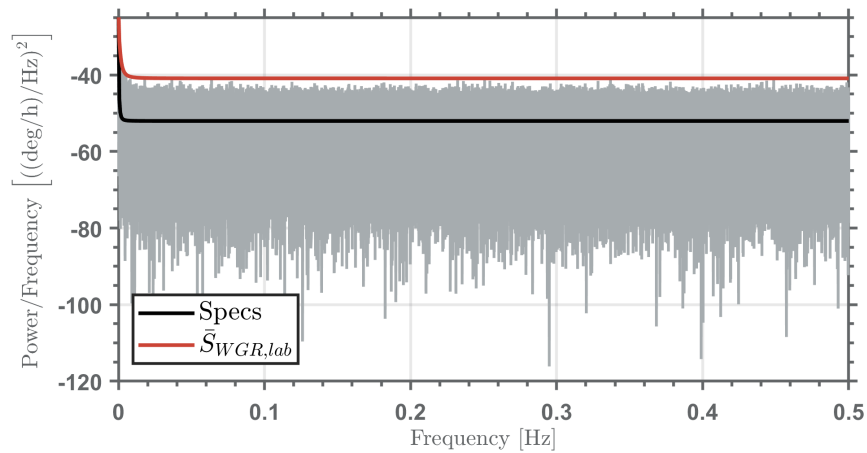


Figure 6.7. Experimental results: upper-bounding sample accelerometer error PSDs.

The error model values used to obtain the red curve are described in Table 6.3, in the $\bar{S}_{WGR,lab}$ column. These values are quite large, and the resulting model is likely to be overly conservative due to the noisy nature of the sample PSD estimate. The following subsection derives a high integrity model for the gyroscope errors using the manufacturer's AV curves.

6.2.3.2 Modeling through Allan Variance bounding. Sample AV curve for gyroscopes errors are extracted from the STIM-300 specification document (represented in grey on the left plot of Figure 6.8). They are upper bounded in the AV domain using a sum of WN, flicker noise, and RW: $\bar{\Sigma}_{WFR}^2$. We have shown above that these error sources have a one-to-one mapping between the AV and the PSD

domain, therefore, since $\bar{\Sigma}_{WFR}^2$ upper bounds the sample AV curves, \bar{S}_{WFR} will upper bound their associated PSD curves. Finally, values for the WN, FOGMRP and RW parameters are selected so as to overbound both $\bar{\Sigma}_{WFR}^2$ and \bar{S}_{WFR} (i.e. the criteria defined by Equations 6.12 and 6.14 are met). This bounding model is represented by the red curves in Figure 6.8 and in the last row of Table 6.3.

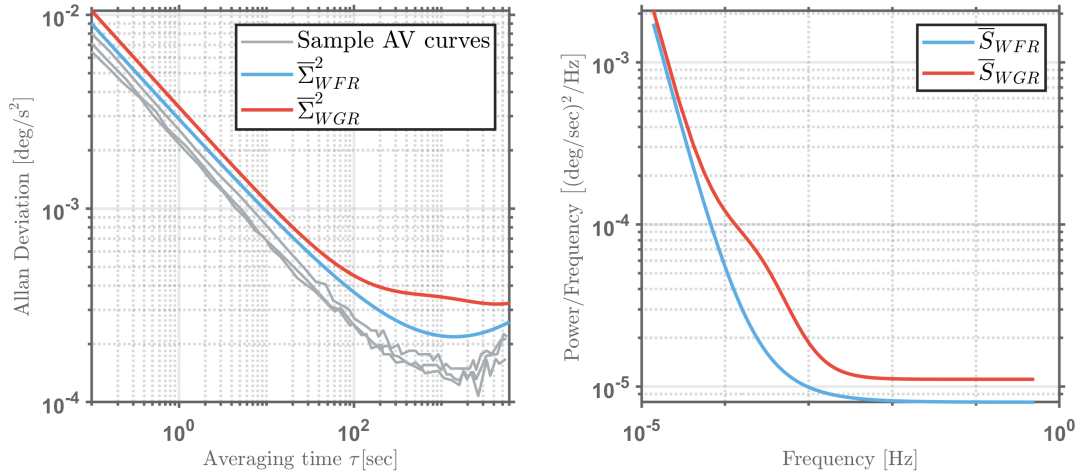


Figure 6.8. AV and PSD domain bounding of IMU errors.

Similar conclusions to the case of accelerometer errors can be drawn: even though both methods provide high integrity error models for the gyroscope errors, the model obtained through the PSD bounding of experimental data is much more conservative than the one obtained through AV (and PSD) bounding of the manufacturer's curves. A user having access to AV curves from the manufacturer should therefore prioritise the second methodology.

6.3 Opening remarks

In the remainder of this dissertation, we focus on a KF that relies solely on GNSS measurements. Inertial measurements are often used in combination with GNSS to improve the continuity of a system (for example in urban canyons). Therefore, even though the error models developed here are not used in the following,

Table 6.3. Gyroscope errors bounding model values

Error type	Param.	Units	Bounds	
			$\bar{S}_{WGR,lab}$ (lab data)	$\bar{S}_{WGR}, \bar{\Sigma}_{WGR}^2$ (manuf. specs)
White noise	N_0	deg/ \sqrt{h}	0.54	0.17
FOGMRP	σ_G	deg/h	5.85	1.01
	τ_G	sec	225	1500
R.W.	K	deg/h ^{3/2}	1.18	0.84

the methodology introduced is applicable to other potential navigation applications requiring high integrity.

CHAPTER 7

PERFORMANCE ASSESSMENT OF FAULT FREE RECURSIVE ARAIM

In Chapter 1, the limitations of snapshot ARAIM were brought to light. In [7], the authors showed that those limitations could be alleviated by exploiting satellite motion in ARAIM. One way to do so is by developing what we will call *recursive ARAIM* or *KF ARAIM*: a KF implementation of ARAIM, where measurements are filtered and integrated over time, as opposed to the traditional *snapshot ARAIM* where measurements are used at individual times to estimate a position solution.

The Kalman filter derived in this chapter relies on two types of measurements: iono-free code and carrier measurements. As the signal travels between the satellite and the user, it is impacted by satellite orbit and clock errors, tropospheric delay, multipath and thermal noise:

$$\begin{aligned}\rho_k^i &= r_k^i + c (\delta t_{r,k} - \delta t_k^i) + T_k + \varepsilon_{MP,\rho,k} + \varepsilon_{TN,\rho,k} + b_{GD,\rho}^i \\ &= r_k^i + c (\delta t_{r,k} - \delta t_k^i) + T_{GPT2w,k} + m_W(\theta_k^i) \epsilon_{T,k}^i + m_\rho(\theta_k^i) (\epsilon_{MP,\rho,k} + \epsilon_{TN,\rho,k}) + b_{GD,\rho}^i.\end{aligned}\tag{7.1}$$

$$\begin{aligned}\phi_k^i &= r_k^i + c (\delta t_{r,k} - \delta t_k^i) + T_k + \varepsilon_{MP,\phi,k} + \varepsilon_{TN,\phi,k} + \eta_{IF}^i + b_{GD,\phi}^i \\ &= r_k^i + c (\delta t_{r,k} - \delta t_k^i) + T_{GPT2w,k} + m_W(\theta_k^i) \epsilon_{T,k}^i + m_\phi(\theta_k^i) (\epsilon_{MP,\phi,k} + \epsilon_{TN,\phi,k}) \\ &\quad + \eta_{IF}^i + b_{GD,\phi}^i.\end{aligned}\tag{7.2}$$

where:

- r_k^i is the satellite-to-receiver range,
- c is the speed of light,
- δt_k^i and $\delta t_{r,k}$ are the satellite and receiver clock bias,

- m_W is the wet mapping function to the GPT2w tropospheric model (defined in Chapter 4),
- m_ϕ is the (environment specific) carrier multipath and thermal noise mapping function (defined in Chapter 5),
- m_ρ is the (environment specific) code multipath and thermal noise mapping function (defined later in this chapter),
- T_k is the tropospheric delay, and T_{GPT2w} its model,
- $\epsilon_{orb,k}^i$, $\epsilon_{T,k}^i$, and $\epsilon_{MP,\phi,k}$ are the orbit and clock error, the GPT2w tropospheric delay residuals and the carrier phase multipath respectively,
- $\epsilon_{TN,\rho,k}$ and $\epsilon_{TN,\phi,k}$ are the code and carrier thermal noises,
- η_{IF}^i is the satellite-dependent constant floating carrier cycle ambiguity.
- $b_{GD,\rho/\phi}$ is the code/carrier phase group delay impacting the measurements (more details in [38])

In order for the KF output state estimate error variances to be bounding, these errors and their time correlations must be modeled and accounted for properly. In previous chapters, we derived high integrity models for the time correlated errors $\epsilon_{orb,k}^i$, $\epsilon_{T,k}^i$, and $\epsilon_{MP,\phi,k}$. The thermal noise contributions, $\epsilon_{TN,\rho,k}$ and $\epsilon_{TN,\phi,k}$, are white with bounding standard deviations specified in [1]. The following subsection briefly summarizes the error models developed in previous chapters. Additionally, Appendix G describes the snapshot models (specific to our testing environment) that were developed for the code multipath errors. Code phase is only used at satellite acquisition, so it is not necessary to model (or bound) their errors as random processes.

7.1 Summary of GNSS error models

The dynamics of a FOGMRP, with parameters σ_x and τ_x , are expressed in discrete form as:

$$x_{k+1} = e^{-\Delta t/\tau_x} x_k + \sqrt{\sigma_x^2 (1 - e^{-2\Delta t/\tau_x})} \omega_k, \quad (7.3)$$

$$\omega_k \sim N(0, 1) \quad \text{and} \quad x_0 \sim N(0, \sigma_0^2)$$

where σ_0^2 is the steady-state variance of the process.

Since the orbit and clock errors $\epsilon_{orb,k}^i$ (with parameters σ_{orb} and τ_{orb}), the tropospheric delay residuals $\epsilon_{T,k}^i$ (with parameters σ_T and τ_T), and the carrier phase multipath $\epsilon_{MP,\phi,k}$ (with parameters σ_ϕ and τ_ϕ) are all modeled as FOGMRPs, the error states for a carrier phase measurement from any given satellite are modeled by the following dynamic system:

$$\begin{bmatrix} \epsilon_{orb}^i \\ \epsilon_T^i \\ \epsilon_{MP,\phi}^i \end{bmatrix}_{k+1} = \begin{bmatrix} e^{-\Delta t/\tau_{orb}} & 0 & 0 \\ 0 & e^{-\Delta t/\tau_T} & 0 \\ 0 & 0 & e^{-\Delta t/\tau_\phi} \end{bmatrix} \begin{bmatrix} \epsilon_{orb}^i \\ \epsilon_T^i \\ \epsilon_{MP,\phi}^i \end{bmatrix}_k + \begin{bmatrix} \sqrt{\sigma_{orb}^2 (1 - e^{-2\Delta t/\tau_{orb}})} \\ \sqrt{\sigma_T^2 (1 - e^{-2\Delta t/\tau_T})} \\ \sqrt{\sigma_\phi^2 (1 - e^{-2\Delta t/\tau_\phi})} \end{bmatrix} \omega_k \quad (7.4)$$

The FOGMRP parameters of each error term are summarized in Table 7.1.

Additionally, since code measurements will be used at satellite acquisition to aid in the cycle ambiguity estimation, code multipath and group delay must be

Table 7.1. GNSS Error Model Parameter Values

Error Type	Subscript	Clocks	τ [sec]	σ [m]	Chapter
Orbit and Clock	orb	GPS	20880	1.55	3
		GAL	10800	0.7	3
Troposphere	T		72000	0.09	4
Carrier multipath (L1)	ϕ		300	0.012	5
Thermal noise (L1)	TN_ϕ			0.0028	5

account for as well. Appendix G derived an error model of the multipath environment present in the following experimental results. This model will be referred to as σ_ρ . Code measurements are not only impacted by multipath but also group delays whose dynamics are highly sensitive to small scale attitude motions and further complicated by a multiplicity of reflective surfaces on platforms with complex shapes, again like transport aircraft, making multipath far more amenable to stochastic modelling than group delay. Since the two are often hard to separate, the code multipath model σ_ρ derived in Appendix G is believed to also cover a large portion of the group delay's impact. The remaining, un-modeled impact of the group delay $\mathbf{b}_{GD,\rho}$ will be accounted for through the use of an additional model term introduced later in Section 7.2.4.

7.2 Kalman Filter design

The following sections describe the steps employed in the KF design.

7.2.1 System State Selection. To incorporate the FOGMRP models in a KF, we use state augmentation. Considering the following state vector:

$$\mathbf{x}_k = \left[\mathbf{r}_{3 \times 1} \quad \mathbf{b}_{2 \times 1} \quad \boldsymbol{\epsilon}_{MP_{\Phi_n \times 1}} \quad \Delta T_{1 \times 1} \quad \boldsymbol{\eta}_{IF_{n \times 1}} \quad \boldsymbol{\epsilon}_{orb_{n \times 1}} \right]_k^T \quad (7.5)$$

where n is the total number of satellites in view at time k , \mathbf{r} is the 3D East-North-Up (ENU) position estimate of the receiver, \mathbf{b} is the vector of user clock biases for the GPS and Galileo constellations, $\boldsymbol{\epsilon}_{MP,\phi,k}^i$ are the carrier multipath errors, ΔT is the GPT2w zenith tropospheric delay residual, $\boldsymbol{\eta}_{IF}$ is the iono-free carrier phase ambiguity and $\boldsymbol{\epsilon}_{orb}$ are the satellite orbit and clock residual errors. Given $n = n_{GPS} + n_{GAL}$ satellites in view at time k , the state vector \mathbf{x}_k will have a dimension of $m = 3n + 6$.

7.2.2 System Dynamic Model. The system's discrete dynamic model is as follows:

$$\mathbf{x}_{k+1} = \boldsymbol{\Phi}_k \mathbf{x}_k + \boldsymbol{\Gamma}_k w_k \quad (7.6)$$

and

$$\mathbf{V}_k = \begin{bmatrix} \sigma_{TN,\phi,1,k}^2 & & & \\ & \ddots & & \\ & & \ddots & \\ & & & \sigma_{TN,\phi,n,k}^2 \end{bmatrix},$$

where $\mathbf{G}_{k,n \times 3}$ is the geometry matrix containing the unit line of sight vectors of each satellite in view. The measurement errors contained in \mathbf{v}_k are comprised of the thermal noise [41–43]; all the other error terms are being handled by state augmentation.

7.2.4 KF Equations and Initialization. The KF relies on the successive use of two equations: the time update (prediction) and the measurement update.

The time update relies on the user's knowledge of the errors' dynamics. At any epoch k , the state vector and covariance matrices are updated using the following equations:

$$\mathbf{x}_{k|k-1} = \Phi_k \mathbf{x}_{k-1|k-1}, \quad (7.8)$$

$$\mathbf{P}_{k|k-1} = \Phi_k \mathbf{P}_{k-1|k-1} \Phi_k^T + \Gamma_k \mathbf{W}_k \Gamma_k^T. \quad (7.9)$$

The measurement update can be expressed as:

$$\mathbf{x}_{k|k} = \mathbf{x}_{k|k-1} + \mathbf{L}_k (\mathbf{z}_k - \mathbf{H}_k \mathbf{x}_{k|k-1}), \quad (7.10)$$

$$\mathbf{P}_{k|k} = (\mathbf{I}_{n \times n} - \mathbf{L}_k \mathbf{H}_k) \mathbf{P}_{k|k-1}, \quad (7.11)$$

where $\mathbf{L}_k = \mathbf{P}_{k|k-1} \mathbf{H}_k^T (\mathbf{V}_k + \mathbf{H}_k \mathbf{P}_{k|k-1} \mathbf{H}_k^T)^{-1}$ is the Kalman gain.

The state vector estimate is initialized using the following expression:

$$\mathbf{x}_0 = [\mathbf{0}_{1 \times 3} \quad \mathbf{0}_{1 \times 2} \quad \mathbf{0}_{1 \times n} \quad 0 \quad (\delta\phi_k - \delta\rho_k)_{1 \times n} \quad \mathbf{0}_{1 \times n}]^T, \quad (7.12)$$

where $\delta\rho_k$ and $\delta\phi_k$ are the code and carrier measurements of the new satellites in view, after corrections (GPT2w and satellite clock). The covariance matrix is initialized as:

$$\mathbf{P}_0 = \begin{bmatrix} w_\infty \mathbf{I}_{3 \times 3} & & & & & \\ & w_\infty \mathbf{I}_{2 \times 2} & & & & \\ & & \sigma_\phi^2 \mathbf{I}_{n \times n} & & & \\ & & & \sigma_{trop}^2 & & \\ & & & & (\sigma_{\Delta GD}^2 + \sigma_\rho^2) \mathbf{I}_{n \times n} & \\ & & & & & \sigma_{orb}^2 \mathbf{I}_{n \times n} \end{bmatrix}, \quad (7.13)$$

where $\sigma_{\Delta_{GD}}^2$ can be interpreted as an inflation factor that accounts for the unknown/unmodeled impact of the group delays $\mathbf{b}_{GD,\rho}$ on the code measurements ρ and its effect on the initial estimate of the ambiguity. Note that position and clock states are given very high initial covariance values (w_∞) because we do not assume prior knowledge on these states, cycle ambiguity state variances are initialized based on the code measurement error (since it is much larger than carrier phase error contribution), and the other states are initialized based on their steady states values.

7.3 Performance assessment

In this section, we assess four key elements of this research:

- The value of a KF approach for GNSS positioning over the more traditional snapshot Least Square Estimator (LSE) method. Assuming that both methods use the same error models, what are the performance benefits of a KF over a LSE approach?
- The sensitivity of KF performance to variations in the error models derived in Chapters 3 through 5.
- The advantage of tightening the orbit and clock error bounds by separating their models based the satellites' clocks.
- The overall performance of the KF design over 24h satellite geometry variations.

To address these four points, we collected and processed data described in the following subsection.

7.3.1 Experimental set up. On September 5th 2022, 24 hours of data were collected at a 1 sec sampling rate using a OEM6 NovAtel receiver and pinwheel NovAtel antenna, located on the rooftop of the Rettaliata Engineering building (Illinois Insti-

tute of Technology campus). The environment of the antenna is shown in Chapter 5, Figure 5.1, where the red star represents the antenna location.

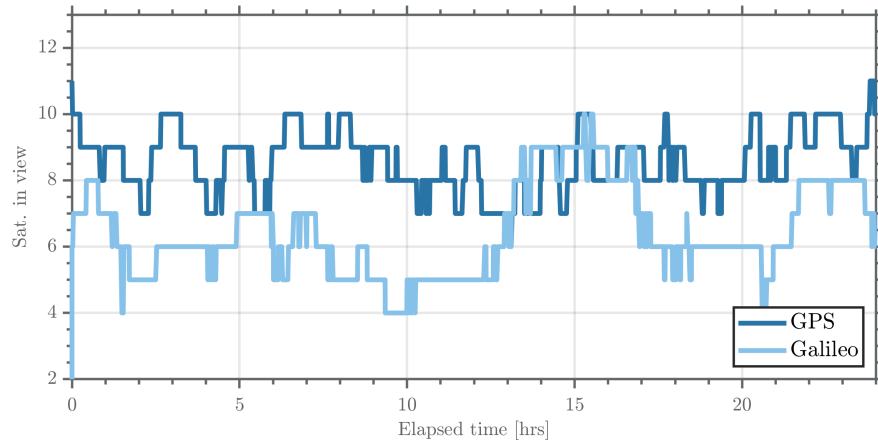


Figure 7.1. GPS and Galileo satellites in view

These 24h are divided into 4h segments: 80 data sets, shifted by 15 min from one another. The first 4h segment is used in subsections 7.3.2 through 7.3.6. The other segments are used for validation in subsection 7.3.6.

Because the orbit and clock error models derived in [23, 61] are restricted to the GPS and Galileo constellations, only those two constellations were processed in this chapter. The number of visible GPS and Galileo satellites during the experiment is shown in Figure 7.1.

7.3.2 Advantage of KF over LSE with the same error models. In this first test case, we evaluate the performance improvement of a KF incorporating time correlated error models over the LSE approach. The error models standard deviations, coefficients and mapping functions already described are applied to both the LSE and KF approaches. Since LSE is a snapshot approach, the time constants in Table 7.1 are not involved in the LSE estimation process. Also, the typical LSE implementation uses carrier-smoothed-code measurements, whereas the KF only uses code during the

first epoch of a satellite in view. The multipath models associated to our testing environment used for carrier-smoothed-code and code are described in Appendix G. For a fair covariance comparison between the LSE and the KF performance, we assume $\sigma_{\Delta_{GD}} = 0$ in Equation 7.13 (a different value of alpha will be used in Section 7.3.6).

In this subsection, the performance of the KF algorithm (and its error models) will be assessed by looking at its PLs, and in particular, the vertical component (considering aircraft precision approach as a motivating application). For an example maximum allowable integrity risk requirement value of 10^{-8} , the fault free VPL can be obtained as:

$$\text{VPL} = 5.73 \times \sigma_D, \quad (7.14)$$

where σ_D is the position error standard deviation in the ‘down’ direction computed by the KF.

Figure 7.2 shows the VPLs obtained over a 4-hour window for both the LSE (green curve) and the KF (blue curve) systems. The Kalman filter (KF) relies on raw code measurements to initialize the carrier cycle ambiguities. However, raw code measurements tend to have a larger variance than the carrier smoothed code used in the least squares estimator (LSE). As a result, the KF starts off with a slightly larger covariance during the first few minutes. In general, the KF provides a covariance envelope that is smaller and smoother than that of the LSE, with an asymptotic value of around 5 meters. It is worth noting that the KF is less affected by satellites coming in and out of view compared to the LSE. For example, at times such as $t = 1.5$ h and $t = 2.8$ h, where there are significant variations of several meters in the LSE, the KF remains relatively stable. It is also evident that the snapshot/LSE algorithm only sporadically meets the 10-meter AL for precision approach, while the KF ensures that the VPL remains less than or equal to the AL for most of the 4-hour

run duration. By reducing the position errors, it is possible to improve the continuity of the navigation solution for applications with strict requirements, such as precision approach.

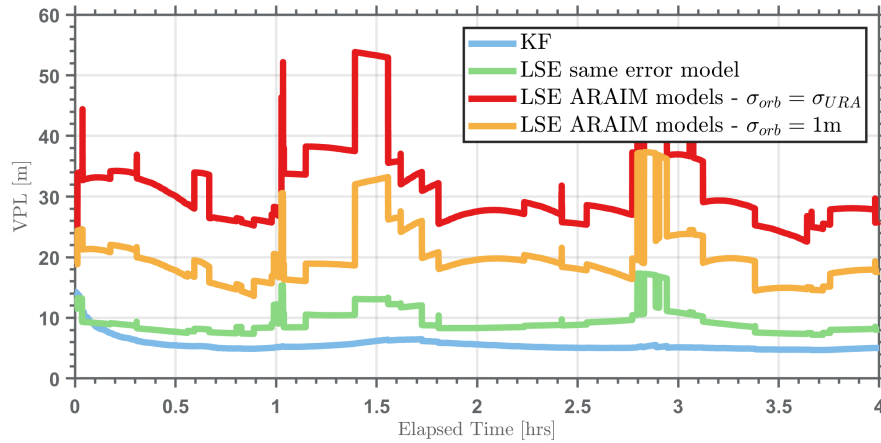


Figure 7.2. KF and LSE/snapshot vertical protection levels

7.3.3 Advantages of KF with Time-Correlated Bounding Models over Fault-Free LSE ARAIM. In this subsection, we compare the results obtained from three estimation processes:

- KF with time correlated, bounding error models (as described in Section 7.2): blue curve.
- LSE with the ARAIM error models (as described in [41–43]) and Appendix G: red curve
- LSE with the ARAIM error models, but $\sigma_{orb} = 1\text{ m}$: orange curve.

These scenarios enable us to analyze the impact of orbital error models on the current ARAIM algorithm and observe the performance improvements (in terms of VPLs) for an ARAIM user when switching from LSE to KF.

Let us first compare the performance of the KF using the error models presented in Chapters 3, 4 and 5) with the LSE using the error models used in FF ARAIM ([41–43]). Figure 7.2 shows the Kalman Filter (KF) results in light blue and the Least Squares Estimation (LSE) results in red. The LSE VPLs average around 30 meters and vary significantly as satellites come in and out of view and as line of site geometries change. Variations can reach tens of meters, such as at $t = 1.5$ h. These geometry variations prevent the LSE VPLs from meeting the LPV-200 AL requirements of 35 meters during those times. Therefore, the LSE ARAIM algorithm cannot provide continuity under LPV-200 requirements, while the KF can with significant margin.

The major difference in these two implementations is in the orbit and clock error models. For example for GPS, we used our new orbit/clock error model in the KF, which has a bounding standard deviation of 1.55 m. However, for the LSE we assumed that estimator uses the GPS broadcast User Ranging Accuracy (URA), whose value today is, at best, 2.4 m. To verify whether the orbit and clock errors are an important contributor to the observed performance differences, a third case was studied using the same ARAIM LSE approach but with $\sigma_{orb} = 1$ m (which is often used in ARAIM availability studies in anticipation of possible future reductions in the GPS broadcast URAs). These results are represented by the orange curve in Figure 7.2. We can see that the VPLs have dropped from the previously observed values, clearly showing that σ_{orb} does have an important impact on the LSE VPLs observed here.

7.3.4 Sensitivity Analysis. In this section, we analyze the sensitivity of the KF to the values of the FOGMRP parameters (σ_x and τ_x) for each GNSS error. Each of the FOGMRP parameters described in Table 7.1 are modified one by one by 20% of their initial value. To investigate the degradation of the KF’s vertical position

standard deviation, we increase the standard deviations of the FOGMRP errors and decrease the time constants by 20%. The resulting VPL is denoted as $VPL_{\Delta 20\%}$. We then compare these results individually to the "nominal KF" results (denoted as VPL_{nom}) presented in previous sections. The performance improvement metric used in this subsection is the following ratio:

$$q(t) = \frac{VPL_{\Delta 20\%}(t)}{VPL_{nom}(t)}. \quad (7.15)$$

In Figure 7.3, the curves with square markers represents the evolution of the ratio q in Equation 7.15 when the FOGMRP parameters of the orbit and clock model are modified. The curves with triangle and circle markers are for tropospheric and multipath models, respectively. Values above 1 correspond to results for which the 20% modification resulted in larger VPLs.

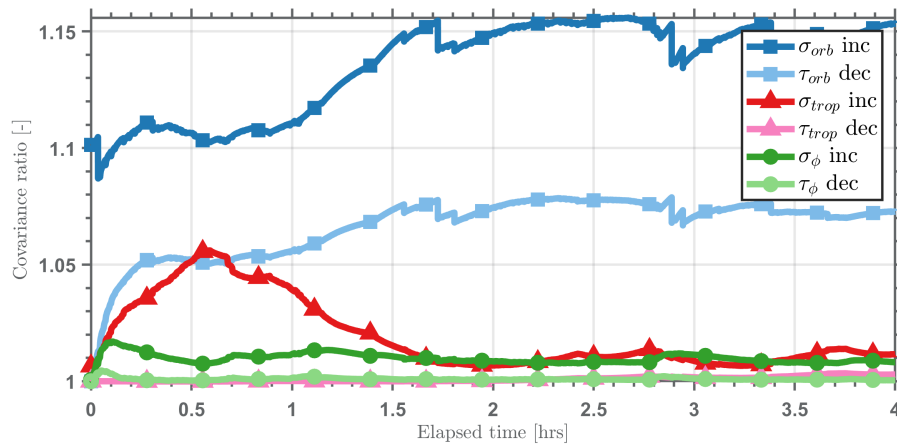


Figure 7.3. Sensitivity to the FOGMRP parameters

The orbit/clock error model is the most sensitive of the three error types. Increasing σ_{orb} by 20% leads to a 10% increase in the KF's VPL at $t = 0$ h. The impact gradually increases as the KF converges (i.e., for $t > 30$ min), with an asymptotic ratio of approximately 1.15 (which represents a 15% increase in the KF's VPL). Among all the curves shown in this figure, this one has the highest ratio after convergence.

The second largest impact is observed when the time constant of the orbit/clock error model is decreased (light blue squared curve for τ_{orb}) with a 7% increase of the KF VPLs at $t = 4$ h.

Another important impact is observed with the tropospheric model, in particular with respect to its standard deviation. Additional analysis revealed that the transient behavior observed at $t = 0.5$ h is geometry dependent and largely due to low elevation satellites coming in and out of view. This satellite geometry effect on the KF output variance becomes negligible once the vertical tropospheric delay state has become observable: similar geometry variations are present at $t = 2.7$ h and $t = 3.7$ h, but these have no impact on q . We also note that the 20% decrease of τ_T has no impact on the KF VPL; the ratio q remains equal to 1 throughout the 4 h window. This is because a modification of the time constant from 20 to 16 hours will not be noticeable over a 4 hour KF run time.

The least impactful error model is for carrier phase multipath, shown in green. Modifying the time constant proves to have a negligible impact on the KF VPL, and modifying its standard deviation results in a small 1% increase in the KF VPL.

Overall, the results in this section show that a user interested in minimizing the KF output position error variance should focus on tightening the bounds of the orbit and clock error models.

7.3.5 Advantages of separate, clock based, orbit and clock error models.

The previous section highlighted the importance of tightening the orbit and clock error model over all other errors. In Chapter 3, we derived tightly bounding error models for the orbit and clock errors based on the satellite's clock types: two separate bounds for GPS's Rb and Cs satellite clocks, and two other bounds for Galileo's RAFS and PHM clocks. In the last section, we used a common error model for all GPS satellites

and another model common to all Galileo satellites (cf, Table 7.1). In this section, we analyse the KF performance improvement of when tailored models are used for the different satellite clock types.

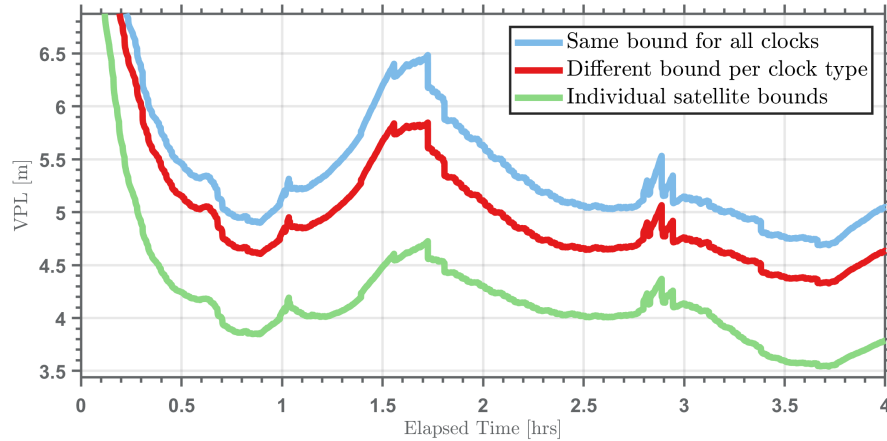


Figure 7.4. Impact of clock-specific orbit and clock error model on KF output standard deviation

The results in Figure 7.4 shows the VPLs obtained over a example 4-hour run. The blue curve represents the scenario in which the same FOGMRP model (with $\sigma_{orb} = 1.55$ m and $\tau_{orb} = 5.8$ h) is used for GPS Rb and Cs satellites and the same model (with $\sigma_{orb} = 0.7$ m and $\tau_{orb} = 3$ h) is used for the Galileo RAFS and PHM satellites. The red curve represents the scenario in which orbit and clock errors are modeled according to the satellite's clock type: GPS models are separated into a Rb-specific model ($\sigma_{orb} = 1.35$ m and $\tau_{orb} = 6.4$ h) and a Cs-specific model ($\sigma_{orb} = 1.55$ m and $\tau_{orb} = 5.8$ h), and Galileo models are separated in a RAFS-specific model ($\sigma_{orb} = 0.65$ m and $\tau_{orb} = 3$ h) and a PHM-specific model ($\sigma_{orb} = 0.7$ m and $\tau_{orb} = 3$ h). By employing clock-specific models, we allow for tighter bounds on the Rb and RAFS satellites. The tightening of those bounds results in smaller VPLs.

Figure 7.5 shows the standard deviations of the stationary GPS orbit/clock error datasets used in this work. The x-axis represents the PRN numbers. The coloring matches the clock coloring of the PSD figures shown in Chapter 3. In Chapter

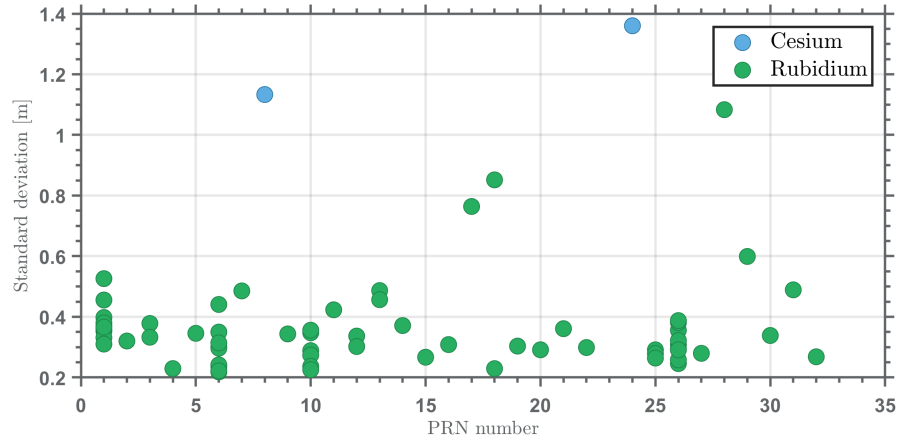


Figure 7.5. Standard deviations of stationary GPS datasets (2018-2020)

3, we derived bounding models for Rb and Cs satellites with standard deviations of 1.35 m and 1.55 m respectively. Figure 7.5 shows that these standard deviations do upper bound the observed sample standard deviations. Looking more closely at the Rb results, one can notice that the bound is driven by PRN 28. In Appendix I, we gathered satellite block information for each GPS satellite during the period of data that was used in the modeling of orbit and clock errors (2018-2020). In that appendix, we show that the satellite using PRN 28 dates back from 2000. The large error standard deviation can therefore be explained by the age of the satellite.

Newer Rb satellites (with smaller standard deviations in Figure 7.5) are so far not taken advantage of in the modeling; they are modeled with the same *loose* model as older satellites (e.g., PRN 28). To tighten the orbit and clock error models and take advantage of recent orbit and clock error improvements, we consider another option: bounding each satellite individually. The KF output VPLs for this scenario are represented by the green curve of Figure 7.4. The performance improvement from tightening the model is noticeable: at $t = 4$ h, the KF output VPL drops from 5 m (for the scenario using one bounding model for all satellites in each constellation – blue curve) to 3.75 m (for the scenario using individual bounds for each satellite –

green curve).

By reducing the PLs, we produce a system capable of meeting more stringent AL requirements. However, such individual bounding of orbit and clock errors may not be practical in terms of implementation. In the following chapter, we will further discuss possible approaches to tightening the bounds, as well as the limitations of such approaches.

The previous sections analysed various aspects of the KF-computed vertical position error standard deviations: how much lower they were compared to LSE's and how sensitive they were to their error models. These standard deviations must now be validated with data. The following section will do so over multiple data sets.

7.3.6 Overall performance of KF with time correlated bounding models.

To verify KF performance we divide 24 hours of data into 80 4-hour sets, shifted by 15 min intervals. Each data set is processed by the KF described in Section 7.2. Figure 7.6 shows the temporal evolution of the vertical position estimate ϵ_D normalized by its associated standard deviation computed by the KF σ_D . Each data set is represented in grey, and the red area highlighted in the figure represents the area for which the normalized error is smaller than 1. The variance of the combined raw code phase multipath and thermal noise error was inflated by a factor $\sigma_{\Delta_{GD}} = 2\sigma_\rho$ in Equation 7.13 to ensure that antenna group delay did not adversely affect carrier cycle ambiguity initialization. This is the reason the grey curves initially exceed 1.

In total, 98.2% of the error data is within the highlighted bounds, significantly more than the normal 1- σ expectation of 67%). This confirms (as already suggested) that the bounding errors models developed in this dissertation can be tightened further. Several approaches can be considered to tighten the models:

- Use clock-specific error models (as suggested by the results of Section 7.3.5).

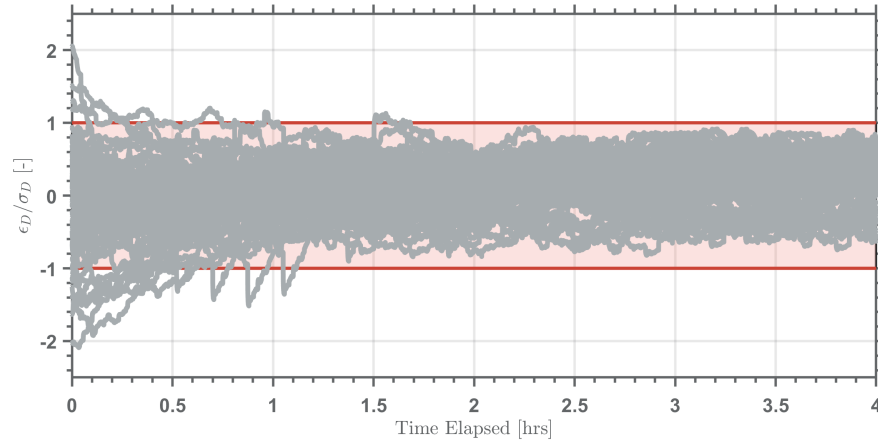


Figure 7.6. Covariance validation results over 6 sets of 4h

- Consider different model processes rather than FOGMRP (e.g. second order Gauss Markov processes) to obtain bounds that are closer to the true processes’.
- Leverage newer ephemeris models being broadcast instead of the current L/NAV broadcast ephemeris models (the ones modeled in Chapter 3).

Each of these solutions will come with their own set of difficulties. The first option will require the user to know in real time which clock a given satellite is relying on. The second solution will require a slightly different implementation from the ones introduced in this chapter and potentially a state augmentation that involves more variables (therefore increasing computational complexity). The third solution suggests that the user leverages recently developed C/NAV ephemeris models, which contain more parameters than the current L/NAV message and therefore produce much smaller orbit and clock errors than L/NAV. This solution requires that future ARAIM users rely only on C/NAV messages over the current L/NAV messages.

CHAPTER 8

CONCLUSION AND FUTURE WORK

Integrity concerns are at the center of safety critical applications and have pushed the GNSS community to develop integrity-focused algorithm such as ARAIM. Considerable efforts have been made to achieve the stringent requirements of vertical guidance (LPV-200). But under depleted constellation conditions, LPV-200 was can only sparsely be achieved [7]. To alleviate these limitations, this dissertation introduced and developed an alternative approach to ARAIM: recursive ARAIM.

8.1 Summary of accomplishments

The focus of this thesis has been on the development of a methodology for high integrity, time correlated error modeling. Power spectral density bounding has been at the center of this thesis and was adapted to the more common but also more challenging cases of non-stationary errors. More details on these various areas of contributions are discussed in the following subsections.

8.1.1 Developing a methodology for high integrity, time correlated error modeling. The core concept of PSD bounding was first brought to light by Langel et al. [11] but was restricted to stationary data. In practice, the discrete and finite nature of most data sets makes it almost impossible to guarantee its stationarity. Therefore, this dissertation developed an error classification, based on the “type” of stationarity observed in the data, as well as its PSD’s characteristics (time dependency). The PSD bounding method was then adapted for each error category.

8.1.2 Developing high integrity, time correlated GNSS and INS error models.

8.1.2.1 Orbit and clock errors. The orbit and clock errors of GPS and Galileo satellites were developed (over 2018-2020) and their characteristics were analyzed. In particular, the clear difference of the Rubidium clock satellites versus the Cesium ones was brought to light. These differences led to the development of clock-specific error models for the two constellations: a Rubidium model and a Cesium model for GPS, and a RAFS model and a PHM model for Galileo.

8.1.2.2 Tropospheric delay. The residuals of two separate models were analyzed in this thesis (the MOPS model and the GPT2w model) at 100 stations worldwide with data from 2018. Both models showed their limitations during tropospheric storms but, unlike the MOPS model, the GPT2w proved capable of properly modeling yearly variations of the tropospheric delay (such as the monsoon season in India). The GPT2w model also performed better worldwide and showed centimeter to millimeter level yearly biases in their residuals. The MOPS model, however showed that certain parts of the world were impacted by yearly biases that could reach up to 12 cm. Both models' residuals were converted to the frequency domain and upper bounded. However, to simplify the KF implementation of this thesis and not have to model a bias separately, this section concluded with the recommendation of using the GPT2w model for better performance.

8.1.2.3 Carrier phase multipath. Carrier phase multipath was characterized using the difference of two frequency carrier phase measurements. The remaining term was impacted by ionospheric delay that needed to be extracted as well. Because the frequency characteristics of multipath and ionospheric delay are so different from one another, the ionospheric component was removed using high pass filtering. An in depth analysis of the cut of frequency chosen for filtering was performed as well, so as to ensure that the final residuals would only contain carrier phase multipath. The PSD bounding methodology was then applied to the carrier phase multipath

measurements of our testing environment, and resulted in a model comprised of a FOGMRP and a WN.

8.1.2.4 Inertial errors. For *unstable* errors such as inertial errors (i.e. their flicker noise), the ACF and PSD vary with time, making it impossible to apply the FT methodology used for other errors. Instead, the PSD bounding approach was modified to use the periodogram function.

8.1.3 Leveraging AV data to provide high integrity, time correlated inertial error models. The low quality of the periodogram estimate often results in an overly conservative model. A second approach was introduced which leveraged the high quality AV curves often provided by inertial manufacturers and revolved around the concept of Allan Variance bounding. Our work revealed the inability to produce high integrity error models using AV curves alone. This information had never been brought to light in the past. To ensure the integrity of a model derived through AV bounding, additional criterion on the final error model were introduced.

8.1.4 Implementing recursive ARAIM with high integrity, time correlated error models.

8.1.4.1 Highlighting the advantages of KF over LSE. The output of the KF was compared to that of the LSE approach. The KF output standard deviation was shown to be much smaller (by a factor of 5) and much less impacted by satellite coming in and out of view than the LSE output. This observation reinforced the argument for this dissertation: recursive ARAIM could help lower achieve more stringent requirements by lowering the protection levels of the system.

8.1.4.2 Analysing the sensitivity of recursive ARAIM to its error models. A sensitivity analysis revealed that variations in the orbit and clock error model impacted the KF output the most. Therefore, to lower the KF output, one must

ensure its orbit and clock error model is as tight as possible.

8.1.4.3 Investigating the performance improvement of clock-specific orbit and clock error models. Based on the conclusions of the previous subsection, an analysis was performed in which several KF were run with various orbit and clock error models (for the loosest to the tightest):

- (a) Each constellation (GPS and Galileo) uses their own model,
- (b) Each constellation separate their models into two, clock specific models: Rb/Cs for GPS and RAFS/PHM for Galileo,
- (c) Each satellite has its own error model.

This analysis revealed important performance improvement from tightening orbit and clock models. Tightening the models from (a) to (b) resulted in a KF output VPL drop from 5 m to 3.75 m (after convergence). But individual satellite clock bounding is not as straight forward as option (a) and (b) would be. Implementing this in ARAIM would require core changes to the ARAIM algorithm such as a modified dissemination strategy (ISM would need to be much larger — Integrity Support Data? — to account for each satellite's model). Additionally, the dilemma of integrity versus age of data arises: to bound satellites individually, several years of data would need to be gathered so as to ensure (1) the accuracy of our PSD estimate (as currently done in this work), and (2) a good historical representation of what this satellite's errors have looked like. Recent upgrade to the GPS constellation have led to a decrease in the GPS orbit and clock errors. Modeling those errors with recent satellites would result in lower/tighter orbit and clock satellite bounds, but would also result in much shorter data length. This dilemma will need to be taken into consideration in future work.

8.2 Recommended topics for future research

A number of recommendations for future work are given in the following subsections to enhance the performance of recursive ARAIM, and bring it to more realistic scenarios.

8.2.1 Development of tighter orbit and clock error bounds using C/NAV broadcast ephemeris. The modeling done in this work regarding orbit and clock error has proposed several approaches to reduce the orbit and clock error model of current L/NAV broadcast ephemeris errors. The bounds obtained here are believed to be close to the lowest possible whether when modeled per constellation, or per clock and constellation. For applications with more stringent requirements, one may consider modeling the orbit and clock errors to the C/NAV model. The C/NAV model is a more recent orbit and clock error model which contains more ephemeris parameters than the current L/NAV model and therefore shows promising results. Modeling its errors could result in much lower error bounds, at the expense of much less historical data.

8.2.2 Recursive ARAIM under faulted assumption. The first step in demonstrating the need for recursive ARAIM was to assess its performance in fault free conditions. This dissertation did that. Future work would now benefit from investigating the performance of recursive ARAIM under (more realistic) faulted conditions so as to address other performance metrics: continuity and availability.

8.2.3 Inertial-aided recursive ARAIM for continuity. Finally, in this dissertation, we introduced a methodology to model inertial errors. Applications with restricted geometry (such as driver-less vehicle navigation through urban canyon) would highly benefit from inertial measurements. Inertial-aided recursive ARAIM for autonomous vehicle navigation could greatly improve the continuity of the navigation

system while maintaining ultra tight integrity requirements.

APPENDIX A
EPHEMERIS INTERPOLATION

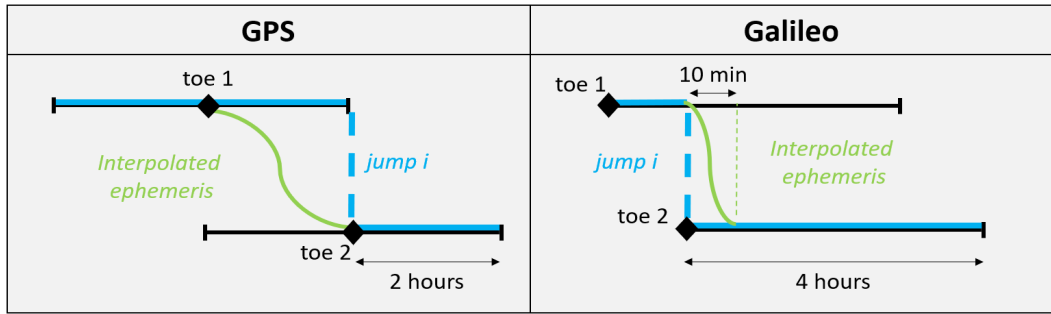


Figure A.1. GPS and Galileo Ephemerides Interpolation Diagram

GPS satellites typically broadcast a new set of ephemerides every 2 hours. Each set is valid for at least 4 hours. Hence, when a new set of ephemerides is received, the previous one is still valid for another 2 hours. Section 2.3 shows that ephemeris updates introduce jumps in the orbit and clock errors.

If we were to account for the jumps in a batch or KF implementation, we would need to model their dynamic behavior, which would require a cumbersome hybrid continuous/discrete process model. Since smoother dynamics are more convenient to model, and since we would ideally, for ease of implementation, like to model errors using simple models (e.g., as FOGMRP), we instead use interpolated broadcast ephemerides.

A.1 GPS ephemeris interpolation

GPS ephemerides are valid for (at least) 4 hours - 2 hours before and after the specified ‘time of ephemeris’ (*toe*). A new set of ephemerides is normally received by the receiver every 2 hours. When the new set is received, the current one is still valid for some time (2 hours after *toe* [28]). Users who are not concerned with stochastically modeling ephemeris error would typically decide to use the new one immediately. However, our goal is to produce such a model, so we instead interpolate the current (X_{cur}) and next (X_{next}) sets of ephemerides in the position and velocity domains over

a window W_{int} of 2 hours. This interpolation is represented in Figure A.1, where the blue curves are the original, non interpolated ephemerides and the green curve represents the interpolated portion, during the time where both ephemerides are valid. The equation describing this interpolation is:

$$\hat{X}(t - \tau) = \frac{\tau}{W_{int}} X_{next}(t - \tau) + \frac{W_{int} - \tau}{W_{int}} X_{cur}(t - \tau) \quad (\text{A.1})$$

where:

\hat{X} is the interpolated output

W_{int} is the interpolation window

t is the time of the jump between X_{cur} and X_{next}

τ is a dummy variable within the interpolation window: $\tau \in [0 : W_{int}]$

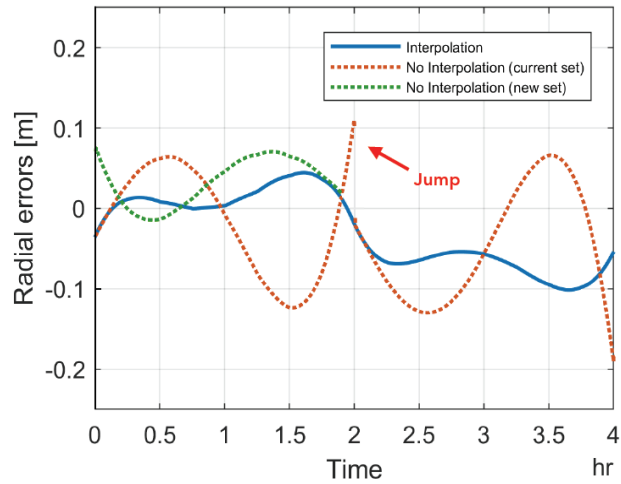


Figure A.2. GPS PRN07 Ephemerides Interpolation

Figure A.2 shows the radial errors of GPS PRN07 in December 2018. The focus is on the "ephemeris jump" occurring at $t = 2$ hours. The blue dashed curve represents the set of ephemeris currently in use and whose toe is $t = 0$ hours. The black dashed curve represents the set of ephemeris that was just received by the user, whose toe is at $t = 2$ hours, but whose validity window starts at $t = 0$ hours. The

green curve represents the result of their interpolation between $t = 0$ and 2 hours. At $t = 0$ hours, the user is currently using the blue set but has just received the black one as well; the interpolation begins at this point. At $t = 1$ hour, both sets are equally weighted to generate the interpolated curve (green). At $t = 2$ hours, the current set time of applicability has expired, and the user is now using 100% of the new set.

A.2 Galileo ephemeris interpolation

Galileo ephemerides are valid for 4 hours after the *toe*, which in this case also represents the time of reception of the new ephemeris. Therefore, the interpolation process is slightly different than for GPS. It is expressed with the following formula:

$$\hat{X}(t + \tau) = \frac{\tau}{W_{int}} X_{next}(t + \tau) + \frac{W_{int} - \tau}{W_{int}} X_{cur}(t + \tau) \quad (\text{A.2})$$

where the interpolation window is now defined (in minutes) as:

$$W_{int} = 180 \times 60 - (toe_2 - toe_1) \quad (\text{A.3})$$

Note that Galileo's interpolation window is different to cope with the fact that the broadcast rate isn't necessarily fixed and can be as short as 10 min. Additionally, unlike GPS, the *toe* is located at the beginning of validity period (see [62] Section C.4.4.1. page 41).

APPENDIX B
VARIANCE OF AUTOCORRELATION ESTIMATES

Let us define the autocorrelation estimate of a random process $X(t)$ as:

$$\hat{R}_X(t) = R_X(t) + \delta R_X(t) \quad (\text{B.1})$$

where $R_X(t)$ is known and $\delta R_X(t)$ is unknown. In the following we derive an approximate expression for the variance of autocorrelation estimate $\hat{R}_X(t)$.

Reference [15] Chapter 8, Section 8.4, Equation (8.103) shows that the variance on the ACF estimate \hat{R}_X can be expressed as:

$$\sigma_{\hat{R}_X(t)}^2 = \frac{1}{T} \int_{-\infty}^{+\infty} R_X^2(\xi) + R_X(\xi + t)R_X(\xi - t)d\xi \quad (\text{B.2})$$

Approximating that the errors are derived from a zero-mean, FOGMP, the parent autocorrelation function can be expressed as:

$$R_X(\xi) \approx \sigma_X^2 e^{-|\xi|/\tau}. \quad (\text{B.3})$$

Substituting Equation B.3 into Equation B.2 and solving the integrals, we obtain:

$$\sigma_{\hat{R}_X(t)}^2 \approx \frac{\sigma_X^4}{T} (\tau + (\tau + 2t)e^{-2t/\tau}). \quad (\text{B.4})$$

APPENDIX C

SENSITIVITY OF PSD ESTIMATION TO PARAMETER SELECTION

The PSD estimation method used in this paper is described in [11] and relies on a tapering window applied to the ACF of the errors prior to the Fourier transform computation. The tapering window, as described in Section 4.2, relies on two parameters: T_1 and T_2 . On top of that, the length of data T plays an important role in the PSD estimation process, since it will drive the ACF accuracy. Hence, when estimating PSDs, we need to take into account all three time parameters: T_1 , T_2 , and T . In this Appendix, we analyze the sensitivity of the PSD estimation process to our choices of T_1 , T_2 , and T .

In Section 3, we showed that the parameter T influences the overall accuracy of the ACF estimate. Since the PSD estimation approach chosen here relies on first estimating error ACFs, the same conclusion applies: the longer the data, the more accurate the ACFs, and hence, the more accurate the PSD estimate will be. Therefore, using as much data as possible would be ideal (i.e., 1 year). Note however, that the choice of T will be entirely determined by the stationarity tests. For this analysis, we assume an ‘average’ value $T = 6$ months.

Additionally, we know that the T_1 parameter represents the lag values until which the ACF will remain unchanged. In our case, because a satellite pass lasts about 7 hours maximum, it is in our best interest to not modify correlation values during that period of time. We therefore choose $T_1 = 7$ hours.

The only parameter left to analyse is T_2 , which will define how rectangular the tapering window will be. If T_1 and T_2 are close to each other, the window will be nearly rectangular, and it will result in spectral leakage in the frequency domain, decreasing the quality of our PSD estimate. Example windows are represented in Figure C.1. The following section analyzes the impact of different T_2 values on the PSD estimate of a FOGMRP process.

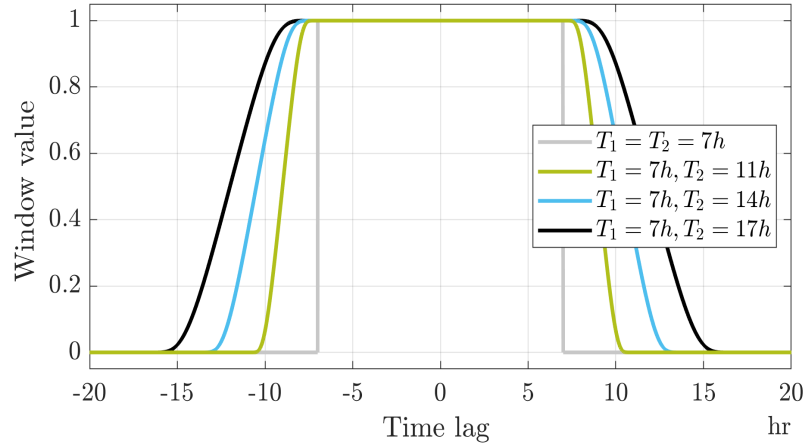


Figure C.1. Example tapering windows used in the PSD estimation process

C.1 Impact of the window shape on a FOGMRP PSD estimate

Let us begin by looking at the impact of various tapering windows on the PSD estimate of a first-order-FOGMRP. For that, we generated 6 months of FOGMRP data at a 30 sec sampling rate, with a time constant of 6 hours and a standard deviation of 1.5 m. Because we know the theoretical expression of a FOGMRP PSD, we can compare it to the various PSD estimates. Figure C.2 shows the PSD estimates using the various tapering windows represented in Figure C.1. The red dashed curve represents the theoretical PSD curve of a FOGMRP. The grey curve represents the PSD estimate obtained when using a rectangular window ($T_1 = T_2 = 7$ h). Rectangular windows are known for inducing spectral leakage in the frequency domain. At high frequencies (right part of the plot), the spectral leakage induce a divergence of the PSD estimate from the true PSD curve. We can see that the more T_2 is increased, less spectral leakage is visible (bumpiness of the curves) and the closer the PSD estimates get to the true FOGMRP PSD curve.

These results suggest that PSD estimates with increasing T_2 will converge to the true FOGMRP PSD curve. To test this theory, Figure C.3 shows PSD estimates

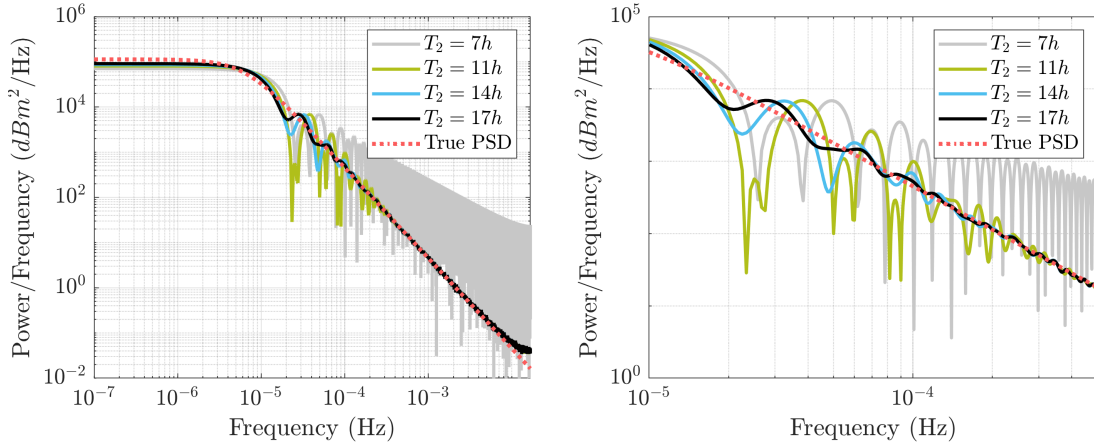


Figure C.2. Impact of tapering window on PSD estimate of FOGMRP in terms of spectral leakage: (a) original figure, (b) zoomed.

using tapering windows whose T_2 values range from 24h to 1 month of data. Beyond a certain length of time for T_2 , the curves can be seen to become noisier at all frequencies. We observe that the ACF from which the PSD is derived also becomes noisier for large values of T_2 .

The results of this section suggest that $T_2 = 48h$ is an ideal value for the PSD estimation of a FOGMRP.

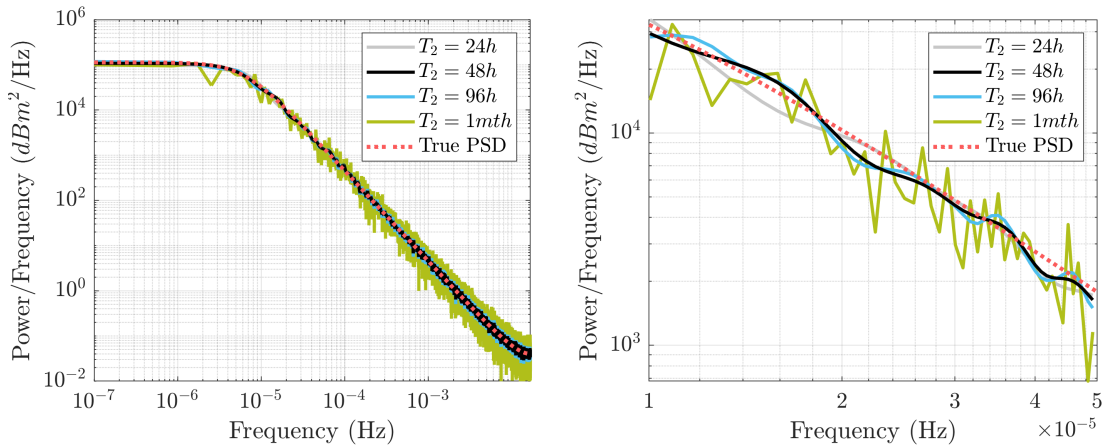


Figure C.3. Impact of tapering window on PSD estimate of FOGMRP in terms of data noise: (a) original figure, and (b) zoomed.

C.2 Impact of the window shape on real orbit and clock error data

In this section, we verify that this theory applies to the orbit and clock errors using an example dataset of PRN 01 for 2018.

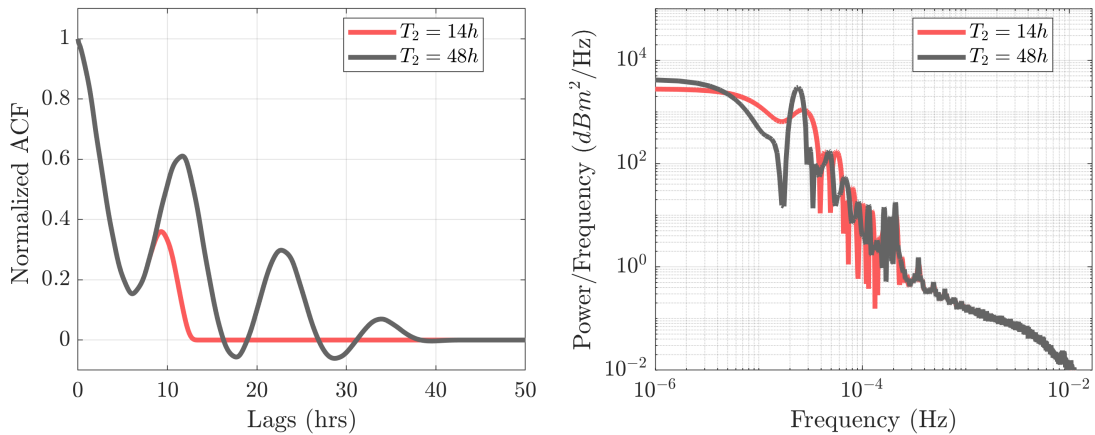


Figure C.4. (a) Tapered ACF and (b) PSD estimates for GPS PRN 01 orbit + clock errors.

The grey curve of Figure C.4 (b) shows the PSD estimate of this data set with $T_1 = 7h$ and $T_2 = 48h$, as suggested by the analysis in Section C.1. If we were to upper bound this curve with a FOGMRP (see Chapter 2), the associated sigma would have to be inflated to upper bound the frequency bump observed at $f = 2.4 \times 10^{-5}$ Hz. That frequency is equivalent, in the time domain to a period of 11.5 hours. Note that GPS satellites have an orbit period of half a sidereal day (23h 56m 4s) and will therefore take about 11.9 hours to orbit the earth. Note also that this orbital period can be observed on the grey ACF curve in Figure C.4 (a). The grey curve represents the tapered ACF of the data set, with $T_1 = 7h$ and $T_2 = 48h$. Therefore, the ACF lobe located at the 11.9 hour time lag is barely tapered and will result, in the PSD domain, in a frequency bump that will drive the PSD bounding process.

Since a satellite pass lasts 7 hours at the maximum, tapering the ACFs after this time lag will not impact the robustness of our model. Smaller T_2 values will result in an attenuated orbital period frequency bump, and therefore a better, less conservative, PSD bounding model.

Therefore, any $14h \leq T_2 \leq 48h$ would ensure limited spectral leakage and noise, but to reduce the impact of the orbital period on our PSD estimate, smaller T_2 values should be prioritized.

To definitely select the ideal value of T_2 an additional layer of optimization will be taken into consideration: optimal FOGMRP bound. This work is done in Appendix H.

APPENDIX D
NUMBER OF INDEPENDENT SAMPLES IN A FOGMRP

Let us define a stationary, ergodic random process $x(t)$ with sample mean $\hat{\mu}_x$ and variance $\hat{\sigma}_x^2$ based on a data set of time duration T . Let us call C_{xx} the autocovariance function of the random process $x(t)$. Assuming the process is zero mean, Chapter 8 of [15] provides a closed form equation of the mean square errors of $\hat{\mu}_x$ and $\hat{\sigma}_x^2$ as:

$$Var[\hat{\mu}_x] = \frac{1}{T} \int_{-T}^T \left(1 - \frac{|\eta|}{T}\right) C_{xx}(\eta) d\eta \quad (D.1)$$

$$Var[\hat{\sigma}_x^2] = \frac{2}{T} \int_{-T}^T \left(1 - \frac{|\eta|}{T}\right) C_{xx}^2(\eta) d\eta \quad (D.2)$$

Let us now assume that $x(t)$ is a zero-mean, FOGMRP with time constant τ_x and standard deviation σ_x . Its autocovariance function is expressed as:

$$C_{xx}(\eta) = \sigma_x^2 e^{-|\eta|/\tau_x} \quad (D.3)$$

Replacing this term in Equation (D.1), and exploiting the symmetry of the autocovariance function, we have:

$$\frac{Var[\hat{\mu}_x]}{\sigma_x^2} = \frac{2}{T} \int_0^T \left(1 - \frac{\eta}{T}\right) e^{-\eta/\tau_x} d\eta \quad (D.4)$$

After direct integration of the first term and integration by parts of the second term, Equation (D.4) simplifies to:

$$\frac{Var[\hat{\mu}_x]}{\sigma_x^2} = \frac{2\tau_x}{T} \left\{ 1 - \frac{\tau_x}{T} (1 - e^{-T/\tau_x}) \right\} \quad (D.5)$$

Similarly, substituting Equation (D.3) into Equation (D.2), and considering the zero mean assumption stated above, we have:

$$\frac{Var[\hat{\sigma}_x^2]}{\sigma_x^4} = \frac{4}{T} \int_0^T \left(1 - \frac{\eta}{T}\right) e^{-2\eta/\tau_x} d\eta \quad (\text{D.6})$$

After direct integration of the first term and integration by parts of the second term, Equation (D.6) simplifies to:

$$\frac{Var[\hat{\sigma}_x^2]}{\sigma_x^4} = \frac{2\tau_x}{T} \left\{ 1 - \frac{\tau_x}{2T} (1 - e^{-2T/\tau_x}) \right\} \quad (\text{D.7})$$

In this work, we are looking at a year's worth of data and time constants shorter than one day, so we can neglect the terms of order $(\tau_x/T)^2$ and higher. Equations (D.5) and (D.7) become:

$$\frac{Var[\hat{\mu}_x]}{\sigma_x^2} \approx \frac{Var[\hat{\sigma}_x^2]}{\sigma_x^4} \approx \frac{2\tau_x}{T} \quad (\text{D.8})$$

Therefore, we conclude that any zero mean FOGMRP with $\tau_x/T \ll 1$ has effectively independent samples every $2\tau_x$.

APPENDIX E
ONE-TO-ONE MAPPING ANALYSIS OF INERTIAL ERRORS

This appendix provides a short overview of each error term in Equation ?? and shows that an upper bound in the AV domain is an upper bound in the PSD domain.

E.1 Velocity random walk modeled as a white noise

Let us define $\bar{\Sigma}_{WN}^2$ (or ΔN_0) as an AV upper bound on the actual white noise's AV, such that:

$$\bar{\Sigma}_{WN}^2(\tau) = \frac{\bar{N}_0}{\tau} = \frac{N_0 + \Delta N_0}{\tau} > \frac{N_0}{\tau} = \Sigma_{WN}^2(\tau) \quad \forall \tau \in \mathbb{R}^+ \quad (\text{E.1})$$

Clearly, this is equivalent to:

$$\bar{N}_0 > N_0$$

White noises can be expressed in the PSD domain as:

$$S_{WN} = \frac{N_0}{2}$$

And it is therefore trivial to prove that the condition in Equation E.1 automatically implies:

$$\bar{S}_{WN} = \frac{\bar{N}_0}{2} > \frac{N_0}{2} = S_{WN} \quad (\text{E.2})$$

The reverse implication is trivial as well.

E.2 Acceleration random walk modeled as a random walk

Similarly, let us define an AV upper bound on the random walk error term K as:

$$\bar{\Sigma}_{RW}^2(\tau) = \frac{\bar{K}^2 \tau}{3} = \frac{K^2 + \Delta K^2}{3} > \frac{K^2 \tau}{3} = \Sigma_{RW}^2(\tau) \quad \forall \tau \in \mathbb{R}^+ \quad (\text{E.3})$$

For this condition to be valid over all $\tau \in \mathbb{R}^+$, we must have:

$$\bar{K}^2 > K^2$$

Which in turns, is equivalent to an upper bound in the PSD domain:

$$\bar{S}_{RW}(f) = \frac{\bar{K}^2}{(2\pi f)^2} > \frac{K^2}{(2\pi f)^2} = S_{RW}(f) \quad \forall f < f_N \quad (\text{E.4})$$

E.3 Flicker noises modeled as a first order GMRP

Let us consider a flicker noise bound $\bar{\Sigma}_F^2$ in the AV domain, on the true flicker noise error AV Σ_F^2 , such that:

$$\bar{\Sigma}_F^2(\tau) = \frac{2\bar{\sigma}_F^2}{\pi} \ln(2) > \frac{2\sigma_F^2}{\pi} \ln(2) = \Sigma_F^2(\tau) \quad \forall \tau \in \mathbb{R}^+ \quad (\text{E.5})$$

Since every terms in that equation are scalar, it is trivial, once again, to show that the bounding is verified in the PSD domain as well:

$$\bar{S}_F(f) = \frac{\bar{\sigma}_F^2}{2\pi f} > \frac{\sigma_F^2}{2\pi f} = S_F(f) \quad \forall f < f_N \quad (\text{E.6})$$

However, it is important to note that flicker noise cannot be modeled in the state space domain. Instead, first order GMRP are often used to model flicker noises. To satisfy the integrity requirements of safety critical applications, this first order GMRP (\bar{S}_G) will have to upper bound the flicker noise:

$$\bar{S}_G(f) > \bar{S}_F(f) > S_F(f) \quad \forall f < f_N \quad (\text{E.7})$$

APPENDIX F
IONOSPHERIC DELAY CUT OFF FREQUENCY VALIDATION

The methodology introduced in this thesis to characterize carrier phase multipath relies on the differencing of carrier phase measurements from two distinct frequencies. The resulting residuals are then filtered out using a high pass filter with cut off frequency f_c . This cut off frequency was carefully selected so as to remove the ionospheric delay from the residuals. However, more work needs to be done to ensure that this choice of f_c will not impact the filtered residuals (i.e. multipath). In other words, does the high pass filtering of the $L_1 - L_2$ residuals also removes some of its multipath?

In this appendix, we validate the choice of f_c and prove that the amount of carrier phase multipath removed during the filtering of the $L_1 - L_2$ residuals is negligible.

F.1 Mathematical representation of multipath

Let us consider the two most common reflection scenarios: ground and side/wall reflections.

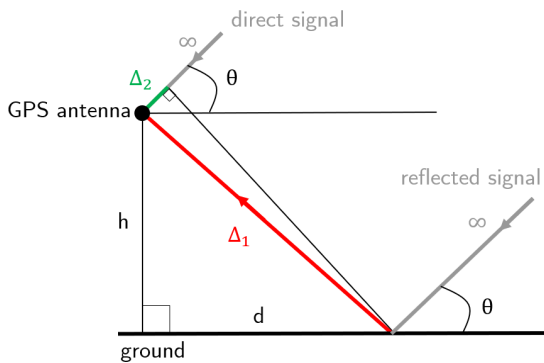


Figure F.1. Ground Reflection

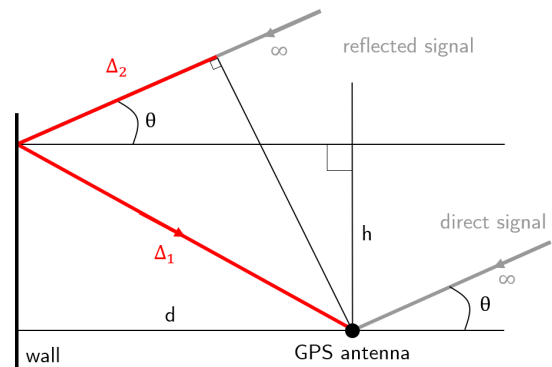


Figure F.2. Wall Reflection

F.1.1 Modeling of ground-induced multipath. Let us assume the following scenario (represented in Figure F.1 from [63]):

- the GNSS antenna is located at an height h from the ground,
- the reflected signal arrives with an incidence angle θ .

The reflected signal travels an extra distance ($\Delta = \Delta_1 - \Delta_2$ in Figure F.1) with respect to the line of sight signal, which results in a phase shift that will directly impact the carrier phase measurement received (and later processed) by the user.

By simple trigonometric manipulation (e.g. $\cos(2\theta) = (1 - 2\sin^2\theta)$), the extra distance travelled by the signal can be expressed as ([63]):

$$\begin{aligned}\Delta &= \Delta_1 - \Delta_2, \\ &= \frac{h}{\sin\theta} (1 - \cos(2\theta)), \\ &= 2h\sin\theta.\end{aligned}\tag{F.1}$$

To express this extra travelled distance in cycles (let us call it ψ), we simply divide Equation F.1 by the wavelength λ of the incoming signal:

$$\psi = z\sin\theta,\tag{F.2}$$

where $z = \frac{2h}{\lambda}$.

F.1.2 Modeling of wall-induced multipath. Let us now consider the case of multipath induced by a wall reflection, as represented in Figure F.2, with the following properties:

- the GNSS antenna is located at a distance d from the reflecting wall,
- the reflected signal arrives with an incidence angle θ .

In this case, the extra travel distance of the reflected signal can be expressed

as:

$$\Delta = \Delta_1 + \Delta_2, \quad (\text{F.3})$$

$$= \frac{d}{\cos\theta} (1 + \cos(2\theta)), \quad (\text{F.4})$$

$$= 2d\cos\theta. \quad (\text{F.5})$$

In this case, the extra travelled distance in cycles is expressed as:

$$\psi = z\cos\theta, \quad (\text{F.6})$$

where $z = \frac{2d}{\lambda}$.

Equations F.2 and F.6 are mathematical expressions of the additional travel distance of a reflected signal, in cycles. In this work, we focus on carrier phase measurements. It is therefore of great interest to express the impact ψ will have on the carrier phase measurement ϕ . Let us denote this added contribution as $\delta\phi$. The in-phase versus quadrature-phase representation of a reflected signal is shown in Figure F.3 from [63].

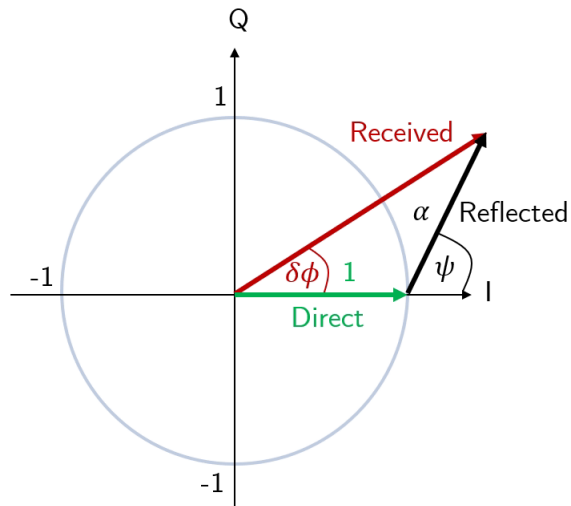


Figure F.3. Complex representation of direct VS reflected signal.

By simple trigonometric manipulation, one can derive the following expression for $\delta\phi$:

$$\tan(\delta\phi) = \frac{\alpha \sin\psi}{1 + \alpha \cos\psi}, \quad (\text{F.7})$$

where α is the relative magnitude of the reflected signal.

Since the reflected signal's magnitude is always smaller than the direct signal's, we are faced with two possible cases:

Case 1:

The reflected signal's amplitude is much smaller than the direct signal's amplitude: $\alpha \ll 1$.

In this case, Equation F.7 can be simplified with:

$$\tan(\delta\phi) \approx \delta\phi \approx \alpha \sin\psi. \quad (\text{F.8})$$

Given the expressions of ψ derived above, this equation can be expanded using the Jacobi-Anger expansion:

$$\begin{cases} \sin(x \cos y) = -2 \sum_{n=1}^{\infty} (-1)^n J_{2n-1}(x) \cos((2n-1)y) \\ \sin(x \sin y) = 2 \sum_{n=1}^{\infty} J_{2n-1}(x) \sin((2n-1)y) \end{cases} \quad (\text{F.9})$$

where J_i is the i^{th} order Bessel function.

Applying this expansion to Equation F.8 for the two reflection scenarios introduced in Sections F.1.1 and F.1.2 yields:

$$\left\{ \begin{array}{l} \text{Ground : } \delta\phi \approx \alpha \sin(z \cos\theta) = 2\alpha \sum_{n=1}^{\infty} J_{2n-1}(z) \sin((2n-1)\theta) \\ \text{Wall : } \delta\phi \approx \alpha \sin(z \sin\theta) = -2\alpha \sum_{n=1}^{\infty} (-1)^n J_{2n-1}(z) \cos((2n-1)\theta) \end{array} \right. \quad (\text{F.10})$$

Case 2:

The reflected signal's amplitude is smaller but not negligible compared to the the direct signal's amplitude: $\alpha < 1$.

Let us apply Taylor series expansion to both sides of Equation F.7:

$$\delta\phi + \mathcal{O}(\delta\phi^2) \approx \alpha \sin\psi (1 - \alpha \cos\psi + \mathcal{O}(\alpha^2)) \quad (\text{F.11})$$

Simplifying and dropping 3rd order terms yields:

$$\delta\phi \approx \alpha \sin\psi - \frac{\alpha^2}{2} \sin(2\psi). \quad (\text{F.12})$$

Applying the Jacobi-Anger expansion in Equation F.9, and simplifying the notations produce:

$$\left\{ \begin{array}{l} \text{Ground : } \delta\phi \approx \alpha \sum_{n=1}^{\infty} (2J_{2n-1}(z) - \alpha J_{2n-1}(2z)) \sin((2n-1)\theta) \\ \text{Wall : } \delta\phi \approx -\alpha \sum_{n=1}^{\infty} (2J_{2n-1}(z) - \alpha J_{2n-1}(2z)) (-1)^n \cos((2n-1)\theta) \end{array} \right. \quad (\text{F.13})$$

Let us call f_g the frequency at which the receiver's environment/geometry changes. By scaling the integer term $2n-1$ of the expansion of $\delta\phi$ by f_g , we can observe the frequency distribution of $\delta\phi$.

We have now derived expressions for $\delta\phi$ for both of the multipath scenarios considered here. These expressions can help us understand the power distribution of

carrier phase multipath, and, by doing so, validate the ionospheric cut-off frequency derived in this work. Let us apply these to two types of multipath datasets.

F.2 Validation of the cut off frequency for rooftop multipath

In Chapter 5, carrier multipath models were derived for the multipath environment on the rooftop of the Rettaliata Engineering Building, where most of our experimental data is collected. More details on the environment are provided in this Chapter.

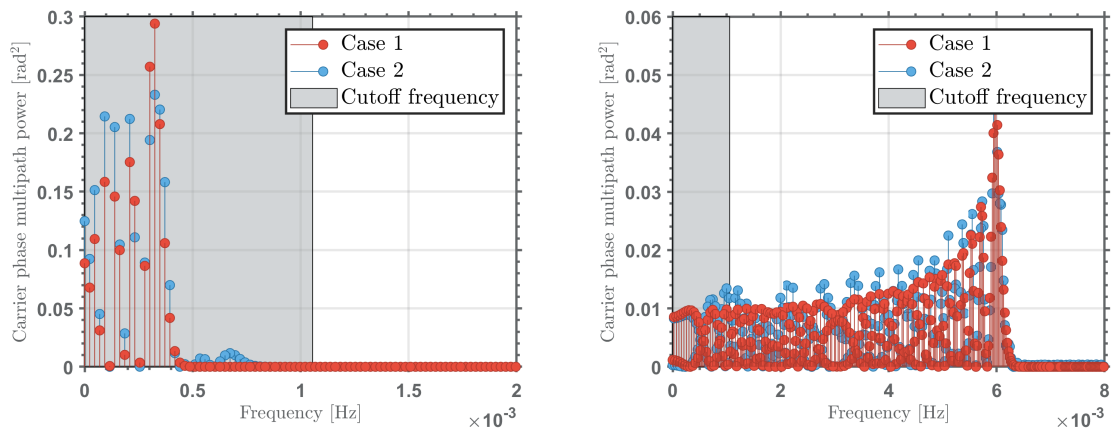


Figure F.4. Bessel approximation of ground (left) and wall (right) reflection power distribution

The data collections performed in this environment are static, therefore, the rate of change of the multipath environment is directly related to the periodicity of the GNSS constellation. The GPS constellation has a periodicity of half a sidereal day (86164.0905 seconds), therefore, $f_g = \frac{2}{86164.0905}$ Hz.

Additionally, the GNSS antenna is located 1 m above the ground (i.e. $h = 1$ m), and the nearest horizontal blockage is 25 m away (i.e. $d = 25$ m).

Figure F.4 represent the power distribution of $\delta\phi$ for both Cases 1 and 2

introduced above, in the ground (left) and wall (right) reflection cases. Note the similarity of results between Cases 1 and 2, suggesting that the second order terms present in Case 2 are negligible. The shaded grey area represents the portion of power that would be removed by filtering with f_c . For the wall reflection case, 11.4% of the multipath's power is filtered out. For the ground reflection case, however, 100% is filtered. Two possible interpretation can be made:

- (i) The Bessel derivation needs refinement (in particular for ground reflections), or,
- (ii) The L1 - L2 ionospheric delay filtering methodology is not appropriate for this multipath environment, since ionospheric delay and ground multipath seem to share their frequency band.

Future work would benefit from investigating this issue further.

F.3 Validation of the cut off frequency for Aircraft Multipath

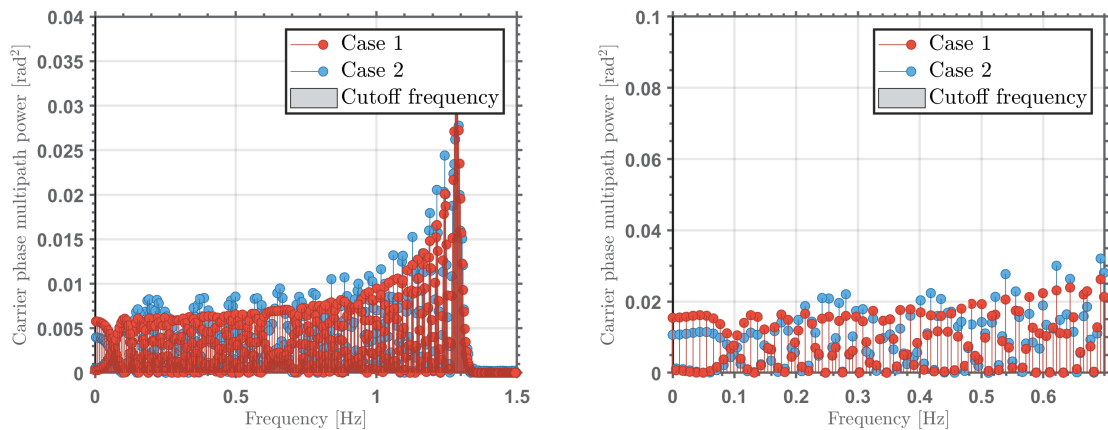


Figure F.5. Bessel approximation of spiral divergence (left) and phugoid (right) modes power distribution

Contrary to static receivers, the carrier multipath geometry observed in-flight aircraft will primarily depend on the flight mode of the aircraft which varies at a

faster rate than the GNSS geometry. Figure F.6, from [63] represents the various flight mode that a receiver could experience. Let us focus here on the phases of flight with the fastest geometry variations: phugoid and spiral divergence modes.

Assuming a Boeing 747-200, Figure F.5 shows the Bessel analysis results for wall reflections with $d = 40$ m (during the spiral divergence phase - left), and ground reflections with $h = 15$ m (during the phugoid phase - right). The shaded grey area representing the portion of power that would be removed by filtering with f_c is barely visible on both plots. For the spiral divergence case, 0% of the multipath's power is filtered out. For the phugoid case, 0.5% is filtered out, suggesting that the filtering of the ionospheric delay will not impact the quality of the remaining multipath residuals.

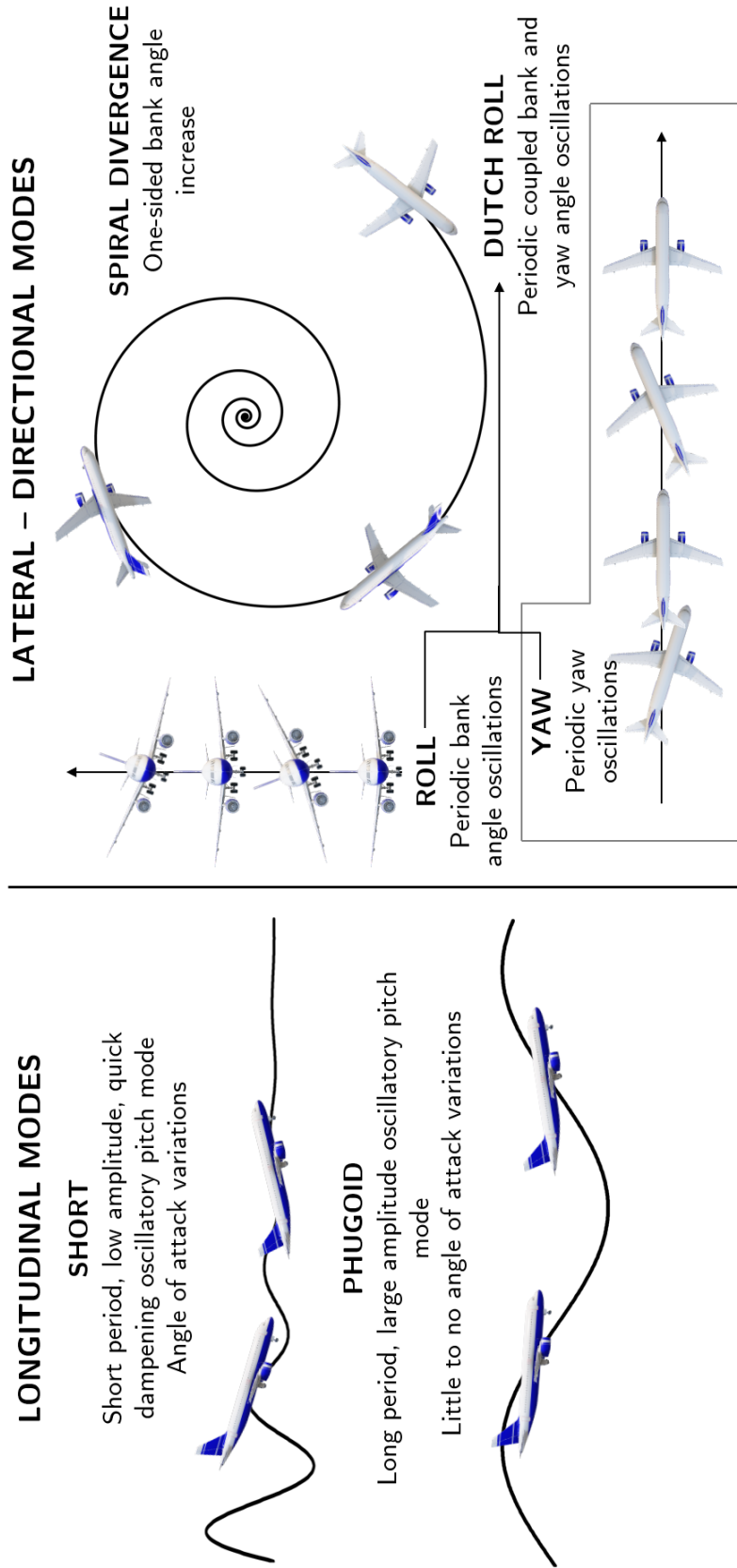


Figure F.6. Aircraft flight modes [63]

APPENDIX G
SNAPSHOT ERROR MODEL OF THE CODE AND CARRIER SMOOTHED
CODE MULTIPATH OF OUR TESTING ENVIRONMENT

In Chapter 7 of this thesis, the error models derived in the previous chapters are put into use in a Kalman Filter version of ARAIM. This KF’s performance is then compared (among other things) to the performance of snapshot ARAIM [41–43]. If most error models used in the KF have been thoroughly derived and described in this thesis, there remain one that still need to be addressed: code multipath. In Chapter 7, we explain that code measurements are used at the first epoch of a satellite in view to help with the initialization of the cycle ambiguities. We therefore need a snapshot model for these errors as well, one that will be specific to the environment in which the experiments are performed (i.e. the rooftop of the Rettaliata Engineering building).

To do so, we collected code and carrier measurements over ten days. Code and Carrier Smoothed Code (CSC) measurements were extracted and processed to produce their respective multipath errors. Note that code measurements are impacted by group delays. These errors are deterministic processes but are environment dependent and difficult to calibrate. They are also difficult to extra and differentiate from multipath errors. The “multipath residuals” modeled here also include group delays. However, residual group delay errors that cannot be modeled will need to be accounted (see Chapter 7).

The datasets are then divided in 5 degree elevation and 10 degree azimuth bins. Standard deviations are computed for each of those bins. They are the results presented below.

The grey points on the left plot of Figure G.1 represents the code multipath standard deviation (y-axis) with respect to satellite elevation (x-axis). An elevation dependent trend can quite clearly be observed, where low elevation satellites produce multipath which is much larger than than the high elevation ones. Similarly, the grey points on the right plot of Figure G.1 represents the CSC multipath standard deviation.

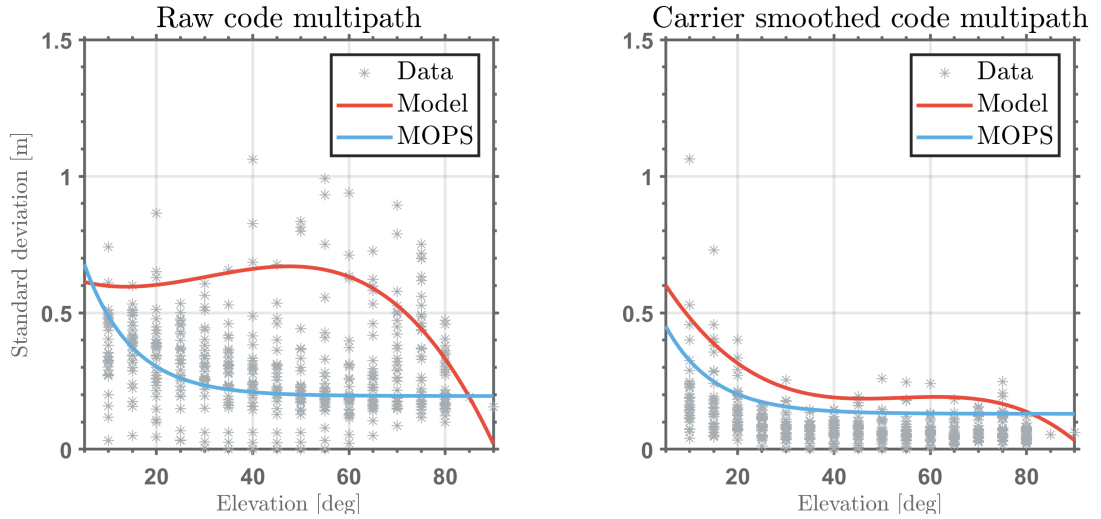


Figure G.1. Rooftop multipath

To have a comparison of the multipath observed on the rooftop and the one usually observed in aircrafts, the blue curve on each of those plots represent the multipath model used in ARAIM (see [1], [7]). We can see that the rooftop experiences much larger multipath values, especially at low elevations.

The model chosen for code ρ and CSC $\tilde{\rho}$ multipath are represented in red. They are obtained with the following elevation-dependent polynomials:

$$\sigma_{\rho/\tilde{\rho}} = P_{\rho/\tilde{\rho}}(1)\theta_i^3 + P_{\rho/\tilde{\rho}}(2)\theta_i^2 + P_{\rho/\tilde{\rho}}(3)\theta_i + P_{\rho/\tilde{\rho}}(4), \quad (\text{G.1})$$

where $P_\rho = [-3.865 \times 10^{-6}, \quad 3.550 \times 10^{-4}, \quad -7.559 \times 10^{-3}, \quad 0.6423]$

and $P_{\tilde{\rho}} = [-3.81 \times 10^{-6}, \quad 6.155 \times 10^{-4}, \quad -0.0325, \quad 0.749]$.

These models will be used in Chapter 7 during the performance evaluation of recursive ARAIM.

APPENDIX H

PSD BOUNDING OPTIMIZATION: CHOOSING THE BEST TAPERING
WINDOW AND FOGMRP BOUND FOR A GIVEN DATASET

In Chapter 2, we introduced a PSD estimation, and bounding methodology which follows the following steps:

- Estimate the ACF of the dataset x : $R_x(\tau)$
- Apply a tapering window $\Gamma(\tau, T_1, T_2)$ to $R_x(\tau)$ to obtain a modified ACF: $\tilde{R}_x(\tau)$
- Take the Fourier transform of the modified ACF, and obtain a modified PSD: $S_x(f)$
- Bound $S_x(f)$ with a FOGMRP (parameters τ_x and σ_x): $\bar{S}_x(f) = \frac{2\sigma_x^2/\tau_x}{1/\tau_x^2 + 4\pi^2 f^2}$

To minimize our final bound $\bar{S}_x(f)$, while ensuring the model is bounding, we want to optimize of parameters T_1 , T_2 , σ_x and τ_x , such that our final bound is as low as possible. The term “optimized” is employed here to refer to the value within a search space for which the space between the sample PSD curve and the PSD bound is minimized. Secondary optimization rule will attempt to minimize the σ parameter of the resulting FOGMRP bound, and finally maximize its time constant τ .

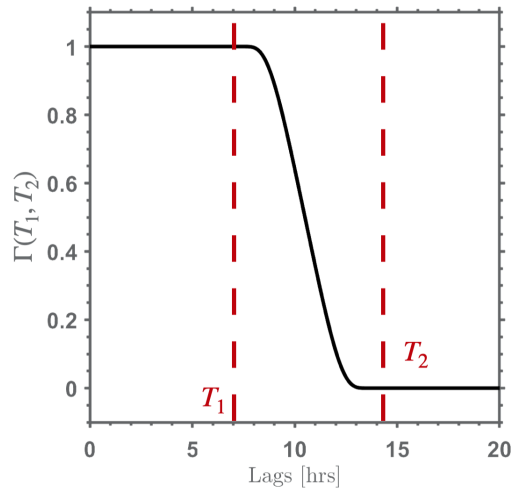


Figure H.1. ACF tapering window representation

Let us divide the problem in two parts. First, the tapering parameters T_1 and T_2 need to be selected so as to minimize spectral leakage and obtain the PSD with the lowest variance possible (and eventually minimize the bound in the next step). Second and last, we find the optimal model $\bar{S}_x(f)$ which tightly upper bounds a sample PSD $S_x(f)$ obtained with the previously derived tapering window. In other words, we want to find σ_x and τ_x that minimize $|\bar{S}_x(f) - S_x(f)|$ while verifying the constraint $\bar{S}_x(f) - S_x(f) > 0 \quad \forall f$.

As detailed in Chapter 2 and represented in Figure H.1, T_1 is the value for which ACF values associated to lag time $\tau \leq T_1$ remain unchanged by the tapering, and T_2 is the value for which ACF values associated to lag time $\tau \geq T_2$ are set to zero. Spectral leakage is introduced in the PSD estimation process when the window is rectangular (i.e. $T_1 = T_2$). To reduce spectral leakage, it is therefore in our best interest to choose T_1 and T_2 as far apart as possible. But choosing a value of T_2 that is too large will also introduce unnecessary noise in the PSD and increase the overall value of the PSD estimate, and hence its final bounding.

Additionally, for each of the errors presented in this dissertation, the value of T_1 will already be known. For orbit and clock errors and multipath, the user will not observe correlation times that are longer than one satellite pass (i.e. 7 hours). For tropospheric delay, the user will be limited to the mission duration (for aviation, the longest flight lasts 18 hours). Therefore, the optimization presented in this Appendix focuses on only three parameters: T_2 , σ_x and τ_x .

In this Appendix, we take an example data set: the orbit and clock errors of GPS PRN 24 over the years 2018-2020. The tapering window results obtained in this Appendix are general and can/will be used for the other errors as well.

Optimization results are shown in Figure H.2. To limit the amount of figures

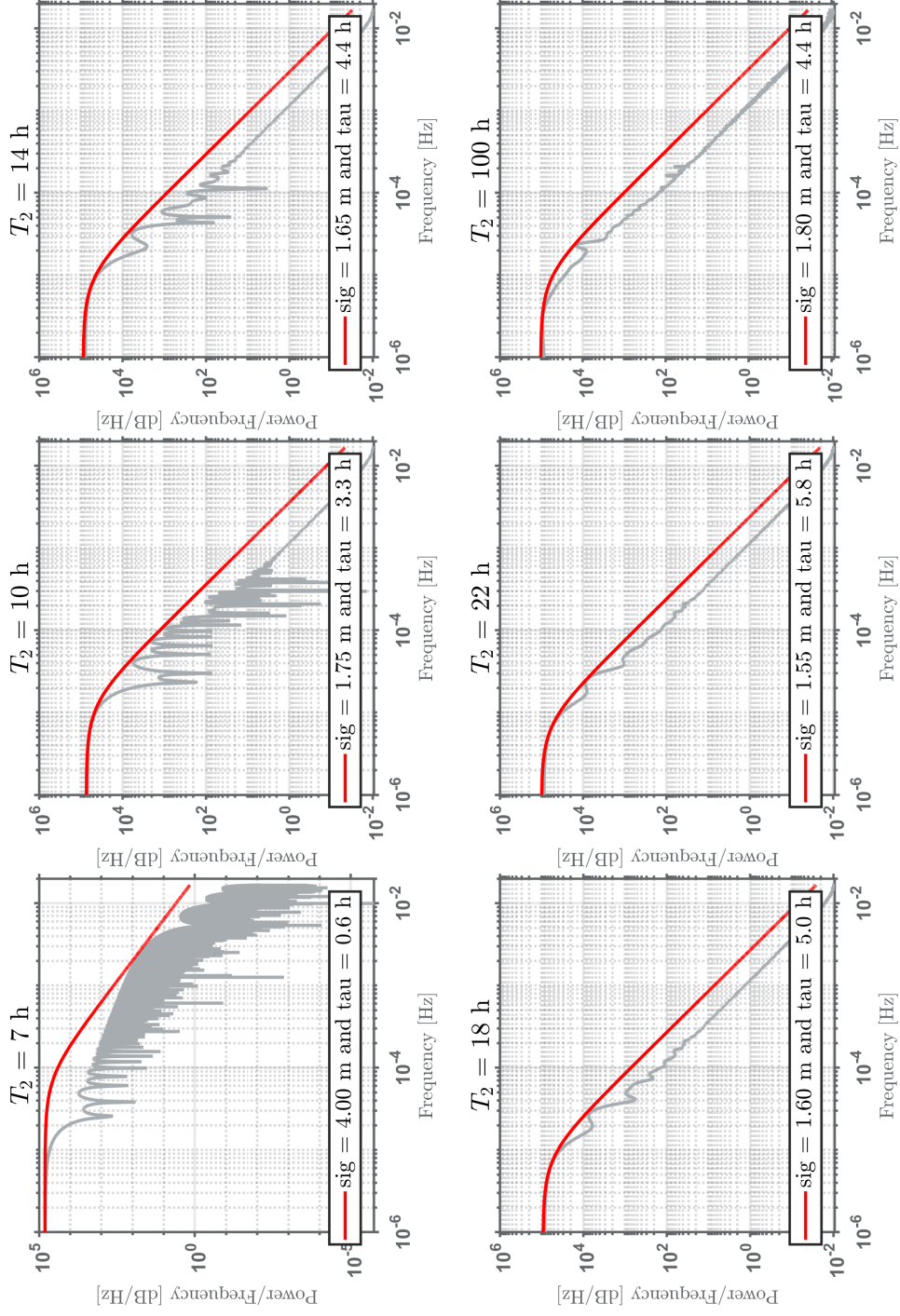


Figure H.2. Selection of the optimal tapering window and FOGMRP parameter, T_2 , σ_x and τ_x for an example dataset (orbit and clock errors of GPS PRN 24 during 2018-2020)

shown here, only 6 values of T_2 (and their associated optimized FOGMRP bound) are represented here. Those values have been chosen to represent the general trend observed while changing T_2 , and include the optimal T_2 , σ_x and τ_x values associated with this dataset. Figure H.2 shows that the lowest σ is 1.55 meters and is obtained for T_2 between 20 – 22 hours. More values of T_2 were tested, but only a few are represented here. To select which value of T_2 is truly optimal, we direct the reader to the results observed in the sensitivity analysis of Chapter 7. In this appendix, the sensitivity of the KF's standard deviation to its error model's parameters is analyzed and revealed that higher FOGMRP time constant values should be prioritised in order to decrease the KF's standard deviation. Note that this last comment is specific to the KF designed in this dissertation and is not necessarily true for all KFs.

Therefore, the optimal tapering and bounding values of the GPS orbit and clock errors of GPS PRN 24 are $T_1 = 7$ hours, $T_2 = 22$ hours, $\sigma_x = 1.55$ meters, and $\tau_x = 5.8$ hours.

APPENDIX I

GPS AND GALILEO SATELLITE INFORMATION DURING 2018-2020

This appendix summarizes the block information of each GPS and Galileo satellite used over the period of date used in the modeling of orbit and clock errors in Chapter 3 (2018-2020). The dates used here will help us understand the overall bounding values obtained in this chapter and how those values could be tightened.

Table I.1. GAL Block information between 2018 and 2020

PRN	Block	Date Start	PRN	Block	Date Start
1	GALILEO-2	2016/5/24	18	GALILEO-2	2014/8/21
2	GALILEO-2	2016/5/24	19	GALILEO-1	2012/10/12
3	GALILEO-2	2016/11/17	20	GALILEO-1	2012/10/12
4	GALILEO-2	2016/11/17	21	GALILEO-2	2017/12/12
5	GALILEO-2	2016/11/17	22	GALILEO-2	2015/3/27
7	GALILEO-2	2016/11/17	24	GALILEO-2	2015/9/11
8	GALILEO-2	2015/12/17	25	GALILEO-2	2017/12/12
9	GALILEO-2	2015/12/17	26	GALILEO-2	2015/3/27
11	GALILEO-1	2011/10/21	27	GALILEO-2	2017/12/12
12	GALILEO-1	2011/10/21	30	GALILEO-2	2015/9/11
13	GALILEO-2	2018/7/25	31	GALILEO-2	2017/12/12
14	GALILEO-2	2014/8/21	33	GALILEO-2	2018/7/25
15	GALILEO-2	2018/7/25	36	GALILEO-2	2018/7/25

Table I.2. GPS Block information between 2018 and 2020

PRN	Block	Start	End	PRN	Block	Start	End
1	IIF	2011/7/16		16	IIR-A	2003/1/29	
2	IIR-B	2004/11/6		17	IIR-M	2005/9/26	
3	IIF	2014/10/29		18	IIR-A	2001/1/30	2018/1/23
4	IIR-M	2017/12/1	2018/9/28		IIA	2018/1/24	2020/3/9
	IIA	2018/10/10	2019/1/2		IIIA	2020/3/13	
	IIIA	2019/1/9	2019/7/12	19	IIR-B	2004/3/20	
	IIA	2019/7/13	2019/10/8	20	IIR-A	2000/5/11	
	IIIA	2019/10/20		21	IIR-A	2003/3/31	
5	IIR-M	2009/8/17		22	IIR-B	2003/12/21	
6	IIF	2014/5/17		23	IIR-B	2004/6/23	2020/6/9
7	IIR-M	2008/3/15			IIIA	2020/7/14	
8	IIF	2015/7/15		24	IIF	2012/10/4	
9	IIF	2014/8/2		25	IIF	2010/5/28	
10	IIF	2015/10/31		26	IIF	2015/3/25	
11	IIR-A	1999/10/7	2021/4/9	27	IIF	2013/5/15	
12	IIR-M	2006/11/17		28	IIR-A	2000/7/16	
13	IIR-A	1997/7/23		29	IIR-M	2007/12/20	
14	IIR-A	2000/11/10	2020/7/27	30	IIF	2014/2/21	
	IIIA	2020/11/5		31	IIR-M	2006/9/25	
15	IIR-M	2007/10/17		32	IIF	2016/2/5	

BIBLIOGRAPHY

- [1] Radio Technical Committee for Aeronautics, “Minimum Operational Performance Standard for Global Positioning System/Wide Area Augmentation System airborne equipment system,” tech. rep., RTCA DO-229E, 2016.
- [2] J. Sanz Subirana, J. Juan Zornoza, and M. Hernández-Pajares, *GNSS Data Processing, Volume I: Fundamentals and Algorithms*. Netherlands: ESA Communications, ESA TM-23/1, 2013.
- [3] E. D. Kaplan and C. Hegarty, *Understanding GPS/GNSS: Principles and Applications*. Artech House, 3rd edition, 2017.
- [4] International Civil Aviation Organization, “International Standards and Recommended Practices (SARPS), Annex 10,” tech. rep., Aeronautical Telecommunications, ICAO Std, N/A, 2006.
- [5] S. D. Perea, *Design of an Integrity Support Message for Offline Advanced RAIM*. PhD thesis, RWTH Aachen University, 2019.
- [6] M. Joerger and B. Pervan, “Fault detection and exclusion using solution separation and chi-squared araim,” *IEEE Transactions on Aerospace and Electronic Systems*, vol. 52, no. 2, pp. 726–742, 2016.
- [7] M. Joerger and B. Pervan, “Multi-constellation ARAIM exploiting satellite motion,” *NAVIGATION: Journal of the Institute of Navigation*, vol. 67, no. 2, pp. 235–253, 2020.
- [8] B. DeCleene, “Defining pseudorange integrity overbounding,” in *Proceedings of ION GPS 2000*, 2000.
- [9] J. Rife, S. Pullen, P. Enge, and B. Pervan, “Paired overbounding for nonideal LAAS and WAAS error distributions,” *IEEE TAES*, vol. 42, no. 4, pp. 1386–1395, 2006.
- [10] S. Langel, *Bounding estimation integrity risk for linear systems with structure stochastic modeling uncertainty*. PhD thesis, Illinois Institute of Technology, 2014.
- [11] S. Langel, O. Garcia-Crespillo, and M. Joerger, “A new approach for modeling correlation Gaussian errors using frequency domain overbounding,” in *Proceedings of the IEEE/ION PLANS 2020*, 2020.
- [12] C. Tanil, S. Khanafseh, M. Joerger, and B. Pervan, “An INS monitor to detect GNSS spoofers capable of tracking vehicle position,” *IEEE Transactions on Aerospace and Electronics*, vol. 64, no. 1, pp. 131–143, 2018.
- [13] J. Rife and D. Gebre-Egziabher, “Symmetric overbounding of correlated errors,” *NAVIGATION: Journal of the Institute of Navigation*, vol. 54, no. 2, pp. 109–124, 2007.
- [14] W. Pulford, “A proof of the spherically symmetric overbounding theorem for linear systems,” *NAVIGATION: Journal of the Institute of Navigation*, vol. 55, no. 4, pp. 283–292, 2009.

- [15] J. Bendat and A. Piersol, *Random data analysis and measurement procedures*. New Jersey: John Wiley & Sons, 2010.
- [16] E. Gallon, M. Joerger, and B. Pervan, "Robust modeling of gnss tropospheric delay dynamics," *IEEE Transactions on Aerospace and Electronic Systems*, vol. 57, no. 5, pp. 2992–3003, 2021.
- [17] C. Chatfield, *The Analysis of Time Series: An Introduction, Sixth Edition*. Chapman & Hall/CRC Texts in Statistical Science, Taylor & Francis, 2003.
- [18] S. Langel, O. Garcia-Crespillo, and M. Joerger, "Bounding sequential estimation errors due to Gauss-Markov noise with uncertain time constants," in *Proceedings of the 32nd International Technical Meeting of The Satellite Division of the Institute of Navigation (ION GNSS+ 2019)*, 2019.
- [19] "IEEE standard specification format guide and test procedure for single-axis interferometric fiber optic gyros," *IEEE Std*, pp. 1–84, 1999.
- [20] C. Greenhall, "Spectral ambiguity of allan variance," *IEEE Transactions on Instrumentation and Measurement*, pp. 623–627, 1998.
- [21] H. Levene, "Robust tests for equality of variances," *Contributions to Probability and Statistics: Essays in Honor of Harold Hotelling*. Stanford University Press, pp. 278–292, 1960.
- [22] F. Massey, "The Kolmogorov-Smirnov test for goodness of fit," *Journal of the American Statistical Association*, vol. 46, no. 253, pp. 68–78, 1951.
- [23] E. Gallon, M. Joerger, and B. Pervan, "Robust modeling of gnss orbit and clock error dynamics," *NAVIGATION: Journal of the Institute of Navigation*, vol. 69, no. 4, 2022.
- [24] I. G. Service, "International GNSS Service Data Repository," 2020. Available online at <ftp://cddis.gsfc.nasa.gov/gps/data/>, last accessed: 2020-09-30.
- [25] P. Steigenberger and O. Montenbruck, "Consistency of mgex orbit and clock products," *Engineering*, vol. 6, no. 8, pp. 898–903, 2020.
- [26] M. Schenewerk, "A brief review of basic GPS orbit interpolation strategies," *GPS Solutions*, vol. 6, no. 4, pp. 265–267, 2003.
- [27] RE Anthony Flores, "NAVSTAR GPS Control Segment to User Support Community Interfaces (ICD-GPS-240)," tech. rep., GPS Enterprise, Space and Missile Systems Center - LAAFB, CA, 2022.
- [28] RE Anthony Flores, "NAVSTAR GPS Space Segment/Navigation User Segment Interfaces (IS-GPS-200L)," tech. rep., GPS Enterprise, Space and Missile Systems Center - LAAFB, CA, 2020.
- [29] S. University, "Stanford University GPS Ephemeris Repository," 2020. Available online at <https://gps.stanford.edu/suglephemeris-files>, last accessed: 2020-09-30.
- [30] CNES, "Broadcast Ephemeris Repository," 2019. Available online at <ftp://serenad-pub-lic.cnes.fr/SERENADO/FROMNTMFV2/NAV/>, last accessed: 2020-09-30.

- [31] O. Montenbruck, P. Steigenberger, L. Prange, Z. Deng, Q. Zhao, F. Perosanz, I. Romero, C. Noll, A. Stuerze, G. Weber, R. Schmid, K. MacLeod, and S. Schaer, “The Multi-GNSS Experiment (MGEX) of the International GNSS Service (IGS), Achievements, prospects and challenges,” *Advances in Space Research*, 2017.
- [32] P. Steigenberger, U. Hugentobler, S. Loyer, F. Perosanz, L. Prange, R. Dach, M. Uhlemann, G. Gendt, and O. Montenbruck, “Galileo Orbit and Clock Quality of the IGS Multi-GNSS Experiment,” *Advances in Space Research*, vol. 55, pp. 269–281, 2015.
- [33] European Commission, “Signal-In-Space Intergace Control Document, Issue 2.0,” tech. rep., European GNSS (Galileo) Open Service, 2021.
- [34] ANTEX, “International GNSS Service Antex files,” 2020. Available online at ftp://ftp.igs.org/pub/station/general/pcv_archive/, last accessed: 2020-09-30.
- [35] NGA, “Antenna offset solutions,” 2020. Available online at <https://earth-info.nga.mil/index.php?dir=gnss&action=gnss>, last accessed: 2020-09-30.
- [36] European GNSS Service Center, “Galileo satellite metadata,” 2020. Available online at <https://www.gsc-europa.eu/support-to-developers/galileo-satellite-metadata>, last accessed: 2020-09-30.
- [37] O. Montenbruck, P. Steigenberger, and A. Hauschild, “Broadcast versus precise ephemerides: a multi-gnss perspective,” *GPS Solutions*, vol. 19, pp. 321–333, 2014.
- [38] P. Teunissen and O. Montenbruck, *Springler handbook of Global Navigation Satellite Systems*. AG: Springer International Publishing AG, 2017.
- [39] S. D. Perea, M. Meurer, and B. Pervan, “Impact of sample correlation on SISRE overbound for ARAIM,” *NAVIGATION: Journal of the Institute of Navigation*, vol. 67, no. 1, pp. 1 – 16, 2020.
- [40] A. E. Bryson, *Applied Linear Optimal Control, Examples and Algorithms*. Cambridge University Press, 1st edition ed., 2002.
- [41] Working Group C, “ARAIM Technical Subgroup. Interim Report Issue 1.0.,” tech. rep., EU-US Cooperation on Satellite Navigation, N/A, 2012.
- [42] Working Group C, “ARAIM Technical Subgroup. Milestone 2.0 Report,” tech. rep., EU-US Cooperation on Satellite Navigation, N/A, 2014.
- [43] Working Group C, “ARAIM Technical Subgroup. Milestone 3.0 Report,” tech. rep., EU-US Cooperation on Satellite Navigation, N/A, 2016.
- [44] J. Huang, F. Van Graas, and C. Cohenour, “Characterization of tropospheric spatial decorrelation errors over a 5-km baseline,” *NAVIGATION: Journal of the Institute of Navigation*, vol. 55, no. 1, pp. 39–53, 2008.
- [45] H. E. Ibrahim and A. El-Rabbany, “A regional stochastic model for noaa-based residual tropospheric delay,” in *Proceedings of ION NTM*, (San Diego, CA), 2008.

- [46] G. Boehm, M. Moller, M. Schindelegger, G. Pain, and R. Weber, “Development of an improved empirical model for slant delays in the troposphere (gpt2w),” *GPS Solutions*, vol. 19, no. 1, pp. 433–441, 2014.
- [47] N. CDDIS, “Troposphere solution directory,” 2020. Available online at <ftp://cddis.nasa.gov/gnss/products/troposphere/zpd/>, last accessed: 2020-09-30.
- [48] J. Saastomoinen, “Contributions to the theory of atmospheric refraction,” *Bulletin Geodesique*, pp. 13–34, 1973.
- [49] E. Gallon, M. Joerger, and B. Pervan, “Robust modeling of tropospheric delay dynamics for sequential positioning,” in *Proceedings of the IEEE/ION PLANS 2020*, 2020.
- [50] R. F. Leandro, M. C. Santos, and R. B. Langley, “A north america wide area neutral atmosphere model for gnss applications,” *NAVIGATION: Journal of The Institute of Navigation*, vol. 56, pp. 57–71, 2009.
- [51] E. Gallon, M. Joerger, S. Perea, and B. Pervan, “Error model development for ARAIM exploiting satellite motion,” in *Proceedings of the 32nd International Technical Meeting of The Satellite Division of the Institute of Navigation (ION GNSS+ 2019)*, 2019.
- [52] M. Circiu, S. Caizzone, C. Enneking, F. Fohlmeister, M. Rippl, M. Meurer, M. Felux, I. Gulie, J. Rüegg, D. and Griggs, R. Lazzarini, F. Hagemann, F. Tranchet, P. Bouniol, and M. Sgammini, “Final results on airborne multipath models for dualconstellation dual-frequency aviation applications,” *Proceedings of the 2021 International Technical Meeting of The Institute of Navigation*, pp. 714–727, 2021.
- [53] M. Harris, P. Schlais, T. Murphy, A. Joseph, and J. Kazmierczak, “Gps and galileo airframe multipath error bounding method and test results,” *Proceedings of the 33rd International Technical Meeting of the Satellite Division of The Institute of Navigation (ION GNSS+ 2020)*, pp. 114–139, 2020.
- [54] W. H. Press and G. B. Rybicki, “Fast algorithm for spectral analysis of unevenly sampled data,” *The Astrophysical Journal*, vol. 338, pp. 277–280, 1989.
- [55] D. Titterton and J. Weston, *Strapdown Inertial Navigation Technology*. London, England: Peter Peregrinus Ltd, 1997.
- [56] D. Gebre-Egziabher, *Design and performance analysis of a low-cost aided-dead reckoning navigator*. PhD thesis, Stanford University, 2004.
- [57] N. El-Sheimy, H. Hou, and X. Nui, “Analysis and modeling of inertial sensors using allan variance,” *IEEE Transactions on Instrumentation and Measurement*, pp. 140–149, 2008.
- [58] H. Hou, *Modeling Inertial Sensors Errors using Allan Variance (Master’s thesis)*. PhD thesis, University of Calgary, 2004.
- [59] A. Quinchia, G. Falco, F. E., F. Dosis, and C. Ferrer, “A comparison between different error modeling of mems applied to gps/ins integrated systems,” *Sensors*, vol. 13, pp. 9549–9588, 2013.

- [60] Sensoror, “Stim-300 imu product specifications,” 2021. Available online at <https://www.sensoror.com/products/inertial-measurement-units/stim300/>, last accessed: 2021-04-30.
- [61] E. Gallon, M. Joerger, and B. Pervan, “Frequency-domain modeling of orbit and clock errors for sequential positioning,” in *Proceedings of Institute of Navigation GNSS+ Virtual Conference*, 2020.
- [62] Galileo OS-SDD, “Open Service Service Definition Document v1.2.,” tech. rep., European GNSS Service Center, 2021.
- [63] C. Benz, “Carrier phase multipath characterization and frequency-domain bounding,” Master’s thesis, Illinois Institute of Technology, 2022.